An Improved Electrical Impedance Tomography (EIT) Algorithm for the Detection and Diagnosis of Early Stages of Breast Cancer

by

Rajen Manicon Murugan

A THESIS
SUBMITTED TO THE FACULTY OF GRADUATE STUDIES
IN PARTIAL FULFILLMENT OF THE REQUIREMENTS
FOR THE DEGREE OF

DOCTOR OF PHILOSOPHY

Department of Electrical and Computer Engineering
University of Manitoba
Winnipeg, Manitoba
October 1999

THE UNIVERSITY OF MANITOBA

FACULTY OF GRADUATE STUDIES

*****

COPYRIGHT PERMISSION PAGE

An Improved Electrical Impedance Tomography (EIT) Algorithm for the Detection and Diagnosis of Early Stages of Breast Cancer

BY

Rajen Manicon Murugan

A Thesis/Practicum submitted to the Faculty of Graduate Studies of The University of Manitoba in partial fulfillment of the requirements of the degree

of

Doctor of Philosophy

A Testimony of the Spiritual Presence of My Parents

Dedicated to Mom and Dad,
Though Gone but not Forgotten...

ஹநனஉயவநன வடி ஆடிஅ யனே னுயனஇ
கூடிரபா முடிநே ரெவ டிவ குடிசபடிவவநபே

Abstract

According to Canadian Cancer Statistics, breast cancer continues to be the most frequent type of cancer diagnosed among Canadian women. An estimated 18,700 new cases of breast cancer will be diagnosed in 1999. During their lifetime, 1 woman in 9 is expected to develop breast cancer and 1 woman in 25 is expected to die from it. Early detection is a woman's hope for effective treatment and better survival rates. Unfortunately, present imaging modalities are either ineffective or financially unjustifiable for mass screening. A new non-invasive screening and diagnostic technique (viz., Electrical Impedance Tomography, EIT) with high potential has recently been given much attention. However, the transition of EIT from the laboratory to the clinic is yet to occur. The main problem appears to be one of spatial resolution, usually attributed to the lack of a robust and fast algorithm capable of producing 3-D clinically useful images.

An existing EIT image reconstruction algorithm, the Wexler 3-D EIT algorithm, is further refined to address the problem. A new and efficient scheme, the Modeller-Predictor-Corrector (MPC) method, is devised and implemented on the original Wexler 3-D EIT algorithm to improve its convergence rate. Images are recovered within a time period comparable to that of existing clinical imaging modalities. The spatial resolution of the MPC-recovered image, though recovered in a reasonable time period, is far from what is desired. To this end, a novel approach, the Locator-Compensator (LC) algorithm is developed and implemented to improve EIT's resolution limit, in particular at normal-to-diseased tissue interfaces. Both schemes (viz. LC and MPC) were implemented on 3-D computer simulations of small breast tumour (i.e., benign and malignant) imaging. Using the improved Wexler 3-D EIT algorithm, breast tumours of size 2.35 mm in diameter were detected and diagnosed. Implementation of this improved imaging algorithm in conjunction with the appropriate EIT hardware system is anticipated to provide a safe, cost-effective, and easily accessible screening and diagnostic tool for the detection of small breast tumours. EIT could serve as a complementary tool to conventional X-ray mammography, considering its advantages.

Acknowledgements

My doctoral research could only have been possible with the assistance of many people. First and foremost, I would like to express my sincere gratitude and gratefulness to my advisors Dr. Al Wexler and Dr. Richard Gordon for the advice, encouragement, and support they provided during the course of my studies. Dr. Wexler your motto of "Ready, Fire and Aim" has proved to be beneficial to the completion of this work. Dr. Gordon, thanks for introducing me to Dr. Wexler and many thanks for the stimulating conversations and ideas we have exchanged during these four years.

Special thanks go to Dr. Zhen Mu, for her commentary, assistance, and for her willingness to help despite her busy schedule. I thank all my committee members for providing the guidance and direction that allowed me to complete this work. Your support has been nothing but exemplary.

My family, my wife, and my friends, I thank you all for the love and advice you have provided throughout this project. Without your encouragement and support I would have been unable to successfully complete this endeavor. Least but not last, I would sincerely like to thank everyone at Quantic EMC Inc who had shared my concerns, worries, and joy over the period of this doctoral thesis. Special thanks go to Mr. Greg McNeill for all his help with the graphic software. Thank you all.

Table of Contents

List of Figures

List of Tables

List of Abbreviations

2-D	Two-dimensional
3-D	Three-dimensional
A.C. and D.C.	Alternating Current and Direct Current
AJC	American Joint Committee
APT	Applied Potential Tomography
CT	Computerized Tomography
dB	Decibel
DIS	Intraductal in situ
EICT	Electrical Impedance Computed Tomography
EIT	Electrical Impedance Tomograhy
EM	Electromagnetic
FEM	Finite Element Method
FWHM	Full-Width at Half-Maximum
KHz, MHz, and GHz	Kilohertz, Megahertz, and Gigahertz
LC	Locator-Compensator
LIS	Lobular in situ
LM	Levenberg-Marquardt
MPC	Modeller-Predictor-Corrector
MRI	Magnetic Resonance Imaging
MTF	Modulation Transfer Function
NM	Nuclear Medicine
PET	Positron Emission Tomography
PSF	Point Spread Function
TDLU	Terminal Duct Lobular Unit
TNM	Tumour-Node-Metastases
US	Ultrasound
WHO	World Health Organization

Chapter 1

Introduction

1.1 Electrical Impedance Tomography (EIT) as an Imaging Modality

The objective of electrical impedance tomography (EIT[1]) is to reconstruct images of the distribution of electrical impedance within a conducting region by means of impedance measurements made on the surface of the region [Hend78, Pric79, Brow82, and Vale89]. In medical applications, small subliminal electrical currents (0.1- 1 mA at 0 - 100 kHz) are applied to the body from an array of electrodes attached to the skin. These currents are below the threshold for perception, let alone tissue damage. Subsequently, from measurements of voltages and/or currents made at these electrodes, image reconstruction algorithms are applied to produce the impedance images of the underlying body structure (i.e., this is characteristic of an inverse problem) [John95]. Due to the differential electrical (i.e., impedance, Z at macroscopic scale) or 'dielectric' (i.e., conductivity, σ or relative permittivity, ε' at microscopic scale) properties of biological tissues at the above frequencies (see Table 1.0) [Gabr96], the resulting impedance images display useful and previously unobtainable anatomical information. A clear and comprehensive relationship between the macroscopic and microscopic electrical behaviour of tissues can be found in Foster and Schwan, 1989 [Fost89] and Rigaud *et al.*, 1996[Riga96a].

[1] EIT is also known as Applied Potential Tomography (APT) or Electrical Impedance Computed Tomography (EICT).

As a potential imaging modality, EIT offers several advantages over existing medical imaging techniques such as X-ray Mammography (film-screen or digital), Computed Tomography (CT), and Magnetic Resonance Imaging (MRI). The positive attributes of EIT are its ability to produce images at reduced biological hazard, its relatively inexpensive instrumentation requirements, and its physical ease of operation [Webs90]. The technique has potential in medical [Kotr97], industrial [Yang97], and environmental [Tamb87] applications. For medical applications, EIT is being considered as a screening [Gord99] or a diagnostic tool.

Table 1.0: Dielectric Properties of Biological Tissues at Frequencies of 10 kHz and 100 kHz.

Tissue	Frequency	Conductivity, σ (S/m)	Relative Permittivity, ε'
Liver	10 kHz	0.15	5.5×10^4
Spleen	100 kHz	0.62	3260
Lung	10 kHz	0.11	2.5×10^4
Kidney	100 kHz	0.25	$1.09 - 1.25 \times 10^4$
Bone	10 kHz	0.013	640
Whole Blood	100 kHz	0.55	4000
Skeletal Muscle	10 kHz	0.55	8.0×10^4

*** Reprinted, with permission, from reference [Gabr96].**

However, as with any tomographic technique, the spatial resolution of EIT is limited by the number of possible independent measurements performed on the object under investigation, and as well as by the signal-to-noise ratio of the collected data [Guar91]. Consequently, the focus in medicine has been on developing applications where resolution is of no major concern. Despite the severe limitation of spatial resolution, ongoing hardware and software developments are broadening EIT's potential to applications where resolution is of the utmost importance. One

such application, of worldwide interest, is in the detection of early stages of breast cancer. The ultimate goal of researchers in this area is to develop a clinical EIT-based breast cancer-screening tool to either complement or replace mammography.

1.2 Medical, Industrial and Environmental Applications of EIT

Many possible clinical applications of electrical impedance tomography have been investigated. Examples include gastric emptying, pulmonary ventilation, perfusion changes during the cardiac cycle, pelvic venous congestion, hyperthermia monitoring, breast cancer screening, and swallowing disorders [Dijk93, Jong94, and Boon97]. Dynamic imaging of impedance changes with time offers the most immediate clinical potential. A potential application of 'static' EIT imaging would be in the screening of breast tumours. Both 'dynamic' and 'static' imaging will be discussed later.

EIT has been used successfully in geophysical applications [Telf76 and Send82]. Tamburi *et al.*, 1987, convincingly demonstrated the effectiveness of an EIT-based system, Electroscan[2], in subsurface imaging of pollution plumes [Tamb87]. Industrial applications of EIT-based techniques include multiphase flow measurement, dynamic internal behaviour of process vessels, reactors, separators or pipelines, fluidized bed analysis, and combustion flame monitoring [Plas95, Yang95, Xie92, and Wang94].

1.3 A Review of Clinical EIT Literature

A comprehensive review on the fundamentals, principles, and concepts of electrical impedance tomography reconstruction algorithms can be found in the literature [Moru96]. Rigaud and Morucci, 1996, published an excellent review on existing hardware solutions for acquisition systems for EIT [Riga96b]. More recently, Boone *et al.*, 1997 [Boon97] published a summary of present and future development in EIT (viz., hardware and reconstruction algorithm). The clinical applications of EIT were reviewed by Webster *et al.*, 1988 [Webs88], Dijkstra *et al.*, 1993 [Dijk93],

[2] Electroscan -- An EIT imaging system developed by Quantic Electroscan Inc., Winnipeg, MB, Canada

Jongschaap *et al.*, 1994 [Jong94], Kotre 1997 [Kotr97], and Boone *et al.*, 1997 [Boon97].

There are presently three ways to use electrical impedance tomography (EIT) in the clinical environment [Boon97]:

- imaging the distribution of absolute impedance within the body at a specific frequency (i.e., 'static' imaging);
- imaging the frequency variation of impedance within the body (i.e., 'multifrequency' imaging); and
- imaging the variation in impedance during breathing or some other physiological change in time, at a single-frequency (i.e., 'dynamic' imaging).

The first two ways are normally concerned with producing images that show how the different types of tissues are distributed in the body; this is sometimes known as *tissue characterization* or *anatomical imaging*. In such applications, EIT is being used as an alternative to X-rays, CT and MRI, with certain practical advantages. The third technique produces images of physiological *function*, such as in the imaging of short (e.g., millisecond) changes in the physiological state of tissue.

In electrical impedance tomography, images are reconstructed from sets of electrical measurements made on the surface of the body. To obtain high-quality images, measurements with good accuracy, precision, and repeatability are needed from the data acquisition system. Boone *et al.*, 1997, provided an informative review of the components of a typical EIT data acquisition system [Boon97]. Noise, optimal current patterns, and electrode-electrolyte impedance among other factors impose stringent requirements on the accuracy of an EIT data acquisition system. Despite these hurdles, useful images, albeit at relatively low resolution, have been obtained. Metherall *et al.*, 1996, using a 64-electrode data acquisition system, reported a spatial resolution of about 10% of image diameter for a centrally located object in the cross-sectional plane [Meth96]. Using a 32-electrode system, Cook *et al.*, 1994, obtained a

spatial resolution of 14% for a similar scenario [Cook94]. Although, the spatial resolution of EIT is limited, its temporal resolution and sensitivity in 'dynamic' imaging is quite good [Kotr97]. It appears that better spatial resolution ought to be achievable by improving either the data acquisition system and/or the performance of the reconstruction algorithm [Guar91]. This thesis will focus on improving the latter, with the objective to image breast tumours at a physical size corresponding to relatively good prognoses.

1.4 A Review of EIT Systems Hardware

Although the focus of this work is on EIT image reconstruction, most of the factors limiting measurement accuracy in EIT systems are at its front end, i.e., the data acquisition system. In most practical systems, the measuring device applies a known, constant current to two or more electrodes, and measures voltages that develop between other electrodes. As published by Boone *et al.*, 1997, a practical EIT system will normally have the following components: waveform synthesizer, current source, differential amplifier, and a demodulator or some combination of these components [Boon97]. For a comprehensive discussion on EIT hardware components, see the following references [Riga96b and Boon97].

Rigaud and Morucci, 1996, published an excellent review on the hardware solutions developed for EIT and outlined changes that have taken place in the previous decade, in terms of measurement strategy and development to overcome hardware error sources that have undesirable effects on image recovery [Riga96b]. In practice, it appears that there are formidable instrumentation problems, due to the interaction of finite current drive output impedance, recording amplifier common mode rejection, and unequal skin-electrode impedances. A number of different EIT systems have been successfully constructed or are presently under development to address these limitations [Smit90, Riu92, Cook94, and Brow94]. These employ differing strategies, such as additional electrodes, multiple electrode current injection, or recording at multiple frequencies, to improve image accuracy with great success.

1.5 A Review of EIT Image Reconstruction Algorithms

Image reconstruction in EIT is the process of converting the voltage/current measurements from the data acquisition equipment into images. The reconstruction process makes use of the relationship known to exist between voltage, current, and resistance (viz., Poisson's equation). EIT image reconstruction is a *nonlinear* inverse problem since the voltage is a function of both the applied current and resistivity, and as well as the geometry of the imaging region. The inverse problem of reconstructing the electrical impedance parameters from voltage and current measurements made on the boundary is very difficult. This is due to the fact that this inverse problem is both *nonlinear*, and quite arguably, depending on the algorithmic method employed for impedance image recovery, *ill-posed* [Oost91]. *Ill-posedness* means that the solution does not depend continuously on the measured data and that small changes in the measured data can lead to relatively large errors in the reconstruction of the impedance distribution.

Many approaches have been proposed for solving the inverse nonlinear problem that arises in EIT. These methods fall into two broad categories. The first are non-iterative (single-step) techniques, based on linear approximations. The basic assumption of these methods is that the conductivity distribution is approximately homogeneous. Examples of these linear approximation methods include the Barber-Brown *backprojection* [Barb83 and Avis95] and related methods [Guar91 and Barb93]. Single-step methods produce an image using the single application of a mathematical operation [Boon97]. Single-step methods can generally be divided into two broad categories: *backprojection* [Barb93] and *sensitivity matrix* [Gadd92 and Moru94] methods.

Iterative techniques are nearly always used to try to solve the 'static' reconstruction problem, i.e., find the actual resistivity in the body rather than a change in resistivity. These include Wexler, Fry, and Neuman's double constraint algorithm [Wexl85 and Wexl88] and a variant [Kohn87]. These methods generally solve a series of linear problems via solution of the Poisson or Laplace (see Equation 1.0) electromagnetic

equations (i.e., the forward problem) in an attempt to solve the full nonlinear problem (i.e., reconstruction of the unknown impedance distribution or inverse problem, see Figure 1.0). Poisson's relation for a continuous inhomogeneous medium is:

$$-\nabla \cdot \kappa \nabla \phi = f \qquad [1.0]$$

where κ, ϕ, and f are the conductivity, potential distributions, and impressed current source distributions within the region being studied, respectively. Most of these methods acknowledge the non-linearity and ill-posedness of EIT (discussed fully later) and attempt to treat it without linearization, unlike non-iterative methods. The mathematical basis of an iterative image reconstruction technique, using the Wexler algorithm [Wexl85] or the Kohn-Vogelius variant [Kohn87] as an example, is discussed in detail in Appendix II.

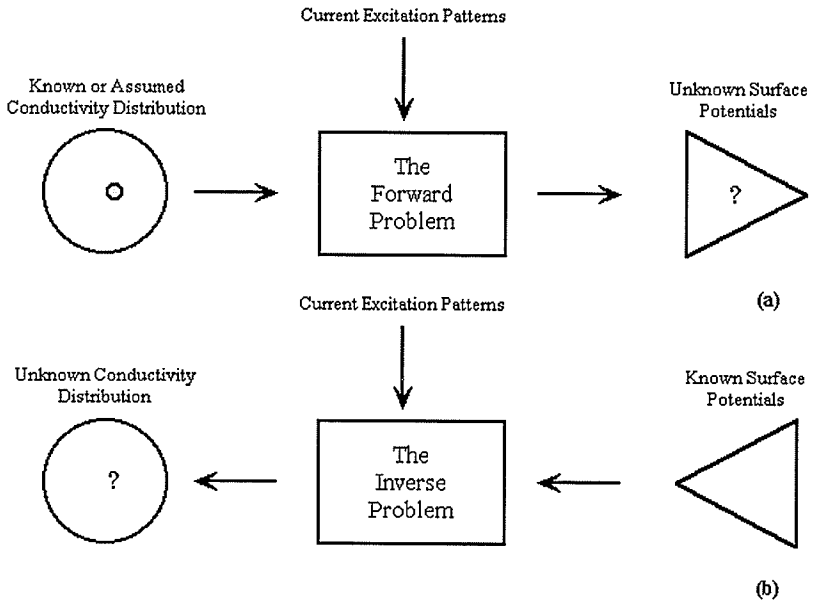

Figure 1.0: The Forward Problem (a) and the Inverse Problem (b) in Electrical Impedance Tomography. In the Forward problem, a known or assumed impedance distribution is used to calculate surface potentials from applied currents. In the Inverse Problem, the measured potentials and applied currents are used to solve for the unknown conductivity distribution.

Kyriacou *et al.*, 1990 [Kyri90] and Yorkey *et al.*, 1988 [York88], have published excellent reviews comparing the different reconstruction algorithms for EIT. What follows is a summary of the fundamental differences. Although there are many different single-step methods, they can be divided into two broad classes, *backprojection* and *sensitivity matrix*, as stated previously. The most widely used backprojection technique is that first described by Barber and Brown [Barb83]. These authors transformed the normal curve isopotential lines into a conformal space where backprojection occurs along parallel lines. This process allowed the calculation of coefficients for the backprojection operator. Each image pixel then had to be "weighted" to compensate for the non-uniform angular distribution of backprojection lines through that point. Variants of the Barber and Brown methods are quite popular in the literature [Bayf95 and Kotr94].

The other broad class is that of the sensitivity matrix approach [Moru94]. The sensitivity matrix is the matrix of values by which the conductivity values can be multiplied to give the electrode voltages. In other words, multiplication by the sensitivity matrix is equivalent to an approximate solution to the forward problem. The sensitivity matrix uses a theorem derived by Geselowitz [Gese71]. To reconstruct an image, the sensitivity matrix needs to be inverted. A number of specific techniques to accomplish this step have been published [Gibs98 and Gadd92].

These linearization methods are very attractive due to their mathematical simplicity and computational speed, but they have the effect of ignoring the non-linearity of EIT. Furthermore, there are a number of undesirable features common to them. In particular, the recovered images of a centrally-placed object appears physically larger than that of a peripheral one of equivalent size, and underestimation of overall difference in resistivity is normally greatest for centrally-placed objects [Boon97].

As mentioned above, it is primarily the accuracy of the guess at the conductivity distribution stage, which distinguishes one iterative reconstruction technique from another. Many iterative algorithms have been published in the literature. Among the iterative techniques are variants of the Newton-Raphson method [York 88, Boon97 and Kotr97] and variants of the error function minimization algorithm [Kohn87]. Error function minimization algorithms minimize an error function based on the differences of potential distribution solutions compared to an initial assumed conductivity distribution. The conductivity distribution is updated by minimizing the error function with a least-square technique. Such algorithms include the Wexler EIT algorithm and its variants [Kohn87]. There seem to be two particular limitations, though highly disputable, to the iterative approach:

- The iterative process is perceived as being sensitive to noise and measurement error.
- Convergence to a solution is observed to be relatively slow and thus the image reconstruction process is computer intensive.

1.6 A Review of Breast Cancer Imaging Modalities

According to Canadian Cancer Statistics[3], breast cancer continues to be the most frequent type of cancer diagnosed among Canadian women. Canada's incidence rates are among the highest in the world, second to the United States. In Canada, an estimated 18,700 new cases of breast cancer will be diagnosed in 1999. During their lifetime, 1 woman in 9 is expected to develop breast cancer and 1 woman in 25 is expected to die from it. The statistics are less alarming in male breast cancer, an infrequent and rare occurrence, accounting for 1% of all breast carcinoma [Bodn99]; although detection is often at advance, incurable stages.

Currently breast cancer can be detected in three principal ways: (1) conventional x-ray mammography; (2) breast examination by a trained health professional; or (3) self-examination. Any means to detect breast cancer before the onset of symptoms is termed screening. Presently, conventional x-ray mammography is the most effective method of screening for breast cancer. However, the technique is not without limitations [Kerl97, Huyn98, Jato99, and Gord99]. With mammography, there are problems distinguishing malignant from benign tumours [Pate98]. Three of four lesions that it detects are benign, resulting in unnecessary costly follow-up medical procedures [Bren97]. In addition, 5 - 10% of breast cancers are undetected mostly in young women with dense breast tissue [Cohe85, Shaw90, Yell91, Benn91, and Hind99]. The X-ray dose of standard mammography causes breast cancer in and kills one woman for every eight saved from the disease [Rick99].

While many ways are being explored to prevent and treat breast cancer, early detection is a woman's hope for effective treatment and better survival rates. Breast lesion size has a direct correlation with survival: a lesion increases 8 times in size from the time it is a non-palpable 0.5 cm to the time it reaches a palpable size of 1 cm. Sivaramkrishna and Gordon (1997), in a quantitative analysis, have shown that the probabilities that 1 cm and a 2 cm lesions have metastasized are approximately 7.31%

[3] National Cancer Institute of Canada: Canadian Cancer Statistics 1999, Toronto, Canada, 1999.

and 25.5% respectively. The authors concluded that detection of very early tumours ought to substantially reduce the likelihood of metastatic spread [Siva97].

The limitations of conventional mammography create the need for new technologies that could detect and diagnose breast cancer at an early stage, thereby eliminating unnecessary biopsies and providing more information about the extent of cancer growth and improving prognosis. Magnetic resonance imaging (MRI), ultrasound (US), computerized tomography (CT), positron emission tomography (PET), and nuclear medicine (NM) are among a few modalities presently under investigation for breast cancer screening [Ziew99]. These modalities, however, are not without limitations. MRI brings the advantage of high-resolution 3-D imaging to breast cancer staging (usually based on the size and degree of tumour spread) and treatment evaluation. However, MRI without contrast media thus far has failed to demonstrate sufficient sensitivity and specificity to justify the enormous expense and time needed to perform these studies [Kram98 and Skaa98]. Ultrasound has demonstrated efficacy in the differentiation of cysts from solid lesions but is unreliable for the differentiation of benign from malignant solid lesion [Samu98]. CT offers essential information that can alter treatment planning and optimize treatment strategy but would likely be restricted, in breast tumours diagnoses, due to the relatively high level of radiation exposure presently employed [Trig99]. Larger trials are necessary to establish whether positron emission tomography and radionuclide scanning would provide any efficacy in screening for asymptomatic breast malignancy [Wahl98]. PET and NM would likely be limited by the requirement for the injection of radioactive material. At the outset, it appears that these new imaging modalities, for reasons outlined above, might not be appropriate in screening for breast cancer but could prove effective as diagnostic aids if they replaced less accurate tests, eliminated biopsies, and improved treatment planning [Cole98].

Can EIT be used as a breast cancer imaging (viz., detection and diagnosis) technique? Can it be used to detect breast cancer before the onset of metastatic spread? What are the limitations of the technique in the full nonlinear reconstruction of absolute resistivity 'static' imaging? Although, the research efforts and accomplishments of a few EIT groups [Cher95 and Chen99] engaged in EIT hardware development deserve recognition, the transition of EIT from the laboratory to the clinic has yet to occur. The main problem appears to be software related. In particular, the limitation in spatial resolution is usually attributed to the lack of an efficient and robust EIT algorithm capable of producing clinically useful images. Recent developments in 3-D EIT appear to be quite promising for clinical applications [Meth96]. However, before EIT can be established as a complementary tool to mammography or as the technique of choice in the detection of breast cancer, the questions raised earlier, and many more, need to be fully resolved.

1.7 Purpose and Outline of Thesis

In Chapter 2, an analytical and critical review of 'dielectric' properties of breast tissue is presented. A review of the histopathological development of breast cancer in Chapter 2 reveals some important requirements for an EIT-based imaging algorithm, in particular, the optimal detection size for a good prognosis. The original Wexler EIT algorithm is presented in Chapter 3. Simple two and three-dimensional computer simulations of breast cancer imaging are performed to illustrate the method. In Chapter 4, several tests are conducted, via simulations, on the original algorithm in order to understand its fundamental characteristics and "dynamics". Among the tests carried out were the algorithm's ability to handle noise, its effect on image quality due to patient motion, and other considerations that are prevalent in clinical situations. The objectives are to evaluate the algorithm's clinical ability and subsequently to identify "areas needing improvement". Two most crucial "areas needing improvement" were identified for the success of the algorithm in the detection of early stages of breast cancer (i.e., at relatively small size of 1- 2mm in diameter). These were the low convergence rate and the limited spatial resolution of the recovered images of the original algorithm. In Chapter 5, a Modeller-Predictor-Corrector (MPC) scheme - that incorporates a modified Levenberg-Marquardt (LM) least-squares fitting algorithm - is devised and implemented in the Wexler algorithm in order to improve its convergence rate. The issue of low spatial resolution is addressed in Chapter 6. A novel technique, which combines the Peak Detection Method, an image- processing algorithm, and a revised localized conductivity compensation scheme, collectively referred to here as the Locator-Compensator (LC) method, is developed to investigate EIT's limit of spatial resolution. By combining the development of the two previous chapters, an improved Wexler 3-D EIT algorithm is presented in Chapter 7. This improved algorithm is demonstrated using realistic computer simulations of small breast tumours. A thorough discussion of the objectives of this thesis is provided in Chapter 8. Conclusions and future work are discussed in Chapter 9.

Chapter 2

Breast Tissue: A Review of Histopathologies and Dielectric Properties

2.1 Introduction

Electrical or dielectric[4] properties of normal and malignant human breast tissue at both radiowave and microwave frequencies have been investigated since as early as the mid-1920. A knowledge of dielectric properties of tissue is important for several reasons, most importantly to: 1) provide a better understanding of the biophysical mechanisms involved in EM radiation-tissue interaction [Bern79, Leve84, and Isma98]; 2) assess the potential of induced local hyperthermia, as a technique in cancer treatment, from a knowledge of the differential dielectric properties over a wide range of frequencies [Conw92, Hawl92, and Gers99]; and 3) evaluate the possibility of noninvasive EM radiation-based imaging techniques [Pric79, Soll81, Wtor99 and Rada99]. In principle, the latter ought to be possible due to the observed differential dielectric properties between normal and diseased breast tissue [Suro88 and Mori90] over some frequency range. Because of the importance of the last objective, and the recent interest in an EM radiation-based imaging technique as a potential screening tool for breast cancer, an objective analytical and critical review is presented at both radiowave and microwave frequencies.

---

[4] There is much confusion in the literature about nomenclature use in describing the electrical properties of tissues. In this thesis, the most commonly used terminology is employed. The microscopic electrical properties that describe the interaction of an EM wave with matter are the complex conductivity σ^* and the complex permittivity ε^*. As described by Rigaud *et al.*, 1996 [Riga96b], although, "the term 'dielectric' is typically associated with substances capable of storing electrostatic energy, it is also used for any system capable of polarizing itself under the effect of an electric field". In many instances, the term 'dielectric' is used to describe electrolytes and certain noninsulating media such as biological tissues. As such, the trend in the literature has been in using complex conductivity and permittivity to describe the properties of tissues at the microscopic level and complex impedance, the more general quantity, for defining the electrical behaviour on a macroscopic level.

To understand the concept of dielectric properties of a tissue, a brief summary of the mathematical background and fundamentals is provided. Prior to the review, a discussion on the manner in which breast cancer arises and progresses (i.e., its histopathological development) is given. The purpose of the discussion on the histopathology of breast cancer is to derive some fundamental requirements expected of an EIT-based breast cancer screening system. These requirements are then used to evaluate published studies on the dielectric properties of the breast at both radiowave and microwave frequencies.

2.2 Mathematical Background on Dielectric Properties of Tissue

A large amount of data on the dielectric properties of tissue has been accumulated in the literature, starting with the early work of Fricke [Fric26], Cole and Cole [Cole42], Geddes and Baker [Gedd67], and Foster and Schwan [Fost86]. Recently, Gabriel and Gabriel [Gabr96] compiled an extensive survey on the dielectric properties of tissues at radiowave and microwave frequencies. In a 1989 article, Foster and Schwan provided a comprehensive review of the dielectric relaxation mechanisms of tissue [Fost89]. Duck summarized the dielectric properties of tissues covering the frequency range from d.c. to over 10 GHz [Duck90]. Some definitions and basic mathematical concepts of the dielectric properties of tissue are discussed below.

The electrical characteristics of tissues covering the frequency range from radiowave to microwave can appropriately be described by using the properties: relative permittivity, ε', and conductivity, σ [Fost89 and Riga96a]. The relative permittivity and conductivity are, respectively, the charge and current densities produced in a medium (e.g., tissue) in response to an applied electric field of unit amplitude. Using the approach of an idealized parallel-plate capacitor, Foster and Schwan [Fost89] derived an expression for complex conductivity and relative

permittivity as a function of frequency (see Table 2.0). The lengthy derivation is summarized here:

The complex conductivity, $\sigma *$, of a material is defined as,

$$\sigma * = \sigma + j\omega\varepsilon\varepsilon_0 \qquad [2.0]$$

where σ is the dielectric static conductivity, j is $\sqrt{-1}$, ω is the angular frequency, ε is the dielectric static permittivity, and ε_0 is the permittivity of free space (i.e., 8.854×10^{-12} F/m) respectively.

Similarly, the complex permittivity, $\varepsilon *$, is defined as:

$$\varepsilon * = \varepsilon' - j\varepsilon'' \qquad [2.1]$$

Conductivity, σ, is defined as the conductance of a unit volume of matter and has units of Siemens meter^{-1} (S m^{-1}). Conductivity usually has a frequency-independent part (due to ionic conduction), a frequency-dependent component (due to dielectric relaxation), and ε'' equivalent to $\sigma/(\omega\varepsilon_0)$, usually referred to as the "loss", is sometimes used with reference only to the frequency-dependent part of the conductivity. In the literature there are many references to the "dielectric constant" of a material, by which is meant the real part of the complex permittivity (i.e., ε'), typically at low frequencies, at which ε' is independent of frequency. "Permittivity" or "relative permittivity", is usually used to indicate the real part ε' of the complex permittivity, $\varepsilon *$, relative to that of free space, ε_0.

The complex conductivity $\sigma *$ and permittivity $\varepsilon *$ are related by,

$$\sigma * = j\omega\varepsilon_0\varepsilon * \qquad [2.2]$$

from which the complex impedance of a material, Z^*, can be derived as,

$$Z^* = \frac{1}{\sigma *} \qquad [2.3]$$

In some papers, resistivity ρ is used. This is the inverse of conductivity, $\rho = \frac{1}{\sigma}$. A more comprehensive derivation can be found in Foster and Schwan [Fost89].

Table 2.0: List of parameters employed to describe 'dielectric' properties of tissues or biological materials at lower frequencies.

Parameters	Description of Parameters
σ^*	Complex Conductivity
σ	Static Conductivity
ε^*	Complex Permittivity
ε'	Permittivity or Relative Permittivity
ε_0	Permittivity of Free Space
Z^*	Complex Specific Impedance
ε''	Loss
ρ	Resistivity

The resistivity of many tissues is anisotropic (i.e., their electrical properties depend on the direction of measurement). For example, skeletal muscle conducts electricity relatively better longitudinally than transversely. Anisotropy is crucial for the uniqueness of a solution [Sylv86 and Lion97]. As such, anisotropy effects ought to be considered during reconstruction of electrical impedance images [Eyub92 and Glid97]. However, breast tissue is mostly isotropic. It consists of fibrous and fatty tissues, which for the most part can generally be considered as being isotropic but heterogeneous.

2.3 Anatomy and Histopathology of Breast Cancer

The breast, or mammary gland, begins developing in the embryo about 7-8 weeks after conception. From about 12-16 weeks, epithelial buds develop and branch out to lay the foundation for future ducts and milk producing glands [Folk85]. Similarly, other tissues develop into muscle cells that will form the nipple and areola (the dark region around the nipple). At 20-32 weeks, these buds canalize to form lactiferous/milk ducts. From infancy to puberty, there is no difference between the female and the male breast [Rava98]. However, with the onset of puberty, the female breasts undergo dramatic changes. The estrogen effect stimulates longitudinal ductal growth and the formation of terminal ductal buds. Further glandular development occurs in response to progesterone, in particular, the formation of lobules. In the last 8 weeks of pregnancy the lobules mature and increase in complexity in preparation for lactation. This process approximately takes 3-4 weeks.

The adult female breast is composed of essentially three basic structures: the skin, the subcutaneous and interparenchymal fat, and the breast tissue, which includes the parenchyma and the stroma (see Figure 2.0) [Folk85]. Simply stated the breast is made up of primarily the milk-producing glands and the network of larger and larger ducts that conduct milk from the glands to the nipple. The glands and ducts are organized into lobes and lobules. The parenchyma contains about 15-20 lobes, each of which is drained by a lactiferous duct. The breast itself lies on the pectoralis muscles, which cover the chest wall.

Microanatomically, the basic histopathologic unit of the breast is the terminal duct lobular unit (TDLU). The TDLU is composed of the smallest branches of lactiferous ducts, the extralobular terminal duct and the lobule. The lobule is composed of the intralobular duct and the ductules [Well75]. The ducts and the lobules are the sites where most breast abnormalities arise, both benign and malignant. The size of the ducts is approximately 1- 2mm in diameter.

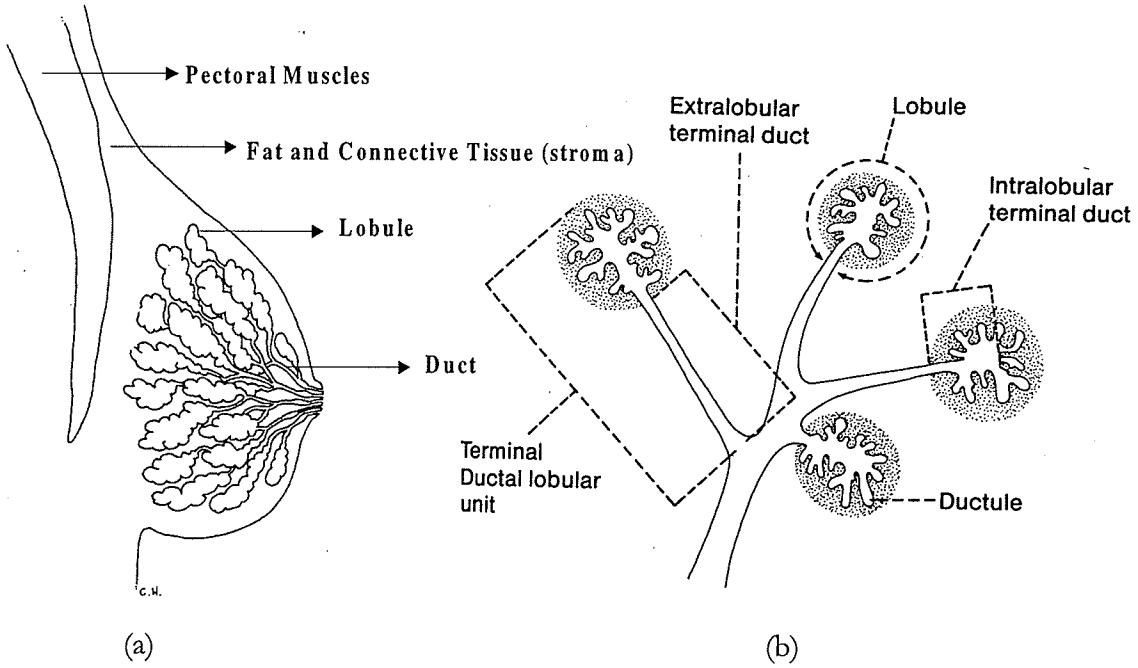

* Reprinted, with permission, from reference [Shaw92].

Figure 2.0: This shows (a) the gross anatomy and (b) terminal duct lobular unit (TDLU) of the normal breast. The three main component of the breast are identified as the glands, the network of ducts, and the lobules. The TDLU consists of the lobule, intralobular terminal duct, and ductule. The average size of the ducts is approximately 1- 2 mm in diameter. The size of the duct is of great interest to EIT imaging of early breast tumours.

There is no known single cause of breast cancer. However, genetic and/or hormonal factors may play a role in some patients [Land88, Will88, and Paul90]. What is generally known about the natural history of breast cancer, and has come to be accepted as the model of progression, is that in the early stages, up to the point of initial invasion, it forms a linear sequence. The sequence of events within this period is predictable and the probability of regional or systemic spread is low. After significant mass formation has occurred, the course becomes more randomized. This formulation supports the importance of early detection and treatment [Tubi91 and Tubi99]. Furthermore, as tumour size increases, the likelihood that distant metastasis has taken place rises and there appears to be a critical volume before which distant metastasis does not occur [Kosc84]. For this reason, screening patients for breast cancer before tumours are large enough to be palpable has been proposed as a way to decrease the risk of dying of the disease [Holm89, Fryk90, Cris93, and Peer96].

Histopathology is the study of the effects of disease on tissue. Histopathological classification of breast cancer helps in establishing the diagnosis of the lesion and appropriate determination of patient treatment and prognosis. Breast cancers are usually classified histologically based on the types and patterns of cells that compose them. Carcinomas can be invasive, extending into the surrounding stroma (i.e., fat and connective tissue) through which tumour cells spread locally, regionally, and distantly via vascular lymphatic space, or noninvasive (e.g., ductal carcinoma in situ) which is confined just to the ducts or lobules [WHO82]. Invasive carcinomas are commonly divided into two major types: ductal and lobular. Figure 2.1 below summarizes the most documented histologic types of invasive, non-invasive, and special variants (i.e., those with distinct morphology and prognosis) of breast carcinomas. Morphology is the study of structure or form and the features comprised in the form and structure of an organism or any of its parts.

Carcinomas have a propensity to spread via lymphatics. Breast cancers, when they metastasize, often go first to the axillary lymph nodes where most lymphatics from the breast drain. Other organs can be sites where metastases lodge, and such sites as lung, bone and liver are more common. Among the least aggressive cancers are non-invasive intraductal and lobular carcinoma in situ. Carcinomas, which can potentially metastasize but less commonly do, are: colloid, medullary, and papillary carcinomas.

The majority of ductal carcinoma is thought to develop in the terminal duct branches, and the calcifications associated with these lesions tend to have a linear, branching orientation or configuration, corresponding to the duct lumen. Lobular processes are often benign, and include many forms of fibrocystic changes (i.e., adenosis, sclerosing adenosis, and cystic hyperplasia). Associated calcifications are more smoothly marginated and rounded, conforming to the configuration of the ductules.

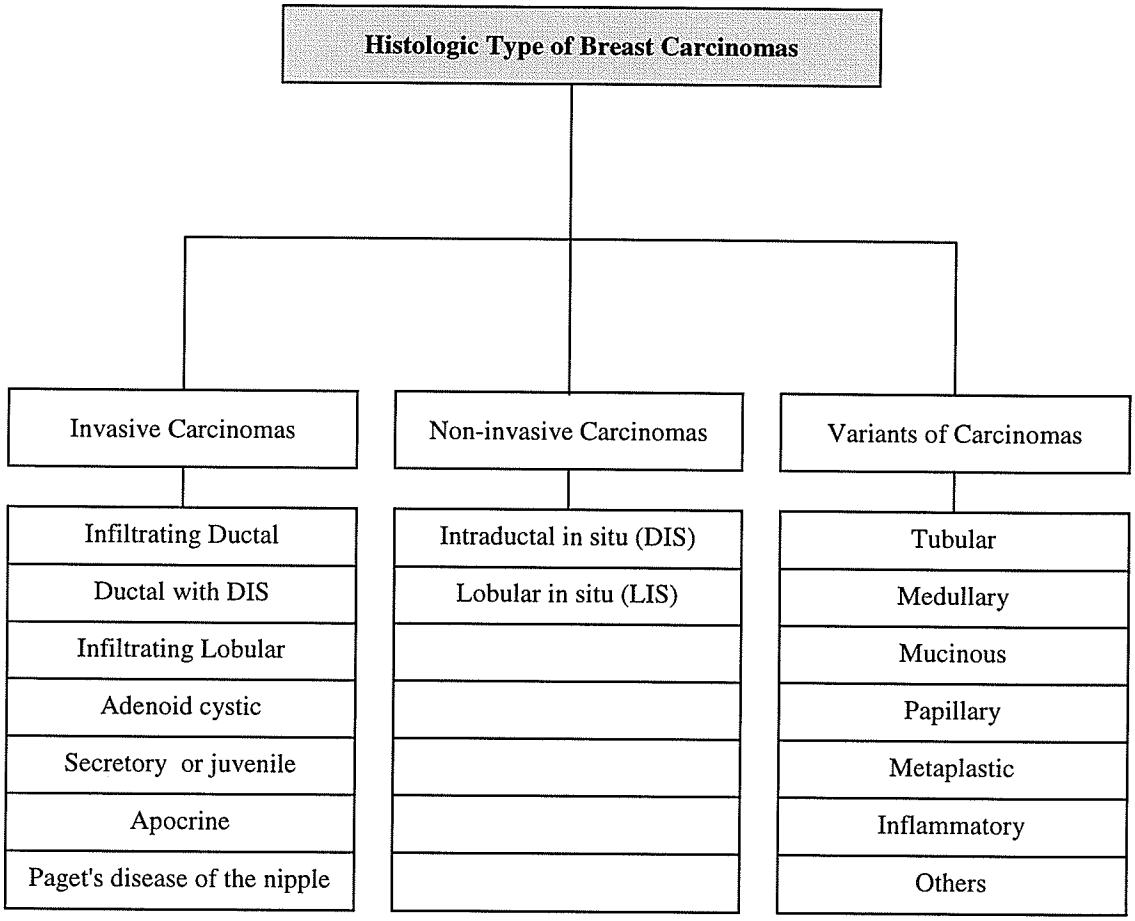

Figure 2.1: The most common histologic classification of breast cancer. Breast cancer histologic types are generally divided into three main categories: Invasive, non-invasive, and variants of invasive and noninvasive. This broad classification is gathered from the WHO histological typing of breast tumours, see reference [WHO82].

The stage of breast cancer is based on its size and degree of spread. Traditionally, the staging system consists of primarily four stages as identified in Table 2.1. In Stage I, the actual tumour is generally no longer than 2 centimeters (i.e., 2 cm) and has not spread to the rest of the breast. In Stage II, any of the following may be true: the tumour is no longer than 2 cm but has spread to the lymph nodes; the tumour is between 2-5 cm and has or has not spread to the lymph nodes; or the tumour is larger than 5cm and has not spread to the lymph nodes. Stage III is usually divided into Stage IIIA and IIIB. In Stage IIIA, the tumour is larger than 5 cm and has

spread to the lymph nodes under the arm, and in Stage IIIB, the tumour has spread to the lymph nodes inside the chest wall along the breastbone. In Stage IV, also called the metastatic cancer, the tumour has spread to other organs of the body.

The most precise system for cancer staging is considered to be the TNM (Tumour-Nodes-Metastases). The TNM staging system was developed by the American Joint Committee (AJC) on Cancer Classifications and is used to stage breast cancer. In the TNM staging system, the tumour, lymph nodes, and metastatic spread are assessed separately. Each letter is followed by a digit that identifies the severity of the condition, (see Figure 2.2 below). As an example, a patient diagnosed with T2N2M1 has tumour growth from 2-5 cm, which has spread to the lymph nodes and have grown together or into other structures under the arm, and has distant metastases or skin recurrence beyond the breast area.

Table 2.1: The Traditional Staging of Breast Cancer (based on size and degree of spread).

Staging		Definition
Stage I		- Tumour 2 cm or less in diameter and without evidence of spread
Stage II		- Tumour is no larger than 2 cm and has spread to the lymph nodes - Tumour is between 2-5 cm and has or has not spread to the lymph nodes - Tumour is larger than 5 cm and has not spread to the lymph nodes
Stage III	Stage IIIA	- Tumour is larger than 5 cm and has spread to the lymph nodes
	Stage IIIB	- As in Stage IIIA, and has spread to lymph nodes inside chest wall
Stage IV		- Tumour has spread to other organs of the body

2.4 Diagnoses via Mammography

Among the abnormalities found on mammography are masses and calcifications. Evaluation of a mass lesion is first characterized by its margination, whether it is relatively well circumscribed or spiculated and poorly defined. Well-circumscribed masses with smooth margins usually represent benign lesions such as fibroadenomas, hematomas, and papillomas. Although well-circumscribed masses are most likely benign, some malignant cancers also may well be defined (e.g., infiltrating ductal carcinomas). Irregularly shaped masses with poorly defined or spiculated margins may be an indicator of malignancy [Shaw92].

Calcifications are tiny specks of calcium seen on mammograpy. The analysis of calcifications is based on assessment of prior mammograms of morphologic features, size, distribution, location, and stability. Calcifications that are widely scattered, of uniform size, and well defined are usually representations of benign conditions. These include fibroadenomas, fat necrosis, and oil cysts. Irregular calcifications that are heterogeneous in size and clustered together may indicate the presence of malignancy.

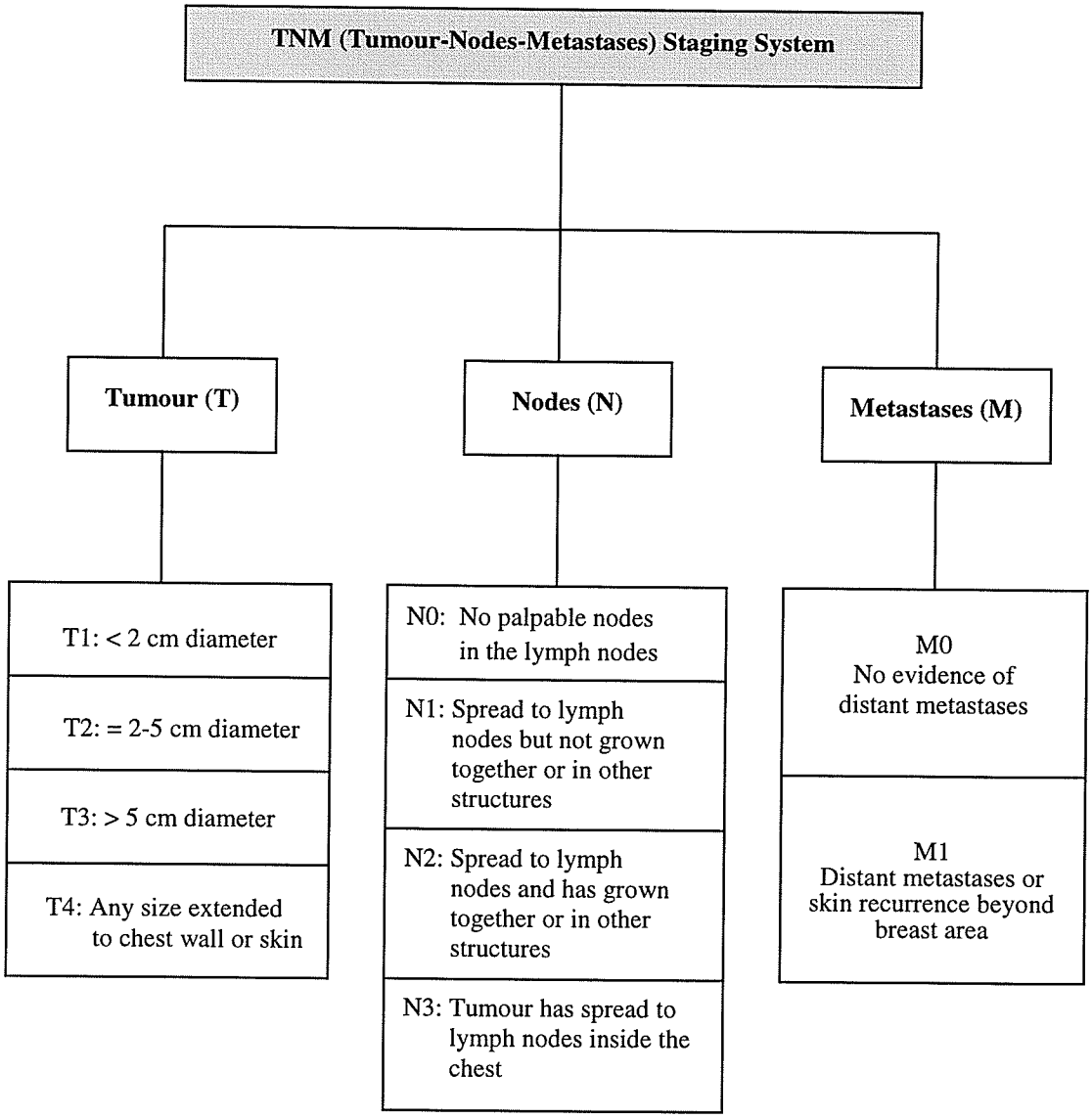

Figure 2.2: The TNM (Tumour-Nodes-Metastases) Breast Cancer Staging System. A new and revised TNM staging system can be found in the American Joint Committee on Cancer (AJCC) Staging Manual, 5th Edition, 1998.

Microcalcifications present more of a problem for mammography than calcifications, since microcalcifications can represent a malignant process [Taba85]. They can be divided roughly into two types based solely on their site of origin. Lobular calcifications tend to occur in the terminal ductules. Examples of processes that may result in lobular microcalcifications include seceral fibrocystic lesions (e.g.,

adenosis, sclerosing adenosis, cystic hyperplasia, and lobular hyperplasia) and lobular carcinoma in situ. There are other less common mammographic signs of carcinoma. These include dilated lactiferous ducts, focal areas of symmetry or architectural distortion, and thickening or retraction of the skin. These conditions are usually benign; however, in some indeterminate cases biopsies are required for proper diagnosis. More detailed discussion on mammographic pathological abnormalities found in mammogram can be found in the following references [Well75 and Rose87].

2.5 Literature Review on the Dielectric Properties of Breast Tissue

An EM-based screening tool (e.g., EIT) will only be effective if adequate impedance variation exists between normal, benign and malignant breast tissues. It is well known that cancerous and normal tissues differ morphologically, histopathologically, and physiologically [Kino 88 and Blad95]. These differences have been known to induce changes in their electrical properties and as such, had prompted many investigators to explore tissue (viz. normal and cancerous) characterization. Of great interest, both from a screening or therapeutic point of view, is the characterization of the biophysical features of cancerous breast tissue. To this end, an analytical and critical review of the literature on the dielectric properties of breast tissue at both radiowave and microwave frequencies is presented. The purposes of this review are to objectively assess published studies and discuss their findings.

Only a few sets of useful data on the dielectric properties of normal and malignant breast tissues have been published. Fricke & Morse [Fric26] found significantly higher permittivity of breast tumour tissue at 20 kHz as compared to normal or malignant tissues in vitro. England & Sharples [Engl49] and England [Engl50] discussed the dielectric properties of breast fat and carcinomas at 3 GHz. Based on the observations of [Engl49] and [Engl50], Mallard *et al.* 1967 postulated the potential use of microwave-based measurements for tumour detection [Mall67].

Chaudhary *et al.* [Chau84] studied the dielectric properties of breast carcinoma and normal tissues at frequencies from 3 MHz to 3 GHz in vitro. They found significant differences in the dielectric properties of normal and malignant tissues, in particular at frequencies below 100 MHz, and suggested the use of EM-based radiation scanning for detection of an early stage of breast cancer. Sollish *et al.* [Soll81] developed an in vivo dielectric breast scanner based on assumed differential dielectric properties of normal to malignant breast tissues. Surowiec *et al.* [Suro88] studied the electrical properties of breast carcinomas and surrounding tissues from 20 kHz to 10 MHz in vitro. They further observed differences in the dielectric properties (viz., the real component of conductivity and permittivity) of normal and malignant breast tissues and indicated the potential of impedance imaging as a diagnostic tool.

Mitsuyama *et al.* [Mits88] measured the electrical impedance of breast tumours in vivo. Morimoto *et al.* [Mori90] and [Mori93] published in vivo data on bio-impedance measurement of breast tumours between the frequency range (0 – 200 kHz) and further confirmed the significant differences in dielectric properties of normal and malignant breast tissues. Rigaud *et al.*, 1996 published a summary of published works on the in vitro and in vivo characterization of breast cancer tissues [Riga96]. Jossinet [Joss96] investigated the variability of impedivity (the equivalent for a.c. of electrical resistivity, ρ, for d.c.) in normal and pathological breast tissue over the frequency range (0.448 kHz – 1 MHz) [Joss96]. The results obtained by Jossinet [Joss96] are somewhat consistent with that of Surowiec *et al.*, [Suro88] and *Morimoto et al.*, [Mori93]. In Figure 2.3 below, the relationship between the in vivo and in vitro studies described earlier is shown.

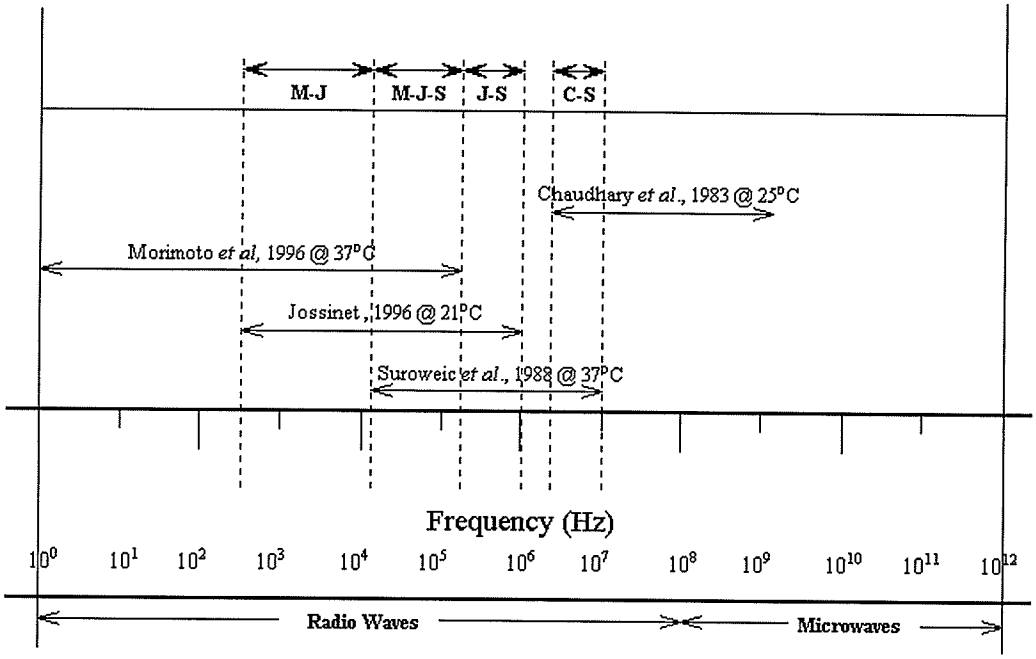

Figure 2.3: Relationship between published in vivo and in vitro studies on dielectric properties of breast tissues at radiowave and microwave frequencies. The region identified as M-J-S, is the frequency region at which the studies of Morimoto *et al.*, 1990, Jossinet 1996, and Surowiec *et al.*, 1988 overlap. Similarly, M-J, J-S, and C-S are the region at which Morimoto *et al.*, 1990 and Jossinet 1996, Jossinet 1996 and Surowiec *et al.*, 1988, and Chaudhary *et al.*, 1983 and Surowiec *et al.*, 1988 overlap.

The frequency region identified in Figure 2.3 as M-J-S (i.e., between 20 kHz to 200 kHz), is the region of frequency over which the studies of Morimoto *et al.*, 1990[Mori90], Jossinet, 1996 [Joss96] and Surowiec *et al.*, 1988 [Suro88] overlap. The overlap could provide a frequency region over which to compare the results of each study. However, they each had employed a different methodology for breast tissue characterization, and had made measurements on different breast cancer histopathologic types. Surowiec *et al.*, 1988 employed the experimental method of reflectometry on ductal carcinomas (invasive), Morimoto *et al.*, 1990 used a three-electrode probe method for in vivo measurements on papillotubular and solid-tubular carcinomas (variants of invasive carcinomas), while Jossinet, 1996 utilized a four-needle hand-held electrode probe to measure variability of impedivity in six groups of breast tissue, with no mention of histopathological type. Others have employed different approaches [Chau84, Camp92, and Blad95].

Among the studies mentioned above, the work of Surowiec *et al.*, 1988 [Suro88] appears to be the most reliable. Since measurements were made on the central part of the tumour, on the tumour surrounding tissue, and on the peripheral tissue, and at normal body temperature, this approach reflects the general knowledge and understanding of the natural progression of breast cancer development. These measurements were performed strictly on infiltrating ductal and lobular (i.e., invasive) carcinomas, and the measurement frequency range (20 kHz - 100 MHz) is well within the frequency range (i.e., > 1 MHz) suggested by Jossinet, 1996 [Joss96]. This is not to say, in anyway whatsoever, that measurements at lower frequency, for example at 2 KHz, do not produce adequate variation in dielectric parameters for potential diagnostic purpose. The in vivo study of Morimoto *et al.*, 1990 [Mori90] had shown that significant variation exists at lower frequency for both benign and malignant tumour.

A property of breast tissue that is of great interest, in particular for the detection of tumours via EIT, is its dielectric (viz., conductivity or relative permittivity) property. Since the published data of Surowiec *et al.*, 1988 was identified to be more realistic, the difference in conductivity (i.e., the contrast) of the normal and diseased breast tissue was plotted in order to determine how much of a conductivity difference exists as a function of frequency. For the purpose of demonstration, a dimensionless parameter that quantifies the conductivity difference or contrast, C was introduced. Contrast C, is defined as the absolute value of the quotient of conductivity of the diseased tissue (σ_d) to that of the normal tissue (σ_d) as a function of frequency,

$$C = \left| \frac{\sigma_d}{\sigma_n} \right| \qquad [2.4]$$

where C is the difference or contrast in conductivity, σ_d is the conductivity of the malignant tissue in units of (mS/cm), and σ_d is the conductivity of the normal tissue

in units of (mS/cm), respectively. The conductivity contrast plot is shown in Figure 2.4 below.

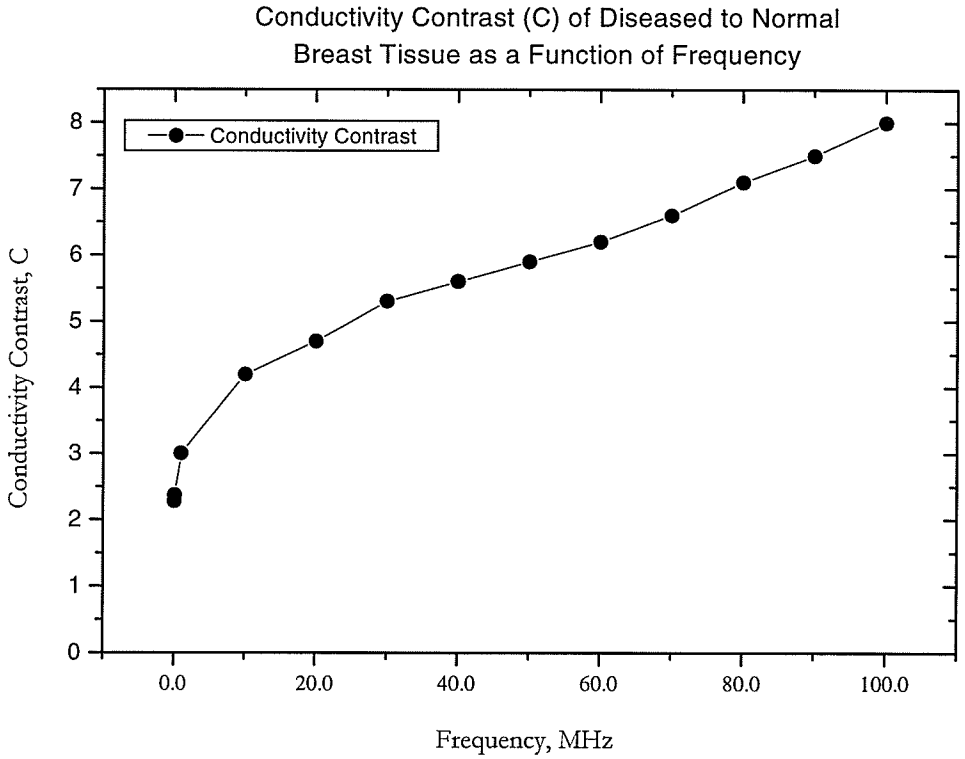

Figure 2.4: Real component of complex conductivity (i.e., conductivity) contrast, C, as a function of frequency for the published data of Surowiec *et al.* 1988. It is obvious that significant variation exists between normal and diseased breast tissue. This demonstrates that impedance imaging at radio wave frequencies has potential in the detection of breast tumours.

It is obvious from the contrast plot above that sufficient variation in conductivity exists between normal and diseased malignant breast tissue, in particular at frequencies above 1 MHz. This indicates that radio wave impedance imaging has potential as a breast cancer detection and as a diagnostic tool since adequate variation exists between normal and benign breast tissue as was also demonstrated by Morimoto et al., 1990 [Mori90] in the frequency range of 0-200 kHz. Based on the study of Morimoto *et al.*, 1990, an EIT machine operating, say at 2 kHz, ought to be

sufficiently adequate to produce virtually pure resistivity images of the diseased breast.

2.6 Discussion

A review of the literature on the histopathologies and dielectric properties of breast tissue was provided. The breast was identified as anatomically simple, consisting of three main components, the skin, the subcutaneous and interparenchymal fat, and the breast tissue, which includes the parenchyma and the stroma. Microanatomically, the basic histopathologic unit of the breast was identified as the terminal duct lobular unit (TDLU). The TDLU is composed of the smallest branches of lactiferous ducts whose average size is approximately 1 - 2mm in diameter. Such size imposes a crucial requirement on the sensitivity of a clinical or experimental breast cancer-screening system.

Since breast cancer is the most common cancer in women worldwide [Park93], its tissue characterization has aroused great interest both on the levels of screening and therapy [Riga96]. In the studies reviewed, it was observed that significant differences exist in the impedance properties of breast tissue (viz. normal, benign, and malignant) measured both in vitro, albeit with different experimental methods, and in vivo. In vivo breast tissue characterization studies are very scarce, mainly due to its complex technical requirements [Riga96]. It was determined that more extensive, particularly in vivo studies of dielectric measurements of breast tissue samples is needed to establish values more accurately from subject to subject (i.e., inter-subject variability) and to investigate the reality of any differences between the myriad of breast histopathological types.

If breast tumours are to be detected at a physical size at which the probability of metastatic spread is relatively low (i.e., within the range 1 - 2 mm in diameter or prior to Stage I and T1N0M0), an EIT system ought to be able to detect a breast tumour at the equivalent size of a basic unit of TDLU (i.e., the size of an average duct).

Following detection, an accurate diagnosis of the histopathological type of breast tumour, from the recovered impedance image of an EIT system, is anticipated. This imposed a further requirement on an EIT system, one of being able to distinguish between benign and malignant breast tumour from the recovered conductivity distribution.

2.7 Summary

The concepts and basic mathematics of dielectric properties of tissue were reviewed. The electrical characteristics of tissues covering the frequency range from radiowave to microwave can appropriately be described by using the properties: relative permittivity, ε', and conductivity, σ. The breast was identified as anatomically simple yet a prodigious producer of neoplasms (i.e., cancers). Excellent prognosis is anticipated with early detection (i.e., at a physical size of 1 - 2 mm), despite the histopathological variarion of breast carcinomas. From evidence obtained in the literature, mammographic screening can be quite unreliable. The general figure is that it misses 15% of tumours – though the size range of the missed tumours is not clinically known.

More extensive studies of dielectric measurements of breast tissue samples is needed to establish values more accurately from tissue to tissue and to investigate the reality of any differences between tumours and normal tissue. As far as EIT imaging is concerned, the most crucial feature of tissue impedance is the existence of sufficient variation between different tissue types to allow appropriate imaging. Such variations, from sparse data obtained so far, seem to be available.

Chapter 3

The Original Wexler 2-D and 3-D EIT Algorithm

3.1 Basics of the Original Wexler EIT Algorithm

The Electrical Impedance Tomography (EIT) algorithm discussed here was first developed and demonstrated by Wexler, Fry, and Neuman [Wexl85]. It has been further expanded in subsequent publications [Tamb87 and Wexl88] and in patent applications [Fry85], where the algorithm is called the "Electroscan" system. Similar algorithms have been published since [Kohn87], and the data processing method has recently been referred to as the "double-constraint algorithm" [Moru96] or the "Wexler Algorithm" [Cond96]. A review of the original Wexler EIT algorithm is presented here. Two- and three-dimensional computer simulations of breast cancer imaging, using the original Wexler algorithm, are performed and the results discussed.

The basic principle of the EIT algorithm is that the surface voltages (i.e., potentials) measured under a given current density are characteristic of a particular impedance distribution of a region/organ under investigation. In the original Wexler algorithm, the impedance distribution is determined from the field equations and subsequent estimates of the conductivity and resistivity distributions are calculated based upon differences between the computed field values and the actual measured values at the surface. An initial guess is made for the impedance distribution and the system is solved for the current distribution for one set of boundary conditions and the voltage distribution for a second set of boundary conditions. New impedance distributions are computed using these results. This is repeated until a threshold criterion based on the minimum of a residual obtained from these two calculations is reached (i.e., an error function minimization algorithm).

To demonstrate the computational Wexler EIT algorithm in the imaging of a 3-D object, a 3-D grid of nodes is defined over a cube (Figure 3.0). The cube is divided into a 3-D finite element mesh of *n* points. Measurement locations are shown around the 3-D object. A particular excitation pair is indicated centered at points *a* and *b*, and a reference node is at *r*. The total current flowing through the electrodes is *I*. At node points, located at mesh intersections, the potentials are computed for each excitation (or view), and the conductivity is then estimated within the intervening region inside the cube. An iterative approach, involving successive estimates of potential-conductivity-potential, etc., is employed, as shown in the flow chart of Figure 3.1.

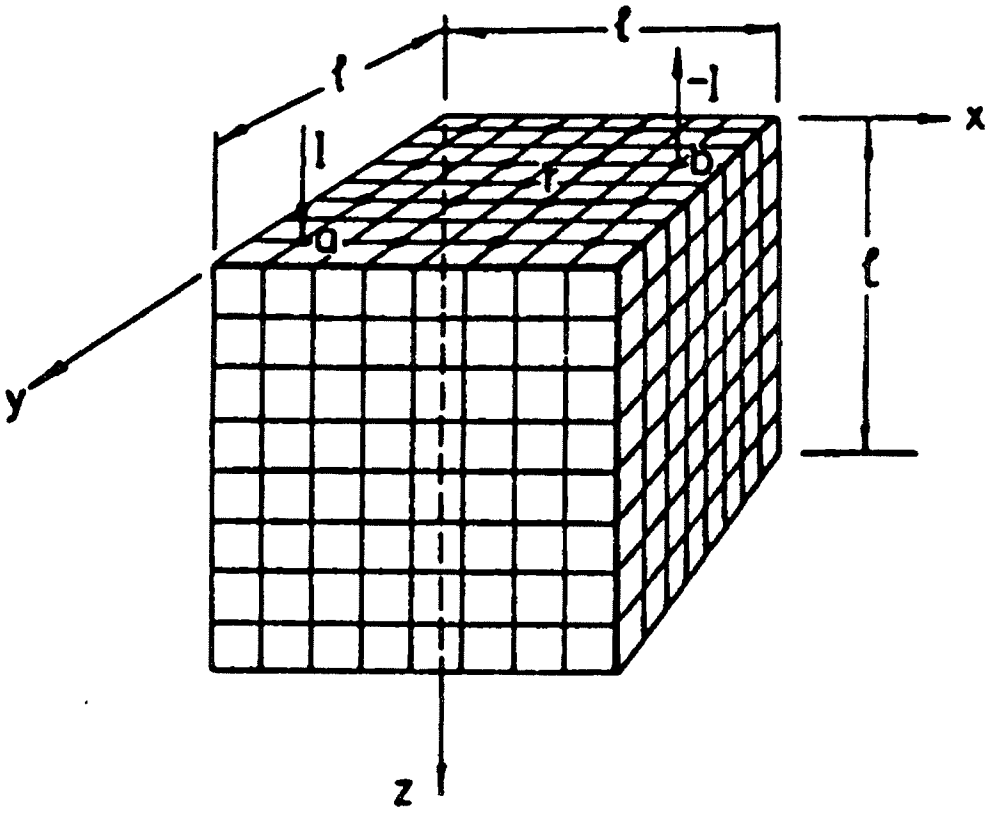

Figure 3.0: A 3-D imaging region. Region is divided into 3-D finite elements where *a* and *b* represent a particular excitation pair, and *r* is a reference node. An excitation pair is a pair of nodes where current is injected in one and measured at the other. Reprinted, with permission, from reference [Wexl85].

In summary, the algorithm proceeds as follows (see Figure 3.1):

Step 1. Calculation of ϕ and $\overline{J}$ with Neumann Boundary Conditions

Assume initially a homogeneous medium with constant conductivity (κ). The potential ϕ and the current flux density distribution $\overline{J}$ (A/m^2) are computed by solving Poisson's equation (1.0). The interior current distribution for each excitation case is determined by first solving for the interior potentials with the known impressed currents applied at appropriate surface node locations. For this scenario, the inhomogeneous Neumann current boundary condition:

$$\kappa(s)\left.\frac{\partial\phi}{\partial n}\right|_S = h(s) \qquad [3.0]$$

is specified; $h(s)$ (A/m^2) describes the electrical current flux density entering or leaving the breast over an electrode surface. With these boundary conditions and a conductivity distribution estimate throughout the interior, the voltage (potential) distribution throughout the interior of the breast is solved using a numerical technique, in particular the Finite-Element Method (FEM) [Redd93 and Silv96]. The FEM computes the field at node points for each excitation. At other points within the elements, ϕ is found by interpolation [Berr92]. Once ϕ is known, the electric field intensity $\overline{E}$, is given by the negative gradient of the potential, i.e.,

$$\overline{E} = -\nabla\phi \qquad [3.1]$$

Thus, with ϕ and $\overline{E}$ obtained, the electrical current density distribution is given by

$$\overline{J} = \kappa\overline{E} = -\kappa\nabla\phi \qquad [3.2]$$

which is Ohm's Law in point form [Wexl80] .

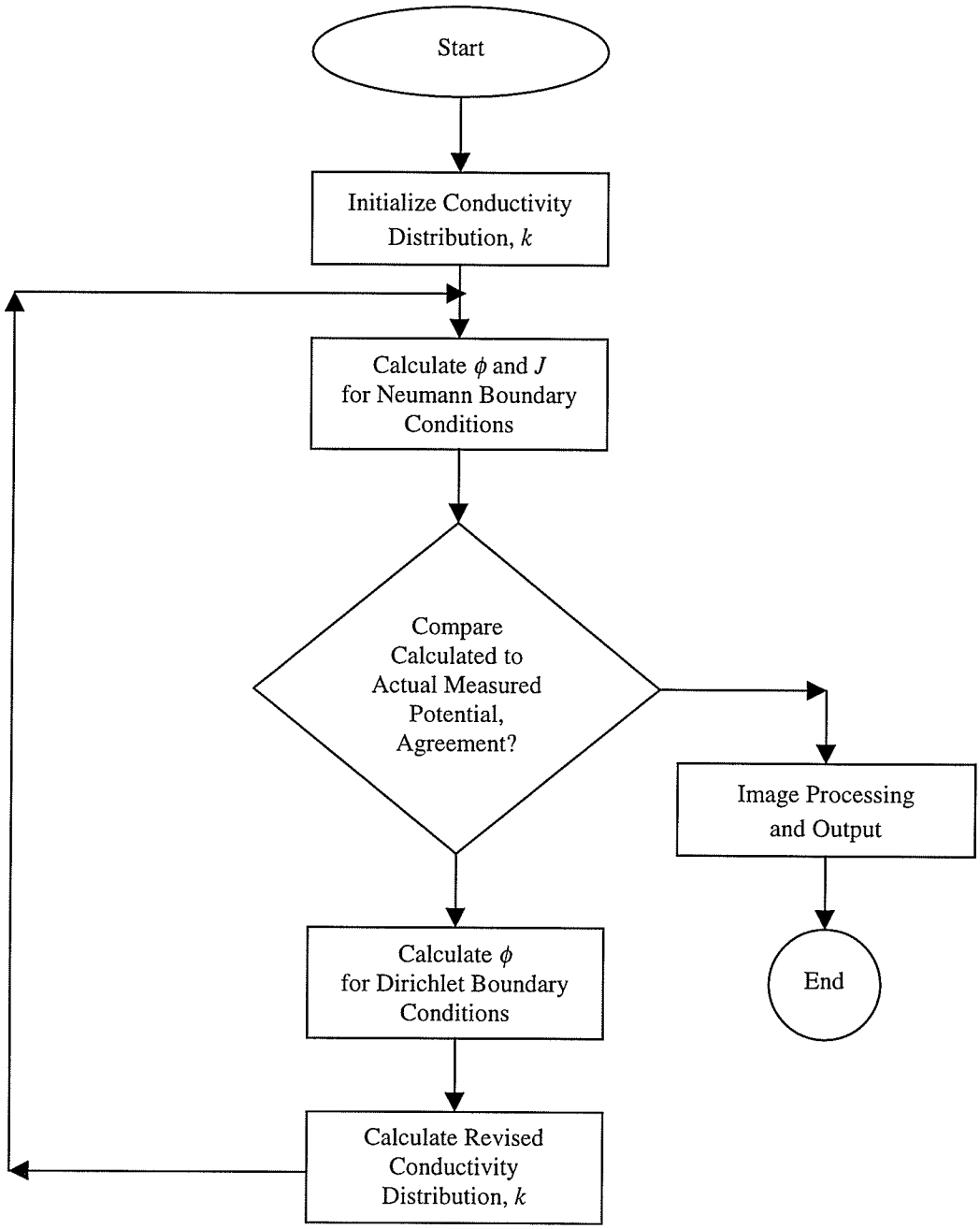

Figure 3.1: The original Wexler EIT algorithm flow chart. The algorithm is initialized using an assumed conductivity distribution. Potentials are computed for Neumann and Dirichlet boundary conditions over the volume and over all excitations. Resulting conductivity distribution is then compared to exact distribution. If satisfactory, the algorithm outputs the conductivity. If not, the potentials from Neumann and Dirichlet are used to compute a new or revised conductivity distribution and this succession continues iteratively until convergence.

The voltages computed from application of the Neumann current boundary conditions are then compared with the actual voltages measured. Unless the exact conductivity distribution κ is known in advance, there will be a discrepancy since κ is only an estimate at the outset. The procedure continues to Step 2.

Step 2. Calculation of ϕ with Dirichlet Boundary Conditions

The algorithm then uses the measured voltages to cause a change to the conductivity distribution to tend toward minimization of the differences between the measured and calculated surface voltages. This is performed by computing the interior potential distribution from application of Dirichlet boundary conditions while leaving the remaining Neumann boundary conditions unchanged.

Mathematically, the Dirichlet boundary condition is,

$$\phi(s) = g(s) \qquad [3.3]$$

where $g(s)$ is the boundary potential distribution.

This computation yields reasonable potential distribution patterns, even for very approximate conductivity distributions, due to the influence of the applied measured voltages acting on the interior region. A general-sparsity preconditioned conjugate gradient method is used to solve the resulting equations [Fry83].

Step 3. Calculation of Conductivity

Imposition of Ohm's law (3.2) over the interior region employing both the previously estimated $\overline{J}$ [Step 1] and ϕ [Step 2] for all excitations permits a conductivity distribution κ to be found that yields compatibility of the Neumann and Dirichlet boundary conditions. With $\overline{J}$ as calculated from Step 1 and ϕ as calculated from Step 2, Ohm's law is generally not satisfied. A residual R is obtained. To enforce compatibility, minimization of the square of the residual over all points and for all excitations is sought in a least square manner:

$$R = \sum_X \iiint_V (\overline{J} + \kappa\nabla\phi) \cdot (\overline{J} + \kappa\nabla\phi)\, dv \qquad [3.4]$$

where R is the square residual sum, V is the region over which the imaging is performed, and X represents the excitations over which the sum is taken. Minimizing and rearranging yields

$$\kappa_i = \frac{-\sum_X \iiint_{V_i} \overline{J} \cdot \nabla\phi \, dv}{\sum_X \iiint_{V_i} \nabla\phi \cdot \nabla\phi \, dv} \qquad [3.5]$$

where κ_i is a revised estimate of the conductivity within element *i*. Equation (3.5), which does not involve matrix operations, is applied to each element of the mesh in turn to update the conductivity distribution over the entire region within which the imaging is being performed.

Step 4. Recursive Improvement

With the new κ estimate computed in Step (3), the process is repeated iteratively from Step (1) until convergence as illustrated in the flow chart of Figure 3.1. The last step involves the processing and presentation of the impedance image. Procedures such as edge enhancement, histogram adjustment, and other image processing techniques are applied to the gray-level image obtained from transformation of the conductivity distribution at this stage. See Appendix I for a simplified discussion on the physical approach of the Wexler EIT image reconstruction technique.

3.2 2-D Computer Simulations using the Original Wexler 2-D EIT Algorithm

To demonstrate the potential of the original Wexler algorithm, 2-D and 3-D computer simulations were performed on a simplified model of the breast. These computer simulations, though not fully realistic, are nevertheless adequate representations of the problem under investigation (i.e., imaging of breast tumour).

In the simple 2-D case, a breast tumour is simulated within a homogeneous background at a conductivity ratio of 4.0:1.0 respectively (see Figure 3.2). The region is divided into 9×9=81 finite elements with 9 gauss points in each element (see Appendix II for a definition of gauss point). It is at these gauss points that functions

are sampled in order to evaluate the required integrals. Sixteen electrodes are arranged on the mesh boundary and eight pairs of current injections/extractions are applied. In order to eliminate contact resistance effects, potential measurements at active injections/extractions are not used in the computation. This scenario gives rise to 81 unknowns and 84 independent measurements (i.e., for the minimum number of excitations needed to recover the image, using the *sometimes* measurement pattern, and measured using a multi-probe extension of the four-probe technique, discussed fully in Chapter 4, Section 4.3). This setup corresponds to a determinacy of approximately 1.04, determinacy, being estimated as the ratio of the total number of independent measurements to the total number of unknowns.

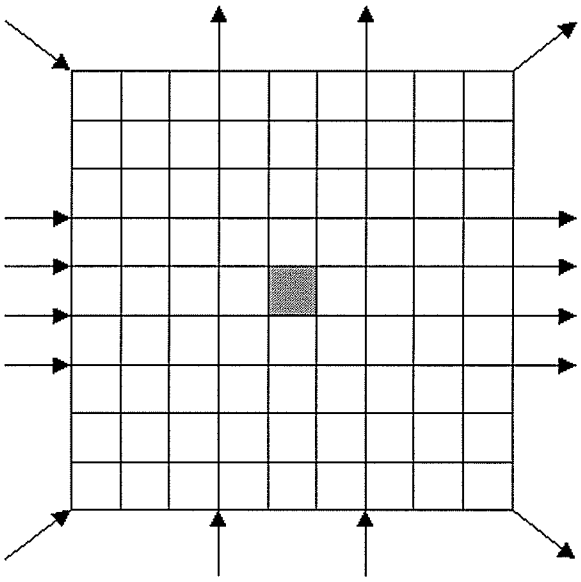

Figure 3.2: Simplified 2-D breast tumour imaging setup using the Wexler 2-D EIT imaging algorithm. Arrows show points of injection/extraction (i.e., excitations). There are 8 pairs of current excitations. Background region has conductivity of magnitude 1.0 and central element (i.e, the tumour element) has conductivity of 4.0.

Figures 3.3(a-d) show a sequence of images recovered for the 2-D case of Figure 3.2 using the original Wexler algorithm after 5, 50, and 500 iterations respectively. The gray-level images were generated using the software package Microcal™ Origin™ [5].

[5] Microcal™ Origin™, Version 5.0, Copyright © 1991-1997, Microcal Software, Inc.

(3.3a) --2-D Breast Tumour Imaging Simulated Problem

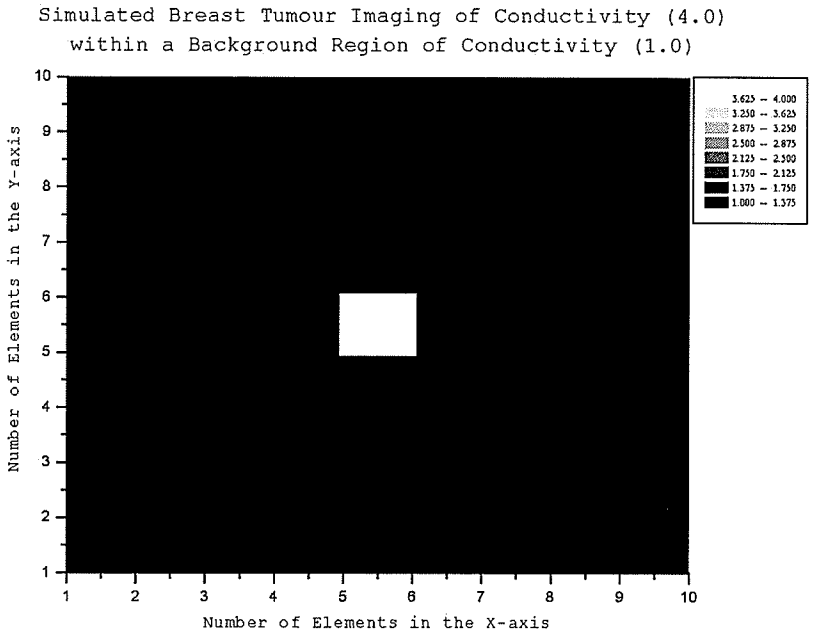

(3.3b) -- Recovered 2-D Conductivity Image at 5 Iterations

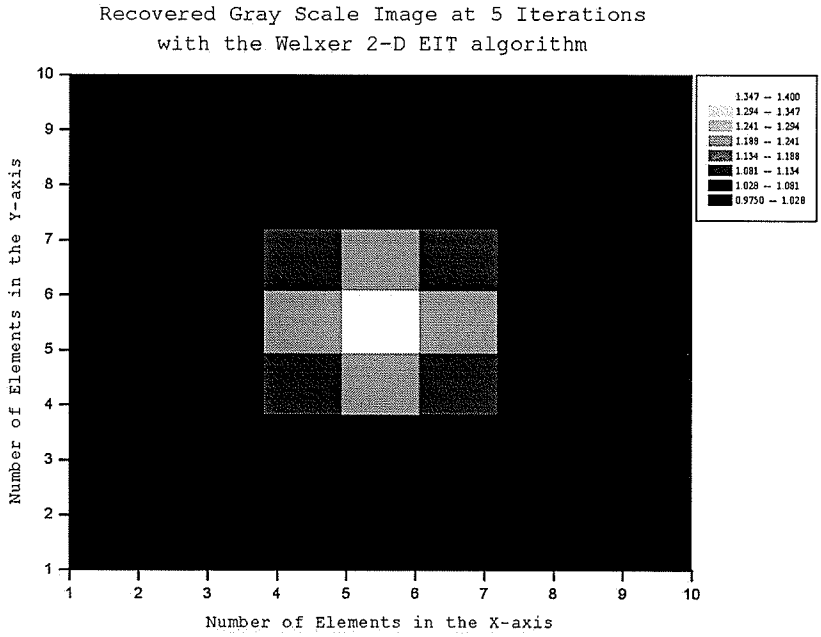

(3.3c) -- Recovered 2-D Conductivity Image at 50 Iterations

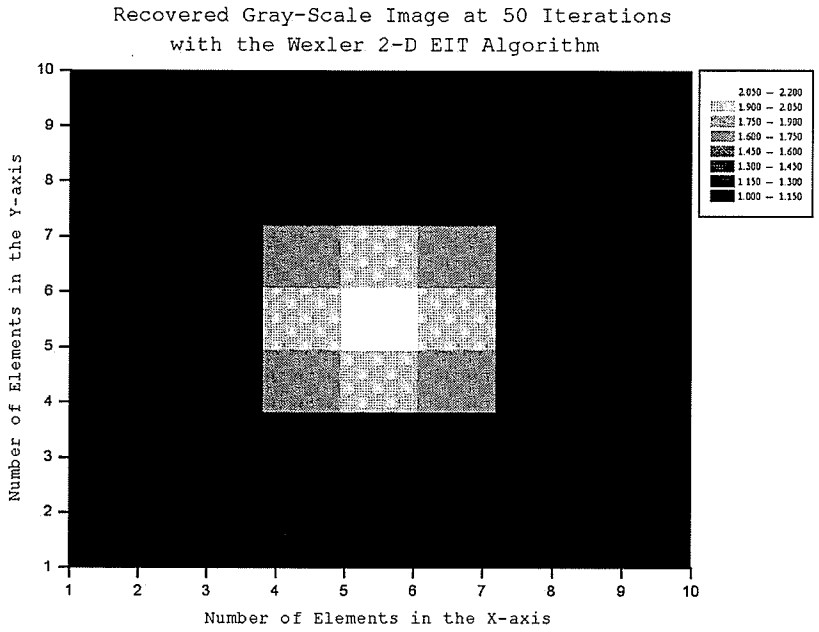

(3.3d) -- Recovered 2-D Conductivity Image at 500 Iterations

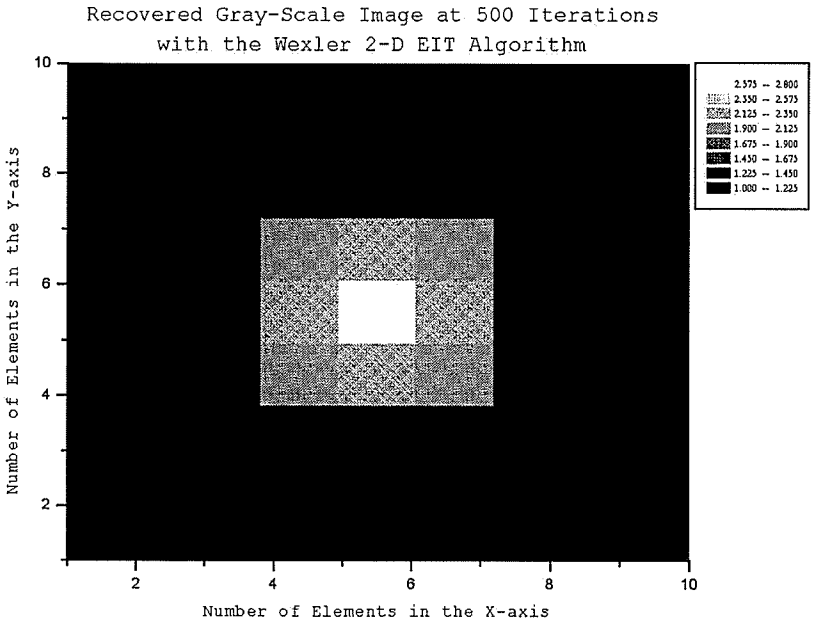

Figure 3.3 (a-d): Recovered conductivity images with the original Wexler 2-D EIT algorithm for setup of Figure 3.2. Image (a) shows the gray-level of the 2-D setup, (b), (c), and (d) show the recovered images at 5, 50, and 500 iterations respectively. Note that the conductivity of the tumour element increases with iterations and surrounding elements have higher conductivities than ideally expected. This phenomenon is termed the "Tumour-Edge" effect for obvious reason.

3.3 3-D Computer Simulations using the Original Wexler 3-D EIT Algorithm

In the simple 3-D computer simulations of breast imaging, the finite element mesh was created using standard linear elements with 8 nodes (see Appendix I). The 3-D computer model of the breast adopted is a cube of 9×9×9 = 729 elements with a central element representing a tumour of conductivity 4.0 within the homogeneous region of conductivity 1.0 (see Figure 3.4). Twenty current injections/extractions pairs are employed over the five sides of the cubic region, corresponding to a determinacy of approximately 0.8. Measurements are not performed on one side of the cubic region, which corresponds to the side at which the breast is attached to the chest wall. Figures 3.5(a-d) show a sequence of images recovered for each layer of the 3-D simulation of Figure 3.4 using the original Wexler algorithm after 5, 50, and 500 iterations respectively.

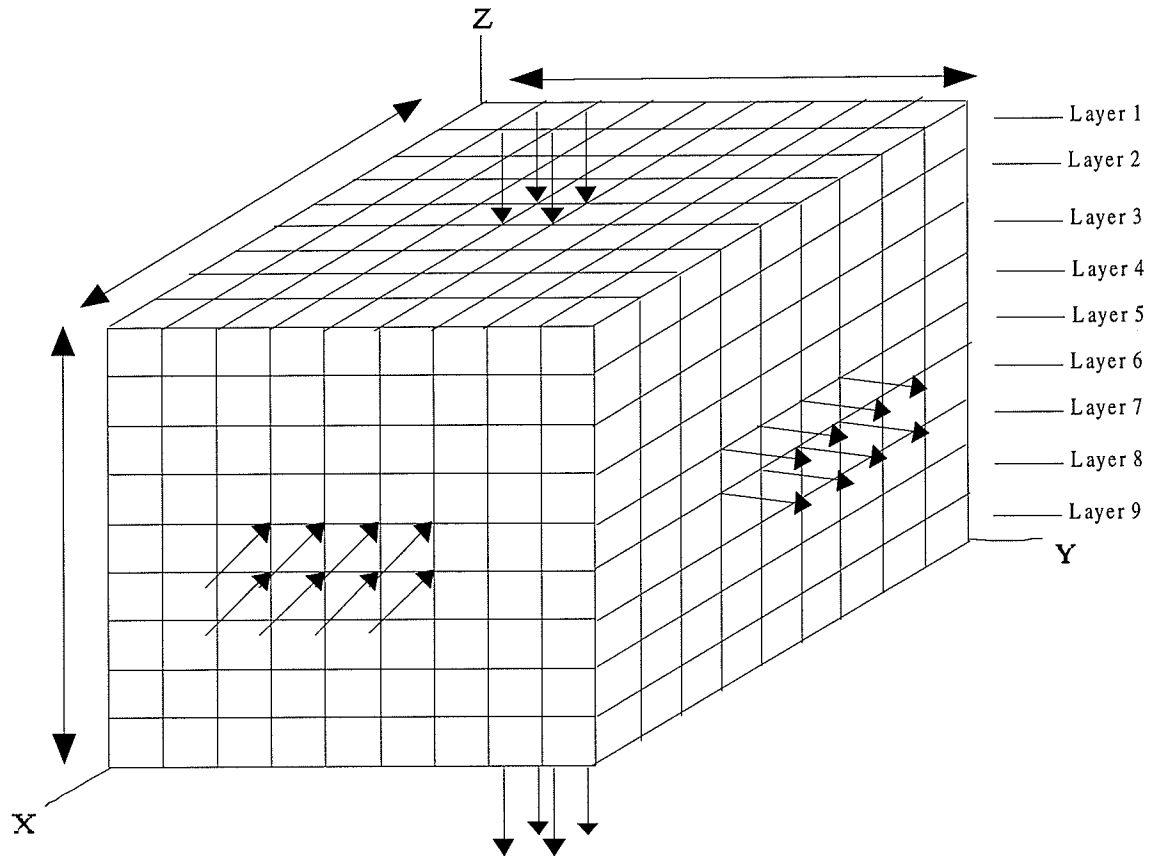

Figure 3.4: Simplified 3-D breast tumour imaging setup using the Wexler 3-D EIT imaging algorithm. Arrows show points of injection/extraction (i.e., excitations). There are no injection/extraction on the side of the chest wall. There are 20 pairs of current excitations, 9 layers, and a total of 729 elements. Tumour element is located at (x=5, y-5, and z=5) coordinates.

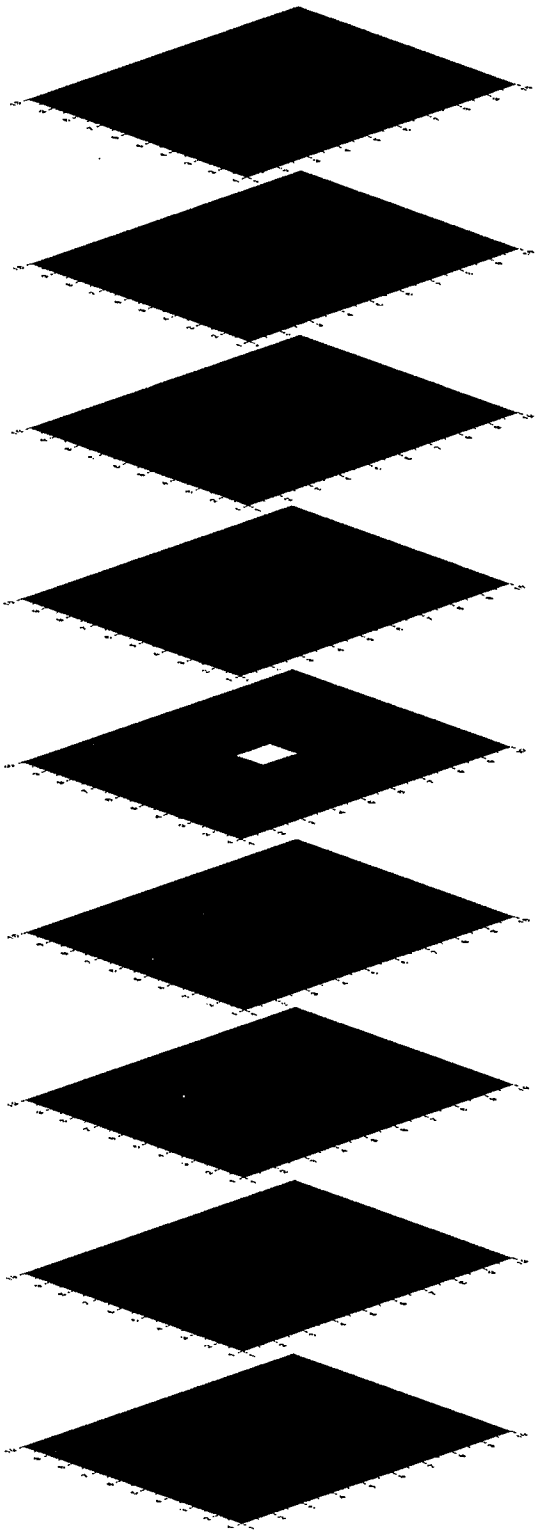

(3.5a) -- 3-D Simulated Problem

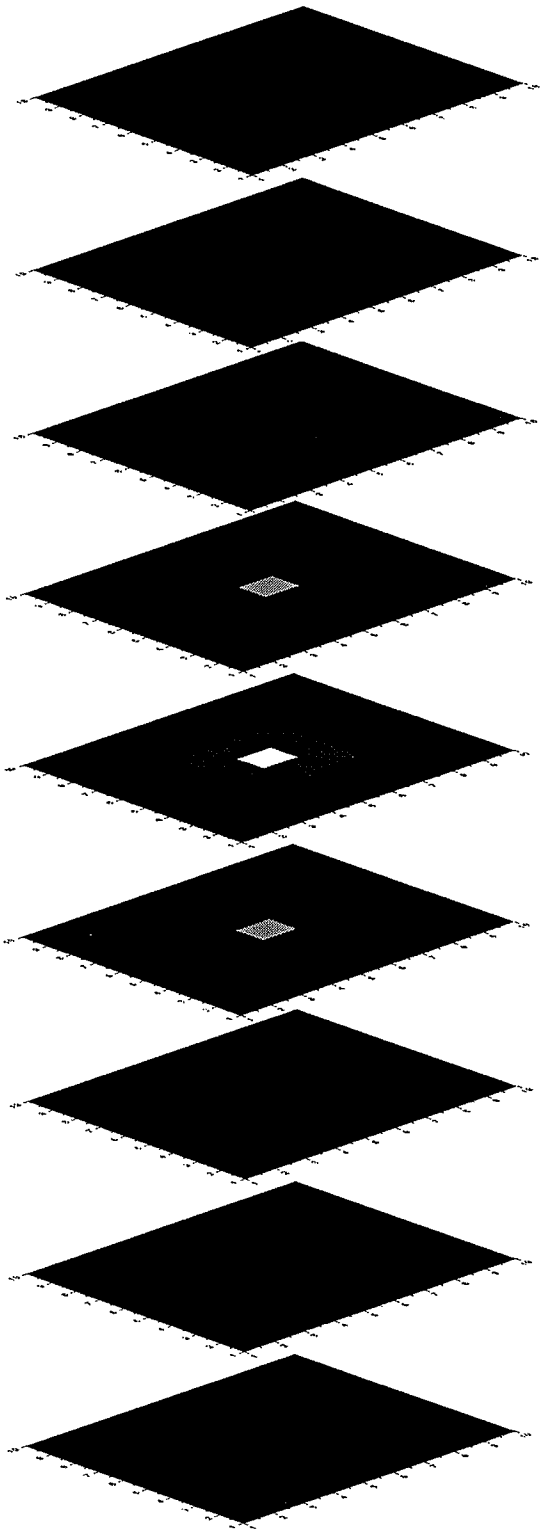

(3.5b) -- Recovered 3-D at 5 Iterations

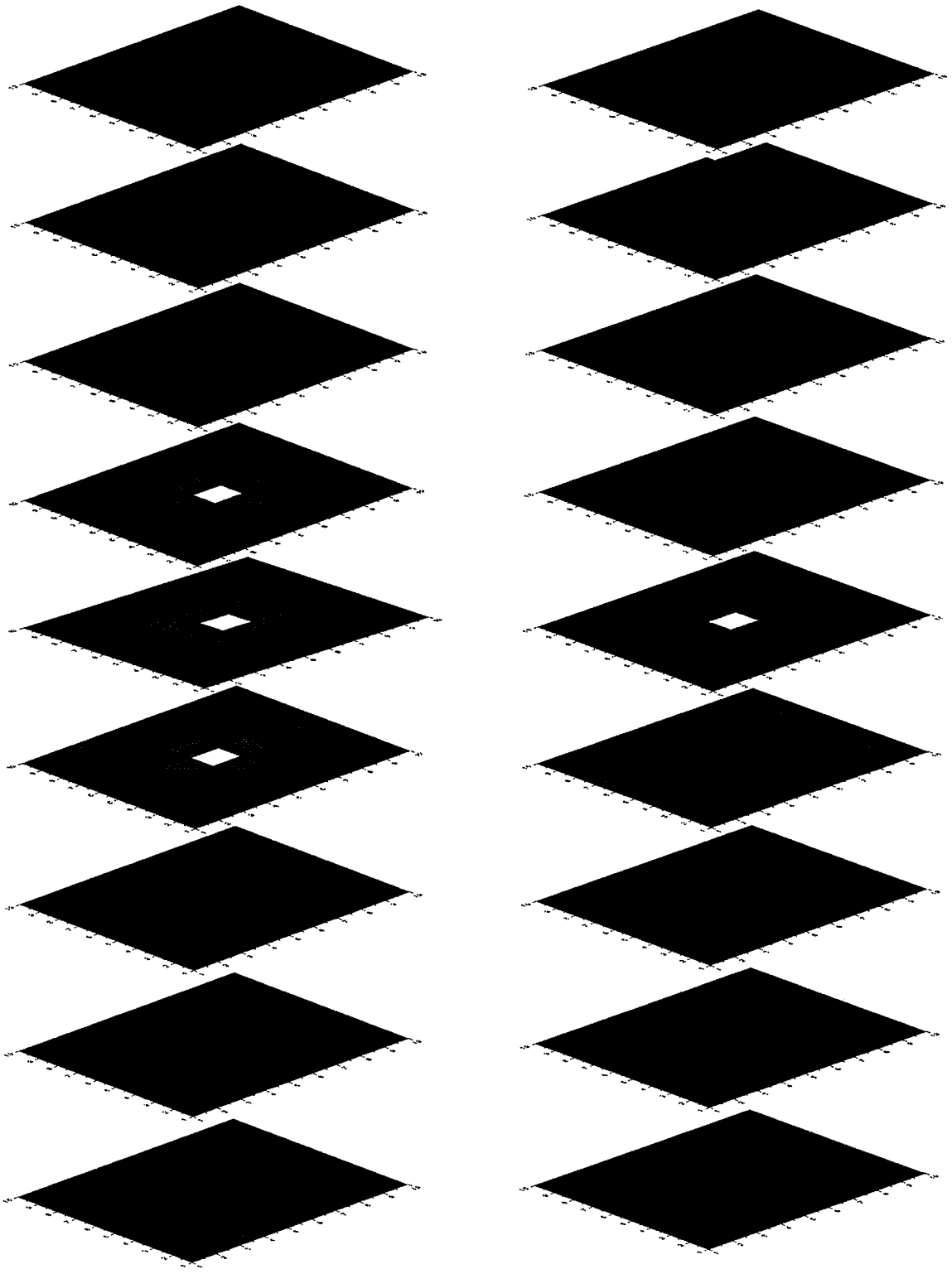

(3.5c) -- Recovered 3-D at 50 Iterations

(3.5d) -- Recovered 3-D at 500 Iterations

Figure 3.3 (a-d): Recovered conductivity images with the original Wexler 3-D EIT algorithm for setup of Figure 3.4. Image (a) shows the gray-level of the 3-D setup, (b), (c), and (d) show the recovered images at 5, 50, and 500 iterations respectively.

3.4 Convergence Rate of the Original Wexler 2-D and 3-D EIT Algorithm

To demonstrate the convergence rate of the original Wexler EIT algorithm, the norm of the error term is plotted as a function of iteration. The norm of the error term is defined as:

$$Error = \left(\frac{\sum_i \left| \kappa_{exact} - \kappa_{calc.} \right|}{\sum_i \left| \kappa_{exact} \right|} \right) \div M \qquad [3.6]$$

where κ_{exact} is the exact conductivity distribution obtained by direct measurement, $\kappa_{calc.}$ is the calculated conductivity distribution, and M is the total number of elements. Figure 3.6 shows the error norm plot (i.e., the convergence rate) of the original Wexler EIT algorithm for the 2-D and 3-D simulations that were described earlier over 500 iterations.

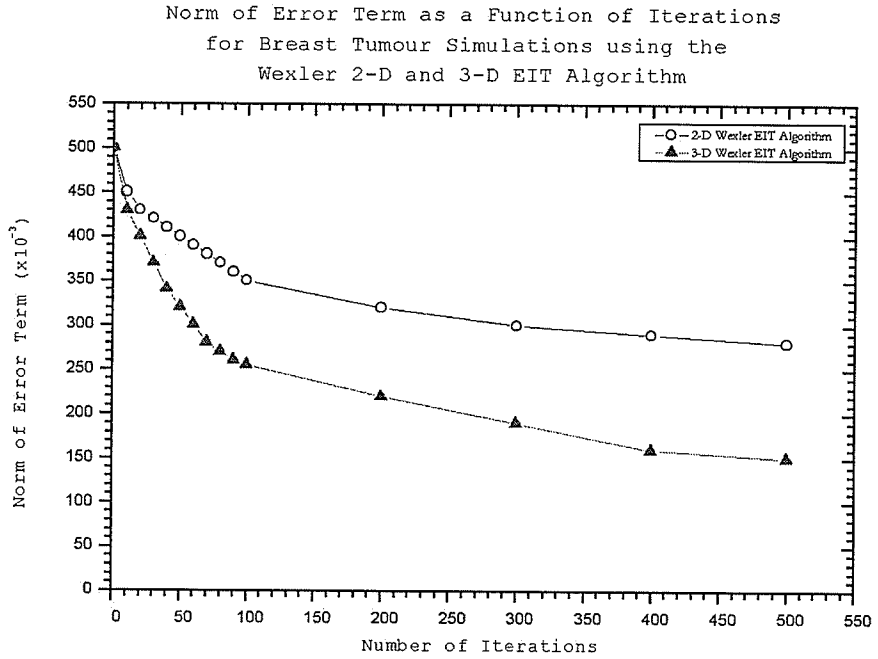

Figure 3.6: Norm of error term as a function of iterations for the 2-D and 3-D Wexler EIT algorithm for the simulations described above . Note that the 3-D algorithm converges much faster than the 2-D algorithm (to be discussed fully in Chapter 4).

3.5 Spatial Resolution of the Original Wexler 2-D and 3-D EIT Algorithm

To demonstrate the spatial resolution of the original Wexler EIT algorithm, the full- width at half-maximum (FWHM) of a single low-contrast object of unit area and volume is imaged at a central location within a 2-D and 3-D region of area 2500 element^2 (i.e., 50×50 elements) and 125,000 element^3 (i.e., 50×50×50 elements) respectively. Background region is set at a conductivity of 1.0 and the central unit area and volume element at conductivity of 4.0. Forty and two hundred and seventy excitation pairs were employed to recover the 2-D and 3-D images respectively which corresponds to a determinacy of approximately 0.94 and 0.88 respectively.

FWHM is a parameter commonly used to describe the width of a "bump" or an object in a picture, when the object does not have sharp edges. It is given by the distance between points on the 2-D profile at which the function reaches half its maximum value. Figure 3.7 shows an example of the FWHM for a Gaussian function.

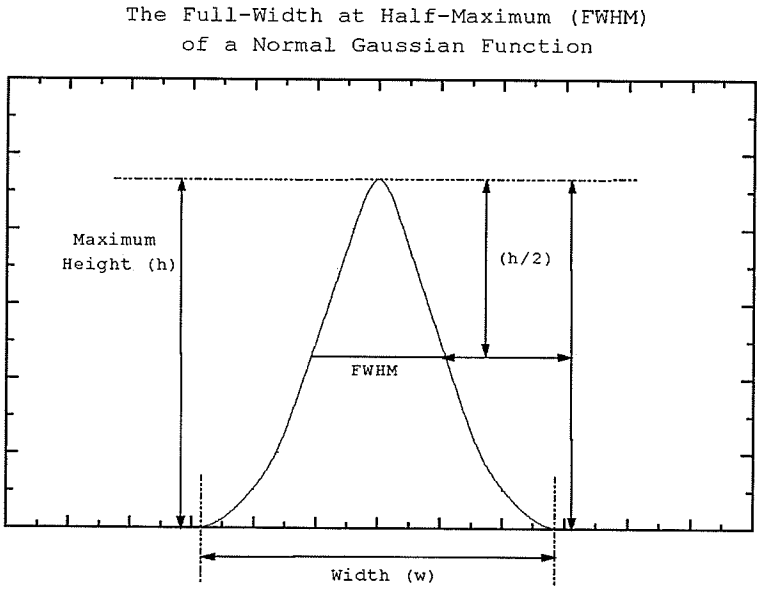

Figure 3.7: An example of FWHM (Full-Width at Half-Maximum) for a Gaussian function. The FWHM is a measure of spatial resolution of an image and is given by the distance between points on the picture at which the function reaches half its maximum value.

The unit area/volume central element employed in the 2-D and 3-D breast tumour imaging simulation approximates a Dirac delta function. The Dirac delta function is often used in imaging to analyze the performance of an imaging device. It is useful to measure the device's response to as simple an input as possible. Mathematically, the delta function in 1-D is defined in terms of the following properties:

$$\delta(x-x') = \begin{cases} 0 & \text{if } x \neq x' \\ \infty & \text{if } x = x' \end{cases} \qquad [3.7]$$

$$\int_{-\infty}^{+\infty} \delta(x - x')\,dx' = 1 \qquad \text{"Area under function is one"} \qquad [3.8]$$

The reconstructed image of a Dirac delta function is the point spread function (PSF) whose normalized cosine Fourier transform would correspond to the modulation transfer function (MTF) of the imaging system if the latter were linear and space invariant [Moru92],

$$\text{MTF}(v) = \frac{\int_{-\infty}^{+\infty} F(x)\cos 2\pi v x\,dx}{\int_{-\infty}^{+\infty} F(x)\,dx} \qquad [3.9]$$

where $F(x)$ is the symmetrical point spread function, v is the spatial frequency (i.e., the denominator used to normalize MTF(v) by the total surface under the PSF.

If it is assumed that the PSF is the Dirac pulse response at a region within the image, then the MTF is that region's frequency response. The PSF is a common tool for quantifying the spatial resolution of the imaging system. As mentioned previously, linearity and space invariance are prerequisites for the proper use of the PSF. Despite the fact that EIT is nonlinear and space variant, the PSF can provide a useful indication of the system behavior [Guar91 and Meth96]. Figure 3.9 below shows the recovered two-dimensional conductivity profiles of the 2-D and 3-D simulations

described above for a central Dirac impulse (see Figure 3.8), generated using the Student Version of Matlab®[6].

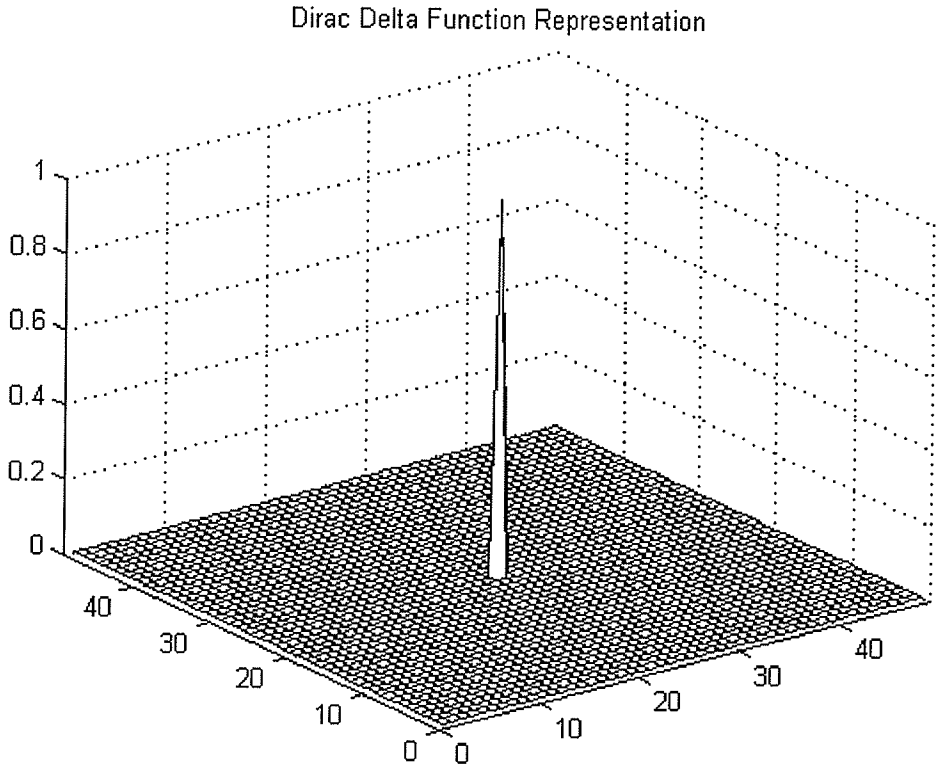

Figure 3.8: The Dirac Delta function representation. One element approximates a Dirac function of conductivity on the imaging plane. A similar representation of Dirac function was used by Guardo et al., 1991 [Guard91]. Though, not fully realistic, this representation provides a good indication of the system behaviour.

For the investigation of spatial resolution of the Wexler 2-D and 3-D EIT algorithms, conductivity profiles as a function of element position (elements) were recovered at 100 iterations. For the 3-D simulation, measurements of the FWHM were performed in both the cross-sectional and axial plane. The FWHM values obtained for the simulations are relatively close to those reported by Ider *et al.*, 1995 [Ider95] in the 2-D case and Metherall *et al.*, 1996 [Meth96] in the 3-D case as shown in Table 3.0 below.

[6] Matlab, The Language of Technical Computing, Version 5.00.4073, Copyright © 1984-1996, The MathWorks, Inc.

Table 3.0: FWHM results of the 2-D and 3-D simulations of Section 3.5. Results are compared to those of Ider *et al.*, 1995 and Metherall *et al.*, 1996. Note that results are quite similar.

	Ider *et al.*, 1995		Metherall *et al.*, 1996		Wexler *et al.*, 1985	
Object Position	**FWHM (%)**		**FWHM (%)**		**FWHM (%)**	
	2-D	**3-D**	**2-D**	**3-D**	**2-D**	**3-D**
Central	27	-	-	x-s: 10 axial: 12.5	24	x-s: 13 axial: 14.6

- data not available, x-s - cross-sectional plane, and axial - axial plane.

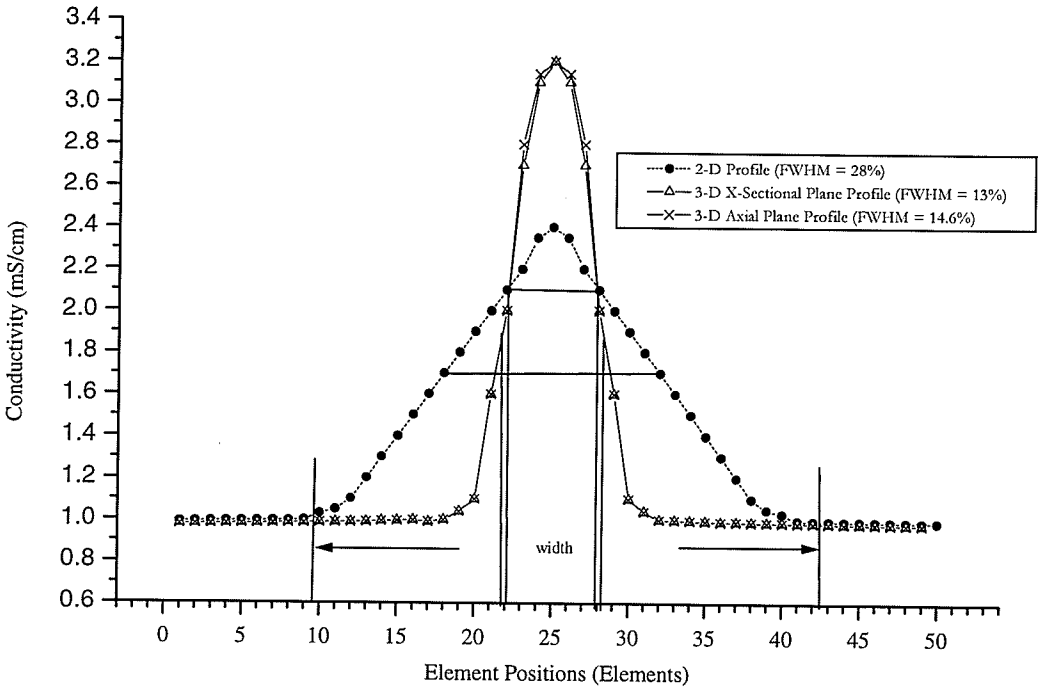

Figure 3.9: FWHMs for the 2-D and 3-D simulations of Section 3.5. The FWHM for the 2-D simulation is 24% of the diameter of the imaging region. The FWHM of the cross-sectional and axial plane of the 3-D simulation are 13% and 14.6% of the diameter of the imaging region respectively.

3.6 Discussion

The original algorithm of Wexler has many advantages over other methods, the most important being that it transfers the difference in potential between the Neumann and Dirichlet boundary conditions to the interior rather than to the boundary, unlike the procedure used in Newton-Raphson-like methods [Woo90]. This approach yields a sparse-matrix permitting use of efficient finite-element method solution schemes. Furthermore, currents are allowed to follow natural paths, and no attempt is made to force them to behave in beam-like fashion. Image quality is not degraded by contact and spreading resistance as is inherent in resistance projection techniques [Bate80].

For section 3.2 and 3.3, the magnitude of conductivity of the central tumour element for the 2-D simulation was determined to be 1.36, 2.21, and 2.64 at iterations 5, 50, and 500 respectively. In the 3-D case, the conductivity of the central element was 1.58, 2.42, and 2.85 at 5, 50, and 500 iterations respectively. Analysis of the recovered image appears to indicate that the recovered conductivity of the central element is affected by closely surrounding elements. It appears as though the difference in conductivity, between simulated and recovered, is distributed equivalently to surrounding elements. As a result, the magnitude of the recovered conductivity of the central element is consequently lower than average. This effect appears to be more pronounced in the 2-D case than in the 3-D simulation.

From the simulations described in Section 3.4, it was obvious that the original Wexler EIT algorithm is slowly convergent, though the 3-D is relatively faster than the 2-D algorithm. For the more realistic 3-D breast cancer imaging simulation described in Section 3.5, the algorithm converges in approximately 3hrs and 47 minutes at approximately 8,000 iterations on a SUNW, SPARCstation-4. The spatial resolution (i.e., FWHMs) of the 2-D simulation was observed to be much lower than that of the 3-D case. The original Wexler 3-D algorithm can only resolve up to 13% in the cross-sectional plane and 14.6% in the axial plane of the diameter of an imaging region.

3.7 Summary

The original Wexler EIT algorithm correctly solves the physics of the inverse nonlinear problem of EIT. It does so by solving Poisson's equation, which correctly describes the flow of electrical current in a heterogeneous medium. However, to be of any potential clinically (i.e., in the imaging of breast tumours at an early stage), the algorithm needs refinement. At first glance, it appears that both the convergence rate and the spatial resolution of the recovered image ought to be improved drastically. What other criteria/standards should the Wexler EIT algorithm fulfill/meet in order to be of potential in the screening/imaging of small breast tumour? This question is fully addressed in the next chapter.

Chapter 4

Characteristics of the Original Wexler 2-D and 3-D EIT Algorithm

4.1 Introduction

In Chapter 3, the original Wexler EIT algorithm was identified as being slowly convergent and the spatial resolution of the recovered image as being relatively low compared to other clinical imaging modalities. To be of potential in the clinical imaging of breast cancer, the Wexler EIT algorithm needs to be improved. Improving the convergence rate and the spatial resolution, however, do not necessarily guarantee clinical success, since many other factors such as the algorithm's ability to handle noise and patient motion among others, need to be considered in order to meet expected clinical imaging standards. As such, the characteristics of the Wexler EIT algorithm is thoroughly investigated here, through a series of computer simulated tests and effects, in an attempt to determine whether it meets the expected clinical imaging requirements.

The choice of an initial conductivity distribution dictates the time it takes an iterative EIT algorithm to converge, i.e., when the difference between the calculated conductivity distribution is equivalent to the actual measured conductivity distribution. Does the Wexler EIT algorithm converge sooner if the assumed initial conductivity distribution is relatively close or equivalent to the correct one? What about the effect of different excitation schemes and the number of finite elements on convergence rate, and consequently, on recovered image quality? How does the Wexler EIT algorithm perform at sharp conductivity edges (i.e., at diseased-to-normal tissue interface)? What about noise handling? Can the algorithm handle noise that

exists in a real clinical situation? These and many more issues are considered here by performing 2-D and 3-D computer simulation models of simplified breast cancer imaging using the Wexler EIT algorithms. Results of these simulations are discussed and presented.

4.2 Initial (or Starting) Conductivity Distribution Effect

In general, a highly accurate initial guess of conductivity distribution ought to lead to faster convergence speed [Mura85 and Avis92]. If the initial starting conductivity distribution is equivalent to the exact conductivity distribution, similar to a null test in image processing, the Wexler EIT algorithm converges at the first iteration. This observation supports the accuracy of the computer code. Using the previous 2-D and 3-D simulation setups of Chapter 3 (see Sections 3.2 and 3.3), hereafter referred to as the standard 2-D and 3-D examples, the effect of initial (or assumed) conductivity distribution is investigated.

In the 2-D and 3-D simulations of Figures 3.2 and 3.4 respectively, the central element/voxel (i.e., the tumour) had a conductivity of 4.0 within a background region of conductivity 1.0. The imaging region (i.e., tumour and surrounding) was then recovered by making an initial homogeneous (i.e., conductivity equal to 1.0) guess at the conductivity distribution. If the initial guess at the conductivity distribution is 2.0, 3.0, 4.0, or 5.0, the time to converge is accelerated. Figures 4.0 (a-b) show the norm of the error term as a function of iteration, at conductivity distribution guesses of 1.0, 2.0, 3.0, 4.0, and 5.0 for the 2-D and 3-D cases respectively.

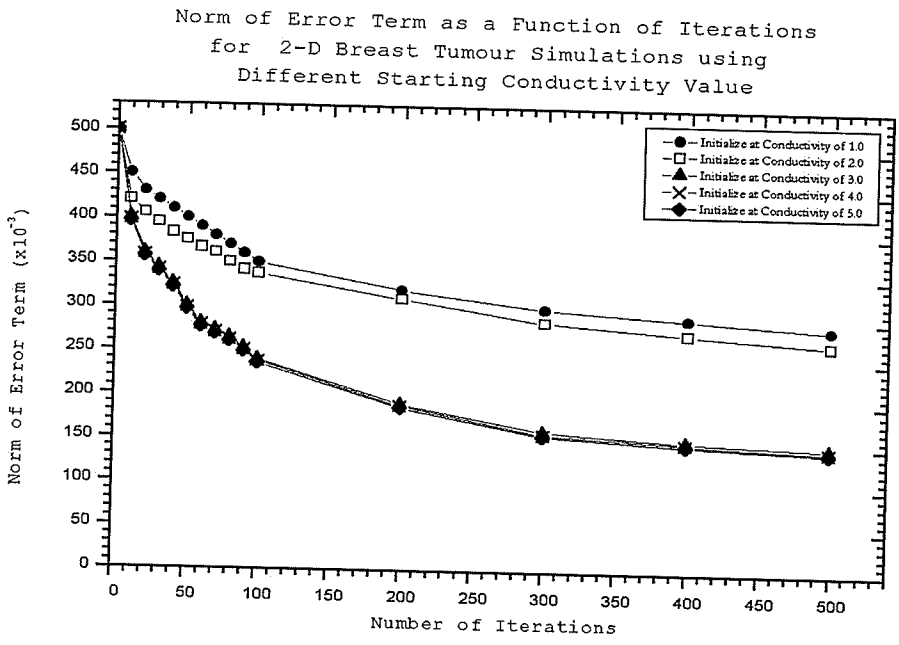

(a)

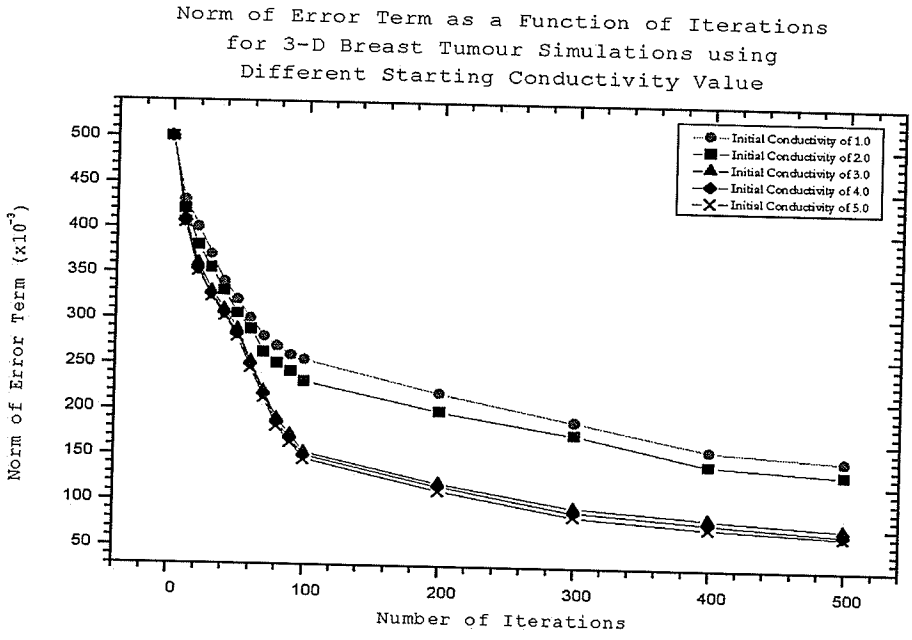

(b)

Figure 4.0(a,b): Norm of error term as a function of iteration for 2-D and 3-D setup of Figure 3.2 and 3.4 respectively. Initial conductivity guess of 1.0, 2.0, 3.0, and 4.0, and 5.0 are shown. Note the increase in convergence speed when initial conductivity distribution guess is close to exact conductivity distribution.

From the results obtained above, it is obvious that a good starting value will produce correct results, while a poor initial guess may lead to slow convergence [Mura85]. As mentioned earlier, if the assumed conductivity distribution is equal to the exact distribution, the Wexler EIT algorithm converges in the first iteration. Similarly, an accurate initial guess would lead to an improved recovered image quality. It can also be observed that, at similar conditions, the Wexler 3-D EIT algorithm converges much faster than the 2-D algorithm. This is associated with the fact that current is not restricted to the 2-D plane

4.3 Excitation Configuration and Measurement Pattern Effect

An *excitation* pattern is usually defined as a set of current injections and extractions employed to recover an image. A *measurement* pattern is a set of measured potentials induced by an excitation pattern [Mu94]. In iterative approaches to solving the nonlinear inverse 'static' EIT imaging problem, the choice of excitation and measurement pattern is crucial to the success of an algorithm [Mura85]. In particular, it is important that the most reasonable number and location of electrodes is chosen since the incorrect choice will affect the speed of the algorithm and concurrently the quality of the recovered image [Hua91].

In the literature, one finds numerous studies on optimal electrode configuration and measurement pattern distribution. A few are mentioned here. Seager and Bates have given, in a comprehensive and detailed proof, the optimum electrode-pair position for two eccentric disks [Seag84 and Seag85]. Newell, Gisser, and Isaacson in a series of papers proved that for two concentric disks, the best current distribution to be introduced (with the electrodes) is the spatially sinusoidal one [Isaa86, Giss87, and Newe88]. Lidgey *et al.*, 1992 employed programmable voltage sources to obtain an optimal current pattern [Lidg92]. Hua *et al.*, 1993 used compound electrodes (i.e., a larger outer electrode to inject current and a smaller inner electrode to sense voltage) to demonstrate improvement in recovered image quality [Hua93]. Blad *et al.*, 1994

using a method that implements a voltage source in order to measure current accurately, rather than using a constant current generator, showed that improvement in the stability of the hardware leads to greater image quality [Blad94]. Recently, Schuessler and Bates, 1998 in a study on determining the optimal number and type of electrodes for thoracic 'static' EIT imaging, argued that compound electrodes, that permit voltage measurement at the site of current injection did not yield any practical improvement of the image quality [Schu98]. They showed that by doubling the number of boundary electrodes a reduction in the reconstruction error by almost two orders of magnitude could be obtained.

It is known and generally accepted that the number and location of electrodes employed in an excitation pattern depends on the algorithm, the problem at hand, and somewhat on experience [Mur85]. To some extent, this is a correct statement. However, the fact that numerical schemes are used to solve the field problem, allows the introduction of truncation (or discretization) error that is incidental to image recovery. With that in mind, and considering the similarity between finite element discretization and lumped element networks, Mu derived some practical observations for optimal excitation and measurement pattern of the 2-D and 3-D Wexler algorithm [Mu94]. Among the observations, of particular interest to breast imaging, are:

- The error function minimization algorithm, namely the Wexler EIT algorithm, can address both over- and under-determined problem.

- Network formulation allows selection of the minimal number of nodes, in a topological sense, without increasing determinacy. Subsequently, optimal measurement locations can be derived. This observation is of particular interest for the imaging of breast cancer.

- Sensitivity analysis and graph theory implementation revealed that the reliable region produced by the arrangements of excitation patterns is crucial in speeding up the algorithm and subsequently in improving image quality. As demonstrated by sensitivity analysis, not all the excitation patterns are necessarily needed for

optimal recovery time and image quality. Rather, what is needed is an optimal arrangement that can provide a reliable region.

- To eliminate contact and spreading resistance for tetrapolar excitations, a measurement scheme, i.e., the *sometimes* pattern, that discards potential measurements at active electrodes produced more reliable image and reduced the number of independent measurements.

- Changing electrode shape does not improve image quality significantly.

A more comprehensive discussion on optimal excitation and measurement patterns can be found in [Mu94]. For the purpose of this discussion, Mu's observations were implemented on the standard 2-D and 3-D examples of simple breast cancer imaging computer simulations model. Mu's observations were verified using the standard examples of Figures 3.2 and 3.4.

From the results of simulations it was observed that the Wexler algorithm addressed problems that are slightly under-determined and performs well at determinacy higher than 1.0. The *sometimes* measurement pattern recovered impedance images faster and with more accuracy than the *always* pattern, which uses all measured boundary potentials including those at active electrode sites. Excitation patterns that employed a symmetrical or near-symmetrical configuration provides faster convergence and improved image quality. The combination of minimal node involvement, symmetrical or near-symmetrical excitation patterns, and *sometimes* measurement patterns provide the optimal configuration for the imaging of breast tumour. Similar optimal excitation and measurement configuration was shown, via simulations using the Wexler EIT algorithm, by Mu for nonuniform geometry [Mu94].

4.4 Finite Element Mesh Scheme and Size Effect

As defined earlier, the forward problem involves finding the internal current and voltage distributions from the known conductivity distribution and boundary current/voltage distributions. There is no analytic solution to the forward problem for an irregular and inhomogeneous medium. Thus finite element method or finite difference method is usually used to obtain the numerical solution [Moru96]. The generation of a finite element mesh usually depends on the conductivity distribution and geometric shape of an object (i.e., situation-dependent). For a forward solution, more elements will generally result in higher accuracy but at the expense of higher computational time and complexity [Moru96].

Ideally, the smallest object that an algorithm can recover accurately would in principle be equal to or greater than the average size of the finite element mesh. In the case of early stage 3-D breast tumour imaging, the finite volume element (or voxel) size ought to be approximately ($1\times1\times1 = 1$ mm^3) in volume, if a tumour of volume 1mm^3 is to be recovered. However, considering the average female breast size, one will be faced with a rather much complicated 3-D dense mesh, and consequently a formidable computing task. As such, many mesh formulation schemes have been developed to address the compromise between accuracy and computational complexity in solving the nonlinear problem of EIT [York88 and Berr92].

Mu, 1994 described a procedure that starts with a coarse mesh to obtain an initial guess and a fine mesh to recover the image accurately in the inverse problem. Mu argued and demonstrated that the convergence period would be greatly reduced if a coarse mesh were used first to obtain an approximate solution, then a finer mesh to reach the true image. The implementation of this scheme is fully described in Mu, 1994 [Mu94].

Here the observations derived by Mu [Mu94] were implemented on the standard 2-D and 3-D computer simulation examples for breast cancer imaging (Figure 4.1). The purpose is to determine whether the scheme developed by Mu can be incorporated into the Wexler algorithm in order to provide an improved algorithm that will speed up the original convergence speed and recover an image of appropriate quality for breast imaging.

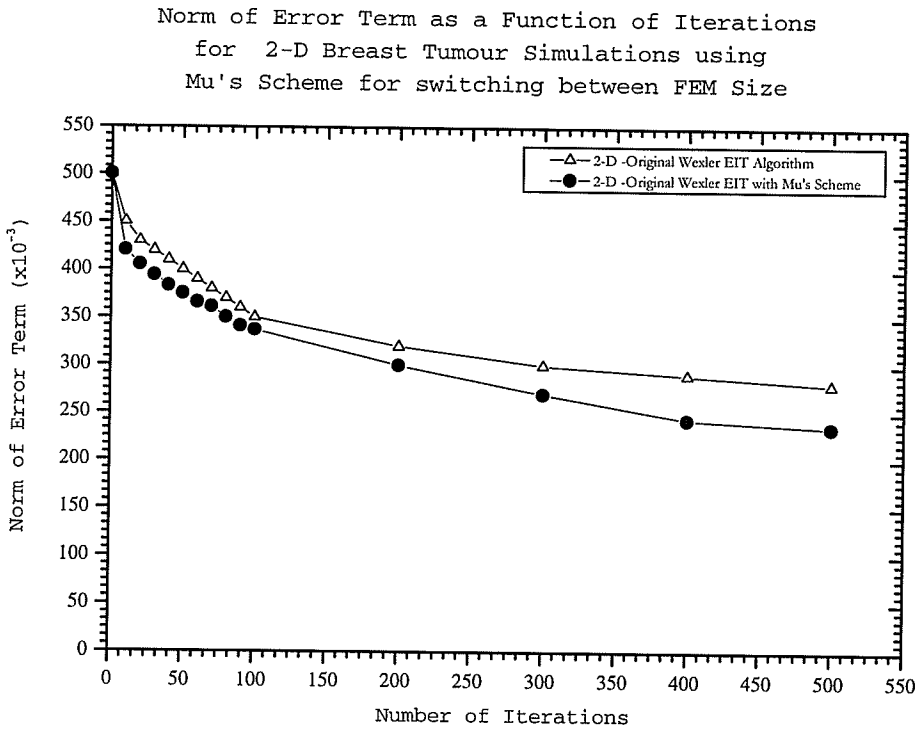

Figure 4.1: Norm of error tern as a function of iterations for the 2-D original Wexler EIT algorithm with and without Mu's scheme for improving convergence speed. Note that the 2-D algorithm converges much faster with Mu's scheme than the original Wexler algorithm. Similar results were obtained for the 3-D simulation.

It is obvious that Mu's scheme results in faster convergence. In this simulation, a coarse mesh of size 5×5 was used in the first 20 iterations and a fine mesh of 9×9 was used to recover the true image for the same geometry.

4.5 Convergence Behaviour Test on Spatial Location of Tumour

Does the Wexler EIT algorithm converge faster if the region(s) of interest has/have different spatial locations? Murai and Kagawa 1985, using 2-D computer simulations, observed that conductivity change nearer to the surface was easier to detect than conductivity change in the internal region [Mura85]. They attributed this observation to an "inherent difficulty" with the inverse problem. Kotre 1996 [Kotr96] developed a measurement strategy, for subsurface electrical impedance imaging, from observations of an object spatial location convergence behaviour. There are no other reported studies of the relationship between convergence speed and spatial location of anomaly/ies. As such, in this section a comprehensive investigation of the time the Wexler algorithm takes to convergence as a function of spatial location of the tumour is performed.

To test convergence behavior on the spatial location of a tumour, 2-D and 3-D computer simulations were performed. In the 2-D simulation, a tumour of unit area 1 element^2 is imaged at peripheral, intermediate, and central locations within an imaging region of area (81 element^2, i.e., 9×9 elements). The tumour element (or pixel) has a conductivity value of 4.0 within a background region of conductivity 1.0. The minimum number of excitations pairs is used, i.e., eight excitation (i.e., injection and extraction) pairs are used to recover the tumour using the *sometimes* pattern. This scenario gives rise to a determinacy of 1.04. The spatial locations of the peripheral, intermediate and central tumour element are at (x=1, y=5; x=3, y=5; and x=5, y=5) respectively. For the 3-D simulation, a tumour of unit volume 1 element^3 is imaged at the peripheral, intermediate, and central location within an imaging region of volume (729 element^3, i.e., 9×9×9 elements). The tumour element (or voxel) has a conductivity value of 4.0 within a background region of conductivity 1.0. The minimum number of excitations (i.e., twenty) is used to recover the tumour using the *sometimes* pattern. This corresponds to an under-determined problem (determinacy is approx. 0.8). The spatial locations of the peripheral, intermediate, and central tumour

voxel are at (x= 1, y=5, z=5; x=5, y= 3, z=5; and x=5, y=5, z=5) respectively. With reference to Figure 3.4, each voxel lies on the same layer, i.e., layer 5 but are at different spatial coordinates as described above.

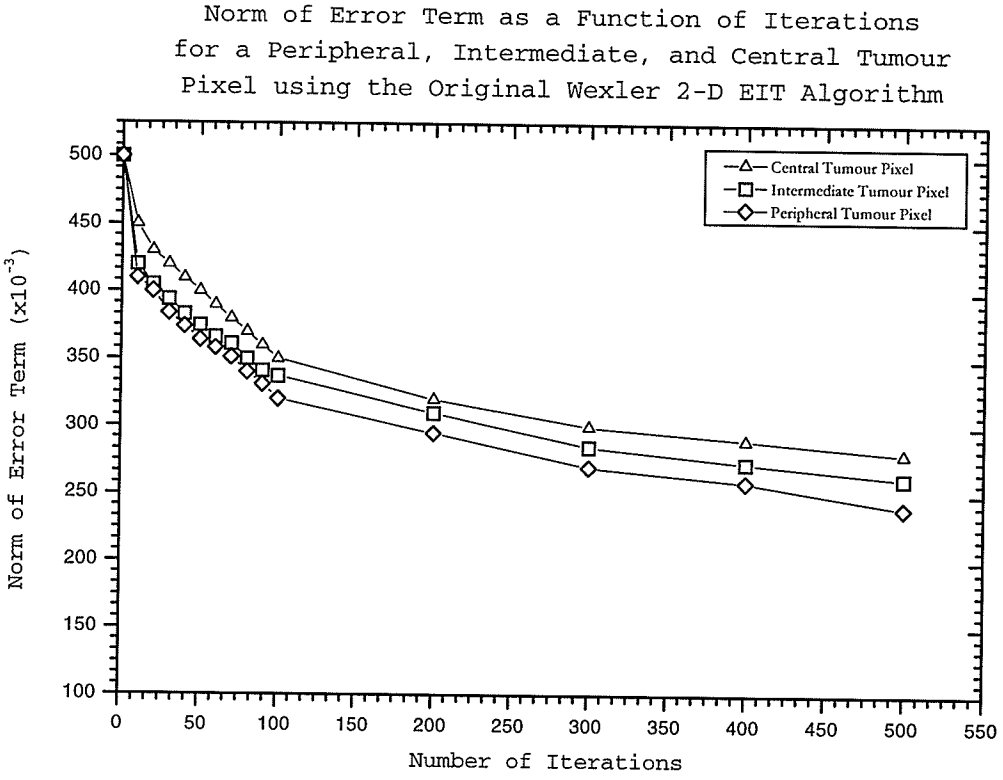

Figure 4.2: Norm of error term as a function of iteration for the peripheral, intermediate, and central pixel element using the original Wexler 2-D EIT algorithm. Note that the peripheral pixel has the highest convergence rate when compared to the intermediate or central tumour pixel. Similar observations were made for the 3-D original Wexler EIT algorithm.

Figure 4.2 above shows the convergence rate of the Wexler 2-D EIT for the peripheral, intermediate, and central tumour pixel respectively. Similar behaviour was observed for the 3-D algorithm. It is obvious from Figure 4.2 above that if the tumour is located at the periphery, the Wexler algorithm converges much faster than if the tumour is located at the intermediate or central location. The central tumour element takes relatively the longest time to converge.

The convergence characteristic and 'dynamic' of the Wexler algorithm was investigated further. This time, rather than plotting the norm of the error term, the recovered conductivity value of a background pixel on the edge of a central tumour, a background pixel located on the periphery, and a central tumour pixel were imaged. The central tumour pixel has a conductivity value of 2.8. The edge and peripheral pixels have conductivity values of 1.0. The purpose of this investigation was to determine how the conductivity value of the pixel of interest, described previously, behaves with increased iteration counts. Figure 4.3 below shows the recovered conductivity value for the background peripheral and edge pixel, and a central tumour pixel as a function of iteration counts for the 2-D simulation setup.

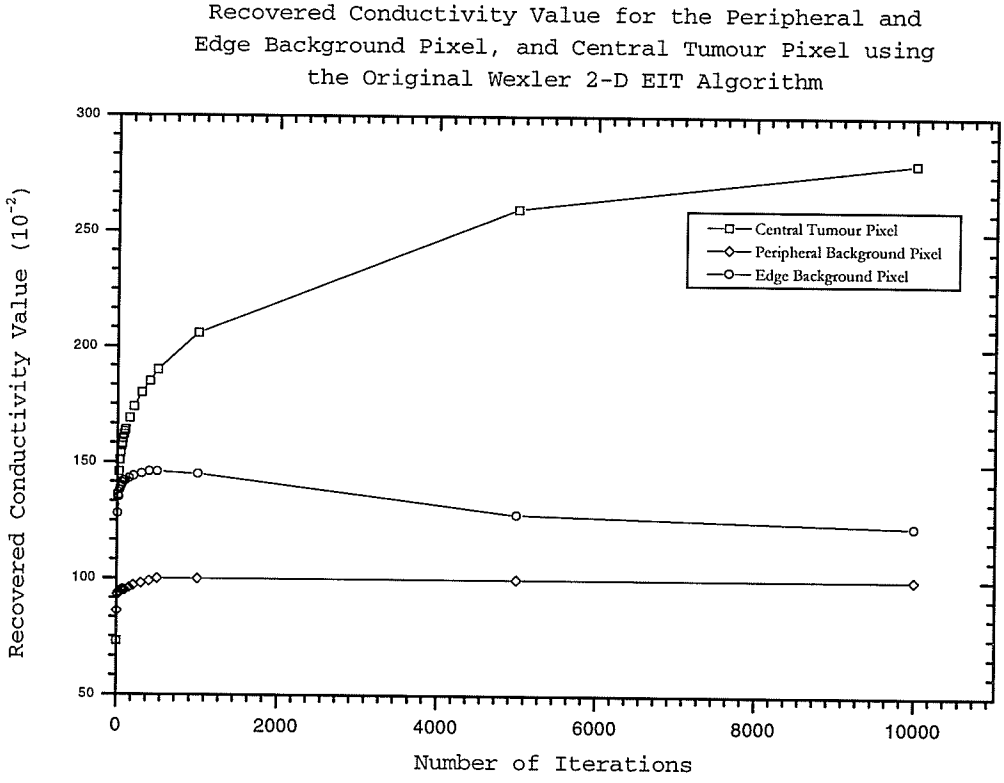

Figure 4.3: Recovered conductivity value as a function of iteration for the background peripheral and edge pixels, and central tumour pixel element using the original Wexler 2-D EIT algorithm. Note that the peripheral pixel lies within a conductivity of average value 1.0. Similar observations were made for the 3-D original Wexler EIT algorithm. The conductivity of the background edge pixel first increases with iterations, but then later drops to its normal value of 1.0.

The simulation results obtained in Figure 4.3 appeared to indicate that the background pixel kept at an average conductivity value of 1.0 throughout the iteration counts. The background edge pixel conductivity increases with iteration count at early iteration and later drops to the correct value. Similar observations were made for the 3-D algorithm. What is also obvious is that if the history of conductivity distributions is known from earlier iterations, future distributions can be determined by extrapolation. The last observation is further investigated in the next paragraph.

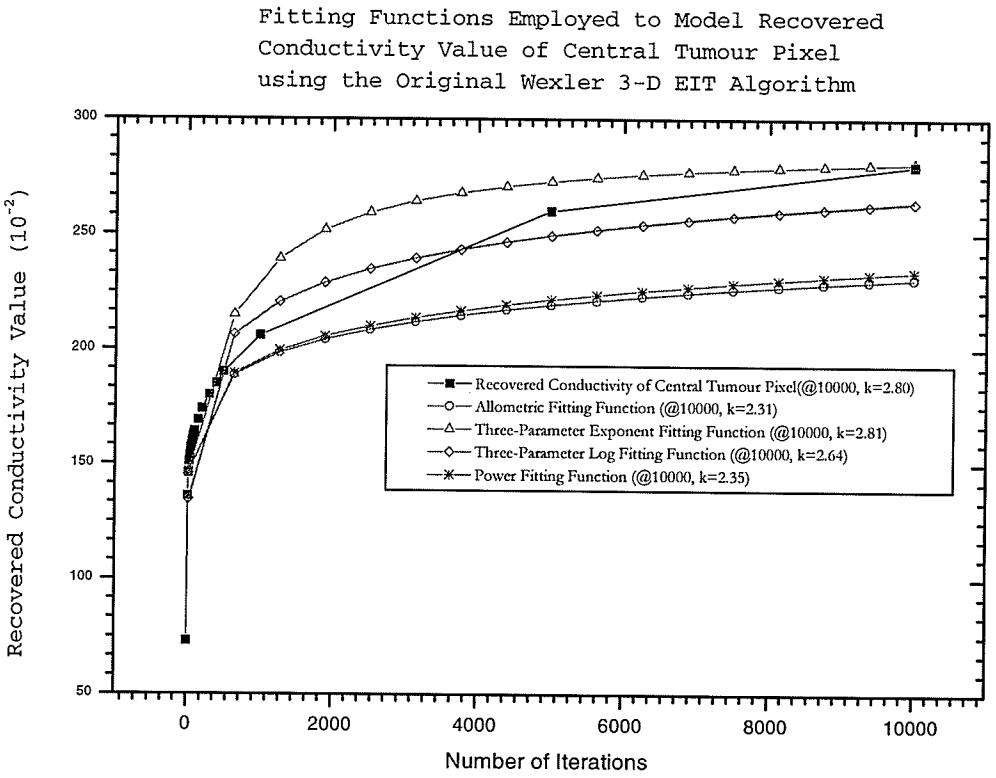

Figure 4.4: Fit functions employed to model the conductivity behaviour of the central tumour pixel as a function of iterations. Note that the best-fit functions are the three-parameter exponential and the three-parameter log respectively. Similar observations were made for the 3-D original Wexler EIT algorithm.

The behaviour of the conductivity value observed above for the central tumour pixel is modelled. The purpose is to determine the correct "fit function" that will fit the observed conductivity progression as a function of iteration. Since the focus is on the central tumour pixel, no fitting functions were derived for the background peripheral and edge pixels. Besides, the conductivity value for the background peripheral and edge pixel ought to be ideally at a constant (approximately an average value 1.0).

Figure 4.4 above shows the "fit functions" of the recovered conductivity distribution for the 2-D simulation described above. In this simulation, the central tumour pixel is at a conductivity value of 2.8 and the background region is at a conductivity value of 1.0. It can be observed that the best fit functions are the three-parameter exponential and logarithmic functions respectively. Fitting was performed using the software package Origin Microcal™. The functions are mathematically expressed as:

$$y = a - b\ln(x+c) \qquad [4.0]$$

$$y = ae^{\frac{b}{x+c}} \qquad [4.1]$$

where a, b, and c are fitting parameters, y is the conductivity value at iteration x.

4.6 Spatial Resolution Dependency as a Function of Location of Tumour

In order to investigate the spatial resolution dependency as a function of location of tumour for the original Wexler EIT algorithm, a single low-contrast object of unit area and volume 1 element^2 and 1 element^3 is imaged at a central, intermediate, and peripheral spatial location. The area and volume of the imaging region are 50×50 elements (i.e., 2500 element^2) and 50×50×50 elements (i.e., 125,000 element^3) respectively. As discussed in Chapter 3, the unit area/volume element approximates a Dirac function. The FWHM (a measure of spatial resolution) of the recovered Dirac impulse was used to determine the spatial resolution of the simulated tumour. Table 4.0 below shows the recovered FWHMs of the central, intermediate, and peripheral simulated tumour of conductivity value 4.0 within a background region of conductivity value 1.0.

Table 4.0: FWHM results of the 2-D and 3-D simulations of Section 4.6. Results are compared to those of Ider *et al.*, 1995 and Metherall *et al.*, 1996. Note that results are quite similar.

	Ider *et al.*, 1995		**Metherall *et al.*, 1996**		**Wexler *et al.*, 1985**	
Object Position	**FWHM (%)**		**FWHM (%)**		**FWHM (%)**	
	2-D	**3-D**	**2-D**	**3-D**	**2-D**	**3-D**
Periphery	14	-	-	-	13	9
Intermediate	18	-	-	-	17	11
Central	27	-	-	x-s: 10 axial: 12.5	24	x-s: 13 axial: 14.6

- data not available, x-s - cross-sectional plane, and axial - axial plane.

It is obvious that the resolution at peripheral location is superior to that at intermediate and central. When compared to values obtained from the literature, the spatial resolution of the original Wexler 2-D and 3-D EIT were found to be quite similar to those obtained by [Ider95 and Meth96]. It is apparent that if the loss in resolution as a function of tumour spatial location could be compensated for, EIT spatial resolution would improve.

4.7 The "Tumour-Edge" Effect

From previous simulations it was observed that the Wexler EIT algorithm fails to give an acceptable image with sharp edges in a reasonable time. This effect is quite obvious in Figure 4.3 above, and in the recovered images of Chapter 3, Section 3.3. The conductivity of the background element that is located on the edge of the central tumour increases as a function of iteration. This affects the recovered conductivity value of the central tumour. This phenomenon is termed the "Tumour-Edge" effect and is observed at diseased-to-normal tissue interface as seen above.

If the original 2-D Wexler algorithm is used to image a conductivity function of the form $\kappa = 1 + \sin^2 x \cdot \sin^2 y$ located within a host medium with $\kappa = 1$ (where $0 \leq x$, $y \leq \pi$ span the picture) the algorithm converges in only a few iterations with high image quality. This represents a smoothly varying conductivity distribution over a 2-D case. However, if the conductivity distribution has the form of a square pulse, as had been simulated so far and shown below (Figure 4.5a-b), the algorithm takes much longer to converge and the resolution the at diseased-to-normal tissue interface is quite poor.

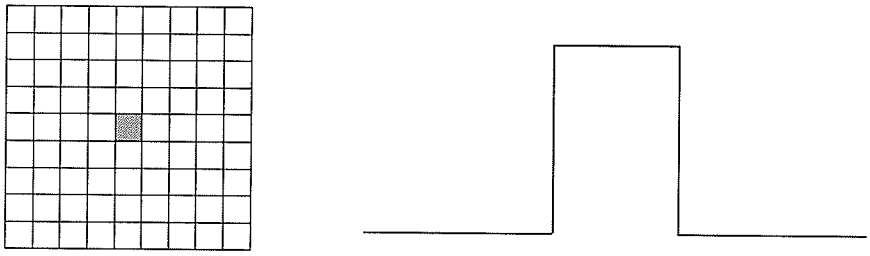

Figure 4.5(a,b): (a) shows a 2-D region with background region of conductivity 1.0. The central tumour has conductivity value of 4.0. The ideal recovered tumour for the central square pulse should be as seen in (b). However, the recovered distribution for the central element using the original Wexler 2-D EIT algorithm is more of a Gaussian (Bell-Shaped) type and has a peak conductivity value of 2.64 at 500 iterations. Similar observations were made for the 3-D algorithm. In the 3-D case, the recovered peak conductivity of the central element was 2.85 at 500 iterations.

In order to quantify, and later assess whether resolution at the diseased-to-normal tissue interface improves, a figure-of-merit is defined that characterizes how close the

recovered conductivity distribution is to the expected square pulse. The figure of merit is termed the conductivity profile ratio and is represented by the Greek letter τ. As seen in Figure 4.6 below, τ is defined as,

$$\tau = \frac{w_s h_r}{w_r h_s} \qquad [4.2]$$

w_r Width of Recovered Conductivity Distribution
w_s Width of Simulated Conductivity Distribution
h_r Height of Recovered Conductivity Distribution
h_s Height of Simulated Conductivity Distribution

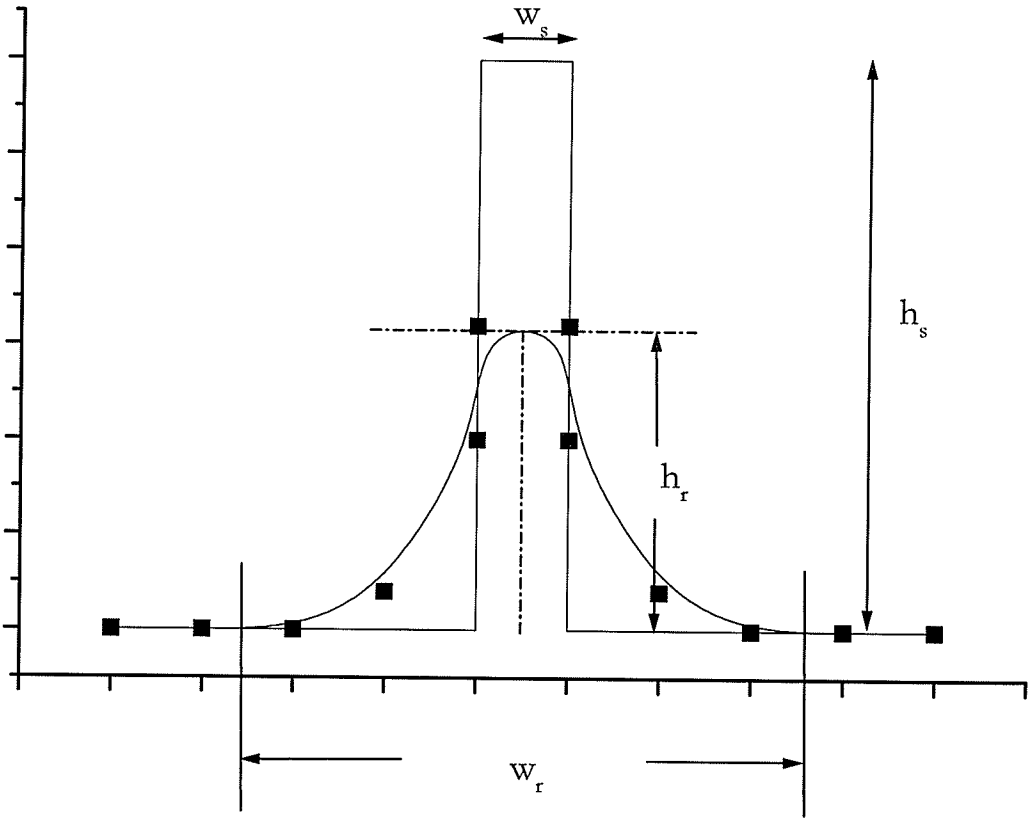

Figure 4.6: The conductivity profile ratio, τ. This parameter allows one to evaluate how close is the recovered conductivity distribution to the simulated conductivity distribution. w_r and h_r are the width and height of the recovered conductivity distribution. Similarly, w_s and h_s are the width and height of the simulated conductivity distribution. A value of 1.0 implies that the widths and heights of the simulated and recovered conductivity distribution is equal to each other.

4.8 Instrumentation or Measurement Device Noise Effect

From a review of literature, it was found that measurements made in EIT are subject to noise and drift artifacts. Boone *et al.*, 1995 [Boon95] provided a comprehensive assessment of noise and drift artifacts using the Sheffield Mark I system, and identified three possible sources of measurement artifact. These are the intrinsic noise in instrumentation of EIT, electrode-electrolyte noise and drift, and noise and drift in skin impedance. They suggested that the instruments contributed about 10%, 65% arose from the skin impedance and 25% arose from impedance variations in the tissue itself. Sinton *et al.*, 1992 [Sint92] published quantitative measurements of the Sheffield real-time EIT's [Brow87 and Smit90] noise performance in realistic conditions. They found image noise traded off against temporal or spatial resolution by filtering the images. Wang *et al.*, 1994 [Wang94] showed that noise increased by a factor of up to 30 from the periphery towards the center of a saline-filled phantom image. They proposed a method to equalize noise to a uniform level of about 16 dB.

The measurement noise effect introduced by instrumentation sensitivity was simulated using the original Wexler 2-D EIT algorithm. In the simple 2-D simulation model of breast tumour imaging, the region is divided into 9×9=81 finite elements. The background region is at a conductivity ratio of 1.0. The central tumour pixel has a conductivity value of 4.0. Sixteen electrodes are arranged on the mesh boundary and eight pairs of current injections/extractions are applied. *Sometimes* and *always* measurement patterns were employed to recover the image.

To simulate instrumentation or device noise, a pseudo-random number generator (written in C language) was developed and implemented in the algorithm to generate random instrumentation noise data so as to corrupt direct measured boundary potentials at node n from φ_n to φ_n^*. Images were recovered with an SNR (signal-to-noise ratio) of 70 down to 10 in 10-decibel (dB) intervals. Figure 4.7 below shows the graph of contrast, C, a parameter that was defined in Chapter 2 as the ratio of the

conductivity of the region of interest, i.e., the tumour to that of the background for both the *sometimes* and *always* measurement patterns as a function of SNR.

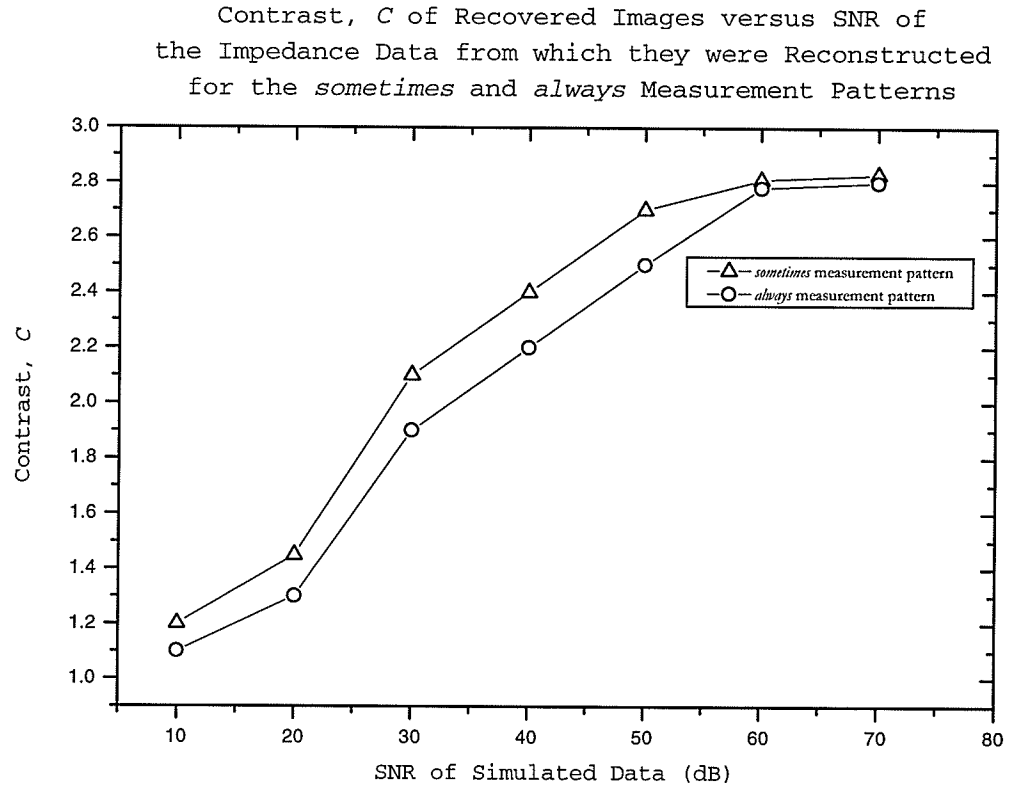

Figure 4.7: Contrast of the recovered images as a function of SNR for the *sometimes* and *always* measurement pattern using the 2-D original Wexler 2-D EIT algorithm. Note that the *sometimes* pattern provides the best contrast even at lower SNR. Results obtained with the 3-D algorithm provide slightly better contrast.

Figure 4.7 above shows graphs of contrast versus SNR for *sometimes* and always measurement pattern. Above 60 dB SNR, contrast curves reach plateaus that are essentially determined by the amplitude of reconstruction artifacts that extends out of the tumour element, in particular the observed "Tumour-Edge" effect observed above. The *sometimes* pattern exhibits higher contrast than the *always* pattern. Figure 4.6 can be used to relate contrast values to the visibility of the tumour object in the recovered images. With the *sometimes* pattern, the tumour is still distinguishable at an SNR of 20 dB.

4.9 Electrode-Electrolyte (or Electrode-Skin) Impedance Effect

The human skin is divided into three principal layers: The epidermis, dermis and the subcutaneous fat layer (or hypodermis) [Figure 4.8]. The outermost layer of the epidermis, i.e., the *stratum corneum*, is the site that is constantly worn out and replaced by new cells. The contact impedance of the electrode-electrolyte (electrode-skin) can sometimes be much greater than the underlying tissue [Rose88]. The skin-electrode impedance can cause measurement error [Boon95, Hua93, and Riu90] that will affect image quality [Boon96]. Furthermore, the type of image reconstruction employed will influence the effect of measurement error on the image. Boone *et al.*, 1995, using a linear back-projection reconstruction [Barb87], showed that a drift of 5%, from an initial impedance of 100 Ω, is sufficient to produce image distortion. Hua *et al.*, 1993 demonstrated, using an iterative scheme, that FEM models for electrodes can be used to improve performance of an EIT algorithm [Hua93].

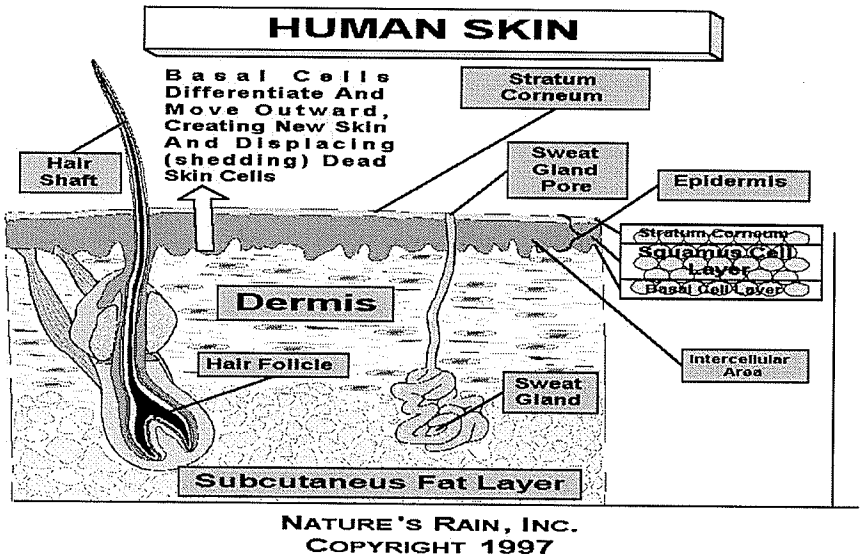

* Reprinted, with permission, from Nature's Rain, Inc., 1997.

Figure 4.8: Anatomy of the human skin. The human skin is divided into three principal layers: The epidermis, dermis and the subcutaneous fat layer (or hypodermis). The outermost layer of the epidermis, i.e., the *stratum corneum*, is the site that is constantly worn out and replaced by new cells. The contact impedance of the electrode-electrolyte can be much greater than the underlying skin. As such, the electrode-electrolyte impedance needs to be accounted for in image reconstruction.

In the Wexler algorithm, the *sometimes* measurement pattern is used to measure boundary potentials. As such, the effects of electrode-contact resistance are minimal, if any (see Appendix I for a complete discussion of reduced contact impedance). The impedance of the skin and that of the chestwall of the breast ought to be considered in the imaging reconstruction algorithm. To appropriately address the impedance effect of the skin and chestwall on image quality, accurate geometrical finite element models are required [Hua93]. Due to the scope of this thesis, the impedance effect of the skin and that of the chestwall are considered as future work and are not addressed here.

4.10 Electrode and Patient Motion Effect

Of interest to clinical imaging is an algorithm's ability to handle measurement device motion and patient movement. In EIT of breast imaging, since images are acquired with electrodes attached to the breasts, any spatial deviation from the point of contact can cause image artifacts [Saha85]. However, the image artifact caused by electrode motion is largely dependent on the image reconstruction algorithm employed. In the Wexler algorithm, since an iterative procedure is used for the field solutions (viz., the preconditioned conjugate gradient method), the preceding field solutions serve as starting approximations to the succeeding calculations. As such, electrode motion would not affect image quality significantly since the starting field values of the previous iteration, prior to motion, would be used to derive field solutions after the motion. To verify this argument, a two-dimensional simulation was performed (Figure 4.9 a-b).

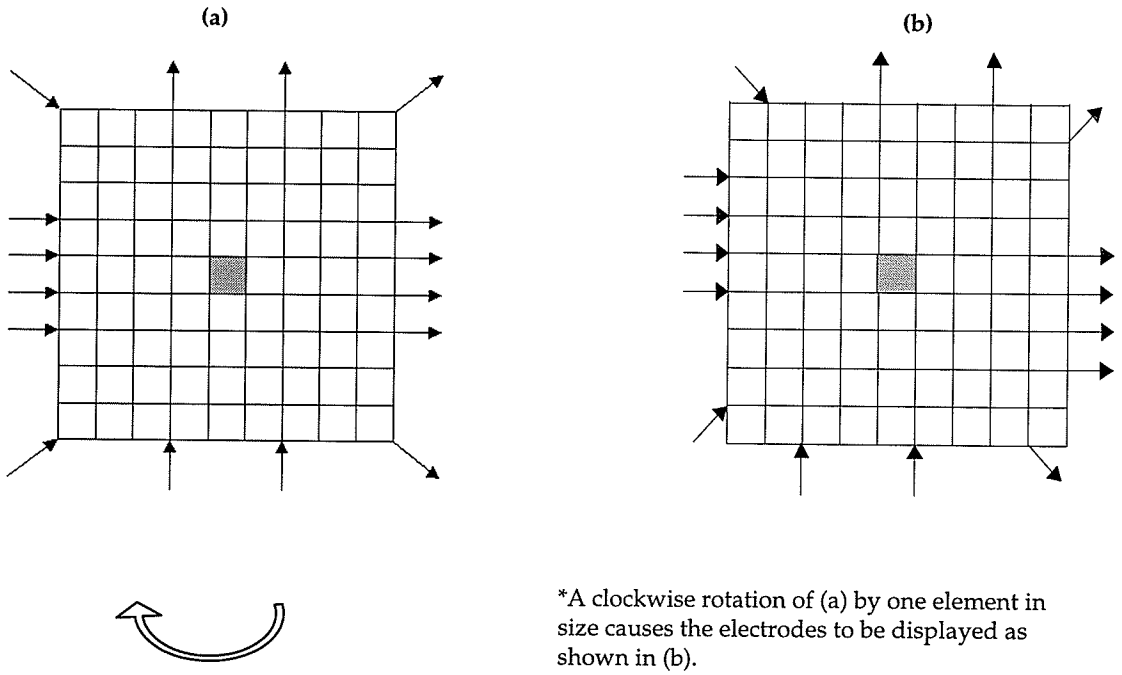

Figure 4.9 (a,b): (a) shows the initial location of the electrodes, (b) shows the final location of the electrodes after a spatial clockwise rotation of the electrodes by one element in size. Central tumour has conductivity value of 4.0 and background 1.0. Eight excitation pairs were utilized to recover the impedance images. Motion is simulated in the interval of 50 to 51 iterations.

In this simulation the region is divided into 9×9 = 81 elements. Conductivity of central tumour element is 4.0 and background is 1.0. Eight excitation pairs are used to recover the image at 50 iterations prior to motion simulation and at the 1st iteration after motion simulation. Electrode motion is simulated during the interval of the 50 to 51st iterations. Figure 4.10 (a-b) below shows the recovered image at 50 and 1st iteration respectively.

(a)

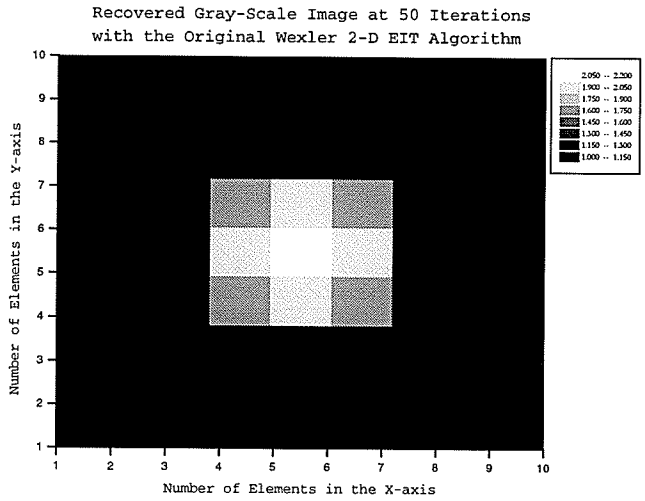

(b)

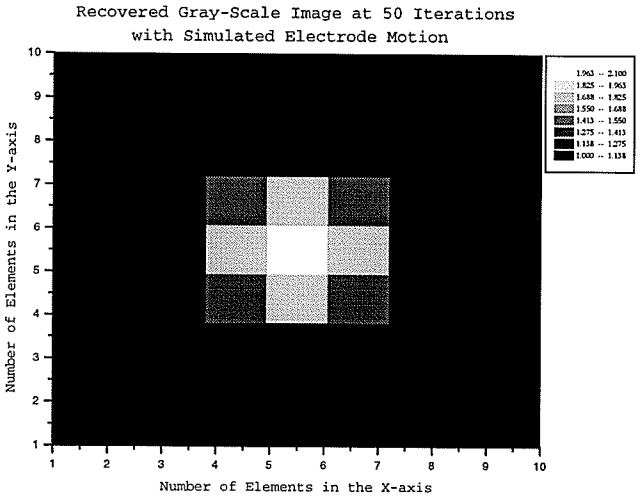

Figure 4.10 (a,b): (a) shows the recovered image before the electrode motion simulation, (b) shows the recovered image after the motion simulation. Note that both images are similar and that the conductivity of the recovered tumour element are 2.21 and 2.10 respectively.

It is obvious that the recovered image prior to electrode motion simulation is quite similar to the one recovered at the first iteration after electrode motion. The conductivity profile ratio τ for the tumour before and after electrode motion were 0.41 and 0.39 and the recovered peak conductivity magnitude of the tumour were 2.21 and 2.10 respectively. Similar observations were made for the 3-D original Wexler EIT algorithm.

Image artifact can also occur if the patient moves (i.e., consequently the breast is displaced) during imaging. This effect is quite common in existing imaging modalities e.g., MRI and CT [Herr97 and Qana99]. There are no reported studies of the effect of patient motion artifact on image quality in EIT literature. Here, a simplified simulation of a translational motion of a tumour, as a result of patient motion, is simulated using a simple 2-D model of the breast. The central tumour element above is translated from the initial spatial coordinates of (x=5, y=5) to (x=3, y=3). The tumour has conductivity 4.0 and is in a background region of conductivity 1.0. This simple translation is taken to simulate breast motion and consequently movement of the tumour. Breast motion is simulated during the interval of the 50th iteration to the 51st iteration. Figure 4.11 (a-b) below shows the recovered image at 50 iterations prior to motion simulation and at the first iteration after motion simulation.

(a)

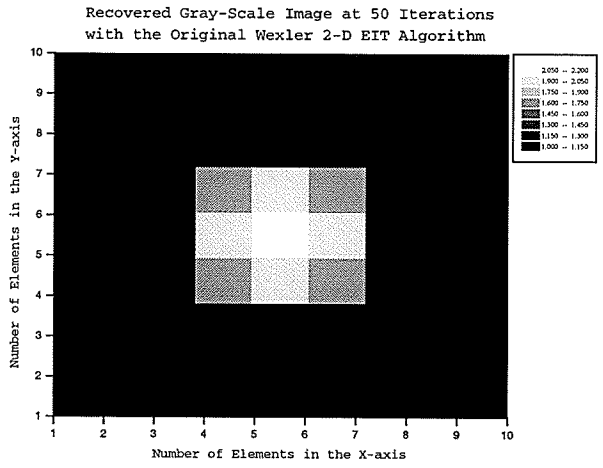

(b)

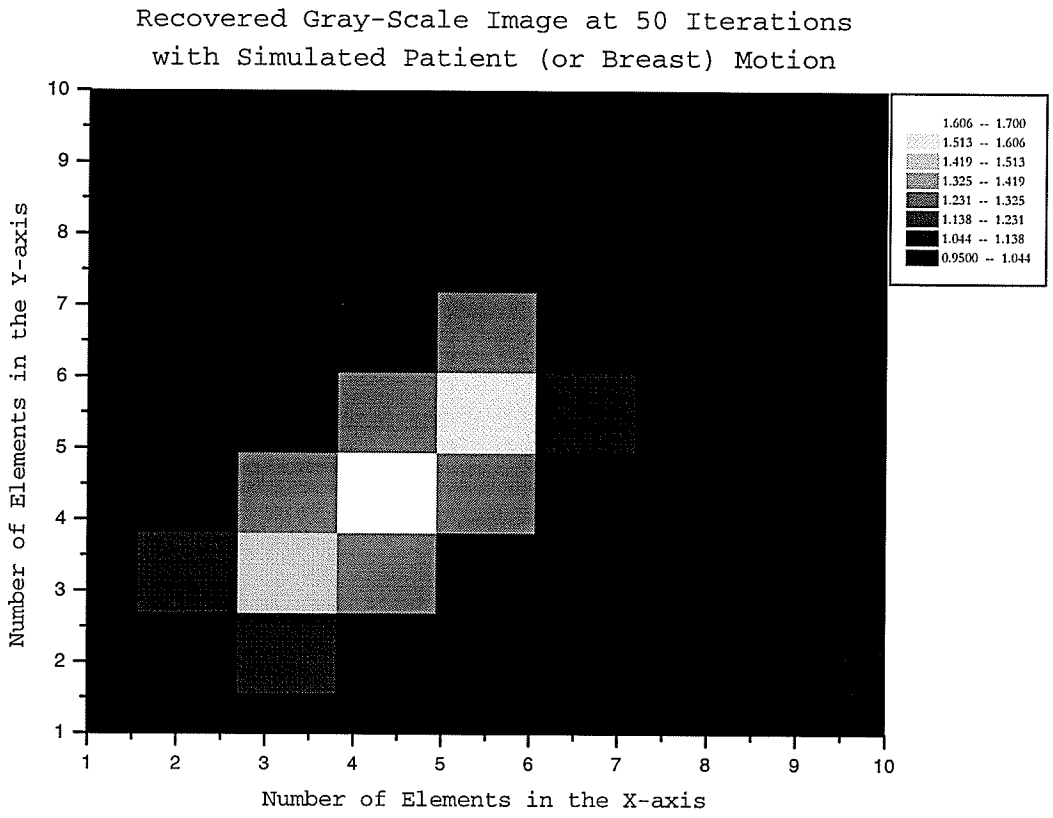

Figure 4.11 (a,b): (a) shows the recovered image before breast motion simulation, (b) shows the recovered image after the motion simulation. Note that a higher conductivity is seen at the (x=4, y=4) coordinates, midway between the initial and final coordinates.

From above simulation, it can be seen that the Wexler EIT algorithm will not perform that accurately in the presence of patient motion. It did recover a distribution, though not the correct one. There are a few ways to resolve patient motion in EIT. An obvious one is to improve the original convergence rate of the Wexler algorithm within seconds interval so patient motion is reduced. The other is to quantify loss of resolution from the motion and compensate for it in the algorithm. The latter had been attempted successfully in MRI imaging of the heart [Muru94]. In his MSc dissertation, Murugan, 1994 showed that contrast loss can be quantified and compensated for to improve overall resolution. This was attempted for MRI SPAMM tag contrast imaging [Muru94]. A similar idea can be used here.

4.11 Effect of the Third Dimension on the 2-D Wexler EIT System

Two-dimensional (2-D) impedance images are usually made from planar arrangements of electrodes [Moru96]. However, electric fields cannot be constrained to flow in a 2-D plane in a 3-D object. Conductivity variations usually depend on all three coordinates and hence voltage variation throughout a 3-D imaging region cannot be assumed to be in the 2-D plane only. As such, off-plane impedance changes, in most cases, imply that 2-D measurements are subject to errors. Kuzuoglu *et al.*, 1992 argued that the correct mathematical model of a physical system (for example, the human breast) ought to be represented in three-dimension [Kuzu92]. However, the use of 3-D finite element routines, as argued by Kuzuoglu *et al.*, 1992, usually leads to a few major shortcomings. In particular, excessive storage requirements are needed and with some intensive computation. For example, if one uses a 100×100×100 element model (i.e., 1,000,000 unknowns), this would result in 999,999 linearly independent measurements (or equations) to solve simultaneously, a clearly formidable computing task.

For a better understanding of the effect of the third dimension on a two-dimensional EIT system, an experimental study is carried out using the Wexler 2-D image reconstruction algorithm on a simulated 3-D cubic imaging region. In this simulation the finite element mesh was created using standard linear elements with 8 nodes (see Appendix I). The computer model adopted is a cube of 9×9×9 = 729 elements (or voxels) with a central Dirac delta element representing a tumour of conductivity 4.0 within the homogeneous region of conductivity 1.0 (see Figure 3.4, Chapter 3). Sixteen electrodes were arranged on a horizontal plane, centered on the 5th Layer as shown in Figure 3.4. The minimum number of excitation pairs needed to recover the 2-D planar images, using the *sometimes* pattern, was determined to be equal to eight. The original Wexler 2-D EIT algorithm was used to recover images over 50 iterations. Recovered images were obtained when the tumour was at the central position (x=5, y=5, and z=5), and at the following off-plane positions (x=5, y= 5, z=

4; and x=5, y=5, and z=3). The recovered 2-D images are shown in Figure 4.12 below along with the cross-sectional profiles.

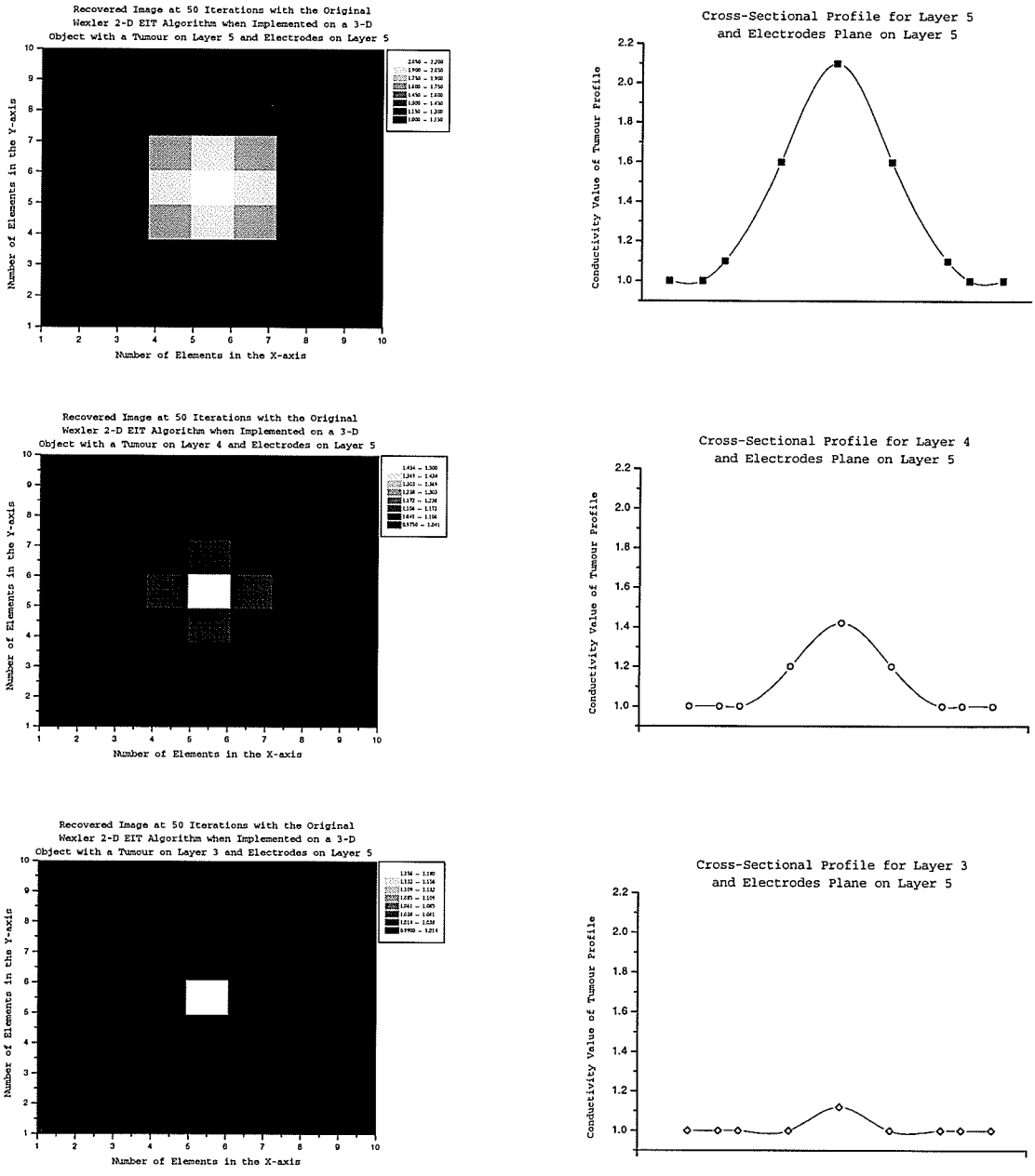

Figure 4.12: Contribution from the off-plane when using the 2-D Wexler EIT algorithm to image a 3-D object. This renders interpretation of EIT images difficult and should be addresses in the image reconstruction algorithm.

4.12 Discussion

An investigation of the characteristics and 'dynamics' of the original Wexler EIT image reconstruction algorithms, with potential in the detection and diagnosis of breast cancer, has yielded some important observations. The tests and effects that were performed here had the purpose of determining whether the original Wexler EIT algorithm could satisfy the standard requirements expected of a potential clinical breast cancer image-reconstruction method. The results of computer simulations are presented and discussed.

In section 4.2, the effect of the initial (or starting) conductivity distribution on the iterative Wexler 2-D and 3-D EIT algorithms was investigated. It was observed that a good starting value would produce correct results, while a poor initial guess may lead to slow convergence or may never converge. This observation is supported by many other studies where incorporating a priori information within the image reconstruction algorithm has led to improve convergence rate and subsequent improved image quality [Avis95 and Mees95]. In the case where the assumed (or initial) conductivity distribution is equal to the exact distribution, the Wexler 2-D and 3-D EIT algorithms converge in the first iteration. This observation is an indication of the accuracy of the image reconstruction algorithm and code.

In section 4.3, an investigation was performed to derive the optimal excitation and measurement pattern configuration. Using a multi-port network formulation as discretized models, along with sensitivity analyses and graph theory, Mu, 1994 [Mu94] derived some interesting observations on the effects of different excitation patterns on the ability of an EIT algorithm to recover the image. Mu's observations were implemented on simple 2-D and 3-D computer simulations of breast cancer imaging. From the results of simulations it was observed that the Wexler algorithm addressed problems that are slightly under-determined and performs well at determinacy higher than 1.0. The *sometimes* measurement pattern recovered impedance images faster and with more accuracy than the *always* pattern, which uses all measured boundary

potentials including those at active electrode sites. Excitation patterns that employed a symmetrical or near-symmetrical configuration provide faster convergence and improved image quality. The combination of minimal node involvement, symmetrical or near-symmetrical excitation patterns, and *sometimes* measurement patterns provide the optimal configuration for the imaging of breast tumour.

In Section 4.4, an investigation into the finite element size effect on convergence rate and image quality was conducted. Mu, 1994 described a procedure that starts with a coarse mesh to obtain an initial guess and a fine mesh to recover the image accurately in the solution of the inverse problem. Mu argued and demonstrated that the convergence period would be greatly reduced if a coarse mesh were used first to obtain an approximate solution, then a finer mesh to reach the true image. The observations derived by Mu [Mu94] were implemented on the standard 2-D and 3-D computer simulation examples for breast cancer imaging. Results of simulations indicated that Mu's scheme improves the convergence rate and subsequently the image quality.

In section 4.5, the effect on convergence speed of the spatial location of the tumour was demonstrated. It was observed that better convergence rate is attained if the tumour is located on the periphery of the object than if it is located in an intermediate or central position within the object. It was also observed that conductivity of the element on the edge of a central tumour element increases with iteration count at early iterations. The conductivity value of the edge element then decreases at later iterations. This phenomenon appeared to affect the resolution at the sharp edges of the diseased-to-normal tissue interface. This effect was termed the "Tumour-Edge" effect. If the potential and conductivity distributions are known from past history, the distributions at convergence can be determined by interpolation. This observation will prove crucial in developing a method to improve the convergence speed of the algorithm, as is discussed further in Chapter 5.

In section 4.6, an investigation of the behaviour of spatial resolution as a function of location of tumour was performed. It was determined that the resolution of EIT is spatially variant. The resolution of a tumour at a peripheral location is superior to that at an intermediate and/or central location. When compared to values obtained from the literature, the spatial resolution of the original Wexler 2-D and 3-D EIT were found to be quite similar to those obtained by [Ider95 and Meth96]. It is apparent that if the loss in resolution, in particular at the diseased-to-normal tissue interface, as a function of tumour spatial location could be compensated for, EIT spatial resolution would improve drastically. This issue is further investigated in Chapter 6.

The "Tumour-Edge" effect identified in Section 4.5 and 4.6 was investigated further in Section 4.7. It was observed that the Wexler EIT algorithm fails to give an acceptable image with sharp edges in a reasonable time. The higher conductivity value of the tumour has an effect on the surrounding edge elements. This affects the recovered conductivity value of the edge elements, since their conductivity values are much higher than the background.

To assess the effect of the "Tumour-Edge" phenomenon on recovered impedance images, simulations were performed. It was observed that if the original 2-D Wexler algorithm is used to image a conductivity function of the form $\kappa = 1 + \sin^2 x \cdot \sin^2 y$ located within a host medium with $\kappa = 1$, the algorithm converges in only a few iterations with high image quality. This represents a smoothly varying conductivity distribution over a 2-D case. However, if the conductivity distribution has the form of a square pulse, the algorithm takes much longer to converge and the resolution at the diseased-to-normal tissue interface is quite poor. To quantify the difference between the simulated and recovered conductivity at the tumour location, a figure of merit was introduced. The figure-of-merit was termed the conductivity profile ratio and was represented by τ. This provides a measure of how close the recovered distribution is to the simulated distribution and is used to assess improvement in

spatial resolution at diseased-to-normal tissue interface. The resolution at diseased-to-normal tissue interface is addressed further in Chapter 6.

In section 4.8, the effect of instrumentation or device noise on convergence rate and recovered image quality was investigated. It was observed that, with the *sometimes* measurement pattern, tumours of appropriate contrast could be distinguished adequately from the background region. However, for the *always* measurement pattern, noise would affect image quality. The fact that the algorithm can handle noise that will be characteristic of a clinical EIT-based system further adds to its potential in medicine.

In section 4.9, the effect of electrode-electrolyte (or electrode-skin) impedance on recovered image quality was discussed. It was determined that for the Wexler algorithm the effects of electrode-contact resistance are minimal, if any. Furthermore, accurate finite element models of the impedance of the skin and that of the chestwall ought to be considered in the imaging reconstruction algorithm.

In section 4.10, the effect of electrode and patient motion was investigated on a simple breast model. It was shown that the results of the original Wexler EIT algorithm is not affected significantly with electrode motion. This is so since the Wexler algorithm is an iterative procedure and the preceding field solutions serve as starting approximations to the succeeding calculations. As such, electrode motion would not affect image quality significantly since the starting field values of the previous iteration, prior to motion, would be used to derive field solutions after the motion.

Simulation of breast motion showed that the original Wexler EIT algorithm would not perform that accurately in the presence of patient motion. Methods were suggested that would address this issue. An obvious one was to improve the original convergence rate of the Wexler algorithm drastically so that radiologically useful images are obtained within seconds, avoiding any contribution to image deterioration from patient motion during imaging. A more practical approach was to quantify the

loss in resolution from the motion and compensate for it within the image reconstruction algorithm. The success of the later approach was demonstrated in an MSc dissertation on MRI cardioimaging.

An experimental study of the effect of the third dimension on 2-D Wexler EIT system was conducted in Section 4.11. It was observed through simulations that the 2-D Wexler EIT system inevitably produces three-dimensional current flow. This renders interpretation of EIT images difficult. This study has shown that a detailed understanding of the nature of this 3-D effect is essential and ought not to be neglected. This effect has justified the focus of this thesis on the development of an improved Wexler 3-D EIT algorithm rather than the 2-D algorithm.

4.13 Summary

The characteristic of the Wexler EIT 'static' imaging algorithm was assessed to determine whether the algorithm meets expected clinical requirements. To be of clinical potential, imaging ought to be possible at fast rate and with high accuracy. Further, noise, electrode-skin contact impedance, and patient motion would need to be appropriately accommodated. The final recovered image ought to be of high diagnostic quality in order to determining proper patient treatment and prognosis.

The Wexler EIT algorithm appears to satisfy most of the criteria of a clinical imaging algorithm. It can handle instrumentation noise, image distortion due to electrode motion, distinguish benign from malignant tumour, and is relatively robust. However, because of the fact that time for image recovery and spatial resolution are not of clinical standards, the algorithm is not yet suitable for imaging small breast tumours.

Two crucial observations were made in this chapter. First, it was observed that knowing the history of conductivity/potential distributions as a function of iteration, the future conductivity/potential distribution could be deduced by modelling the past behavior and extrapolating to later iterations. Second, the overall spatial resolution in EIT was shown to be inappropriate for clinical purposes, in particular, there was inadequate resolution at sharp edges (i.e., at clear demarcation between diseased-to-normal tissue interface). If a resolution compensation scheme is applied during image reconstruction, the overall spatial resolution ought to improve. The issues of convergence and spatial resolution are investigated, and methods are devised to improve both for the original 3-D Wexler EIT algorithm in the following two chapters.

Chapter 5

A Modeller-Predictor-Corrector (MPC) Algorithm to Improve Time of Convergence for the Original Wexler 3-D EIT Algorithm

5.1 Introduction

In recent reviews on EIT's algorithmic performance, the original Wexler algorithm - an error minimization scheme - was characterized as being slowly convergent [York87, Isaa92 and Kyri93]. Although relative to other iterative methods the convergence rate of the Wexler algorithm is somewhat slow, fundamentally the algorithm is superior in solving the physics of the inverse nonlinear EIT problem. In particular, the algorithm makes no assumption as to the pattern of flow of electrical current within a medium. However, as shown previously, its resultant time of convergence and spatial resolution of the recovered images are not of clinical imaging potential (e.g., in the imaging of breast cancer). With that in mind, the focus of this chapter is on improving the convergence rate of the original Wexler EIT algorithm for potential clinically. The issue of low spatial resolution is discussed in the next chapter.

Initially, the low convergence rate of the original Wexler algorithm is demonstrated. Thereafter, a new Modeller-Predictor-Corrector (MPC) scheme is developed and implemented on simplified 3-D computer simulations of small breast tumour imaging. Results of computer simulations using the MPC method are discussed and summarized.

5.2 Time of Convergence of the Original Wexler 3-D EIT Algorithm

The time of convergence of the original Wexler 3-D EIT algorithm was demonstrated earlier (see Chapter 3, Section 3.4 and Chapter 4, Section 4.5). It was observed that the algorithm was slowly convergent (i.e., took relatively more iterations to converge) and, considering the time per iteration, was not of clinical imaging potential when compared to existing imaging modalities. For the purpose of the present discussion, a slightly different 3-D computer simulation setup of breast tumour imaging is employed (see Figure 5.0).

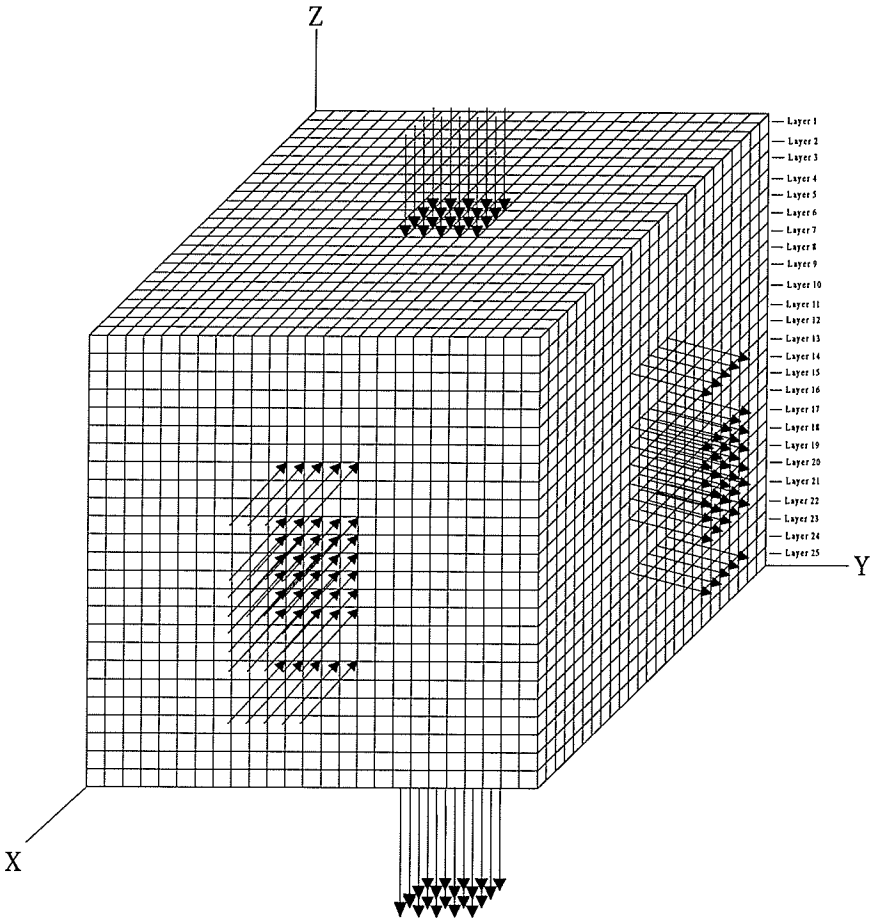

Figure 5.0: Simplified 3-D breast model. Volume has 15625 elements. One hundred and ten excitation pairs were employed. The *'sometimes'* measurement pattern was used. The tumour element is located on Layer 13, with coordinates (x=13,y=13, and z=13). Though not fully realistic, this model provides a means to investigate the problem of convergence rate in the detection of small tumours of the breast.

In this 3-D simulation setup, a cube is used to represent a simplified model of the breast. The model is divided into 15625 (i.e., 25×25×25) finite volumetric elements (i.e., voxels), with the central voxel representing the tumour (see Figure 5.0). The tumour element is located at the spatial coordinates (x=13, y=13, and z=13). Two hundred and twenty electrodes were arranged over the 3-D object surface, and a minimum number of one hundred and ten injections/extractions views were employed to reconstruct the 3-D images. This corresponds to a determinacy of 1.15 using the '*sometimes*' measurement pattern. The central voxel representing the tumour has a conductivity of 4.0 and the background region has conductivity of value 1.0. Measurements are not taken on one side of the cube. This side represents the side of the breast that is attached to the chest wall.

Figure 5.1 below shows the norm of the error term plotted as a function of iteration for the recovered 3-D breast model setup of Figure 5.0 above. It is obvious that the algorithm tends to converge faster at early iterations and appears to be almost "dormant" at later iterations. Though the time to converge is situation dependent, this setup took approximately 104 minutes (at about 2,200 iterations) to approach converge while running on a SUNW, SPARCstation-4.

It is obvious that in order for the Wexler 3-D EIT to be of potential in the imaging of small breast tumour, the convergence rate or the time for a complete medical scan ought to be improved drastically. The Modeller-Predictor-Corrector (MPC) algorithm developed in the next section attempts to improve the time of convergence so as to be of clinical potential.

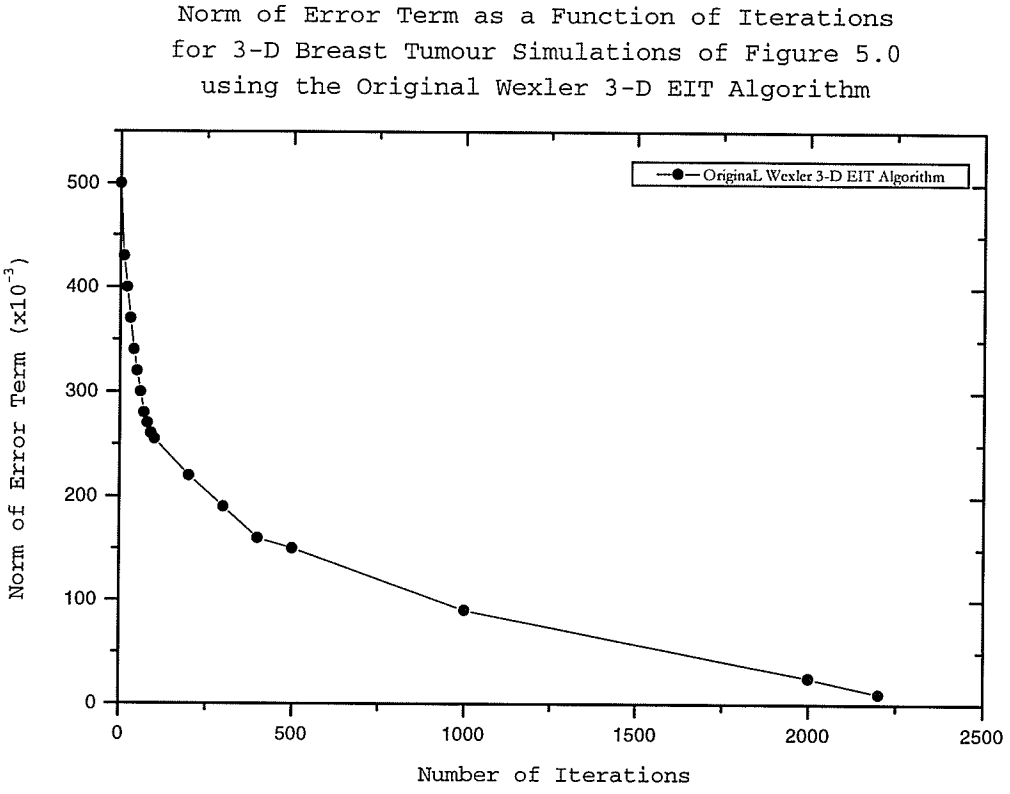

Figure 5.1: Norm of error term as a function of iterations for the simplified computer simulation setup of Figure 5.0 using the original Wexler 3-D EIT algorithm. Note that the algorithm is slowly convergent. The norm of error term is defined in Chapter 3, Section 3.4

5.3 The Modeller-Predictor-Corrector (MPC) Algorithm

Based on the observations reported in Chapter 4, it is obvious that with a knowledge of the history of conductivity distributions as a function of iteration, one can condense and summarize the data by fitting it to a model. Modeling, in this case, can be used as a kind of constrained extrapolation, where a few given data are extended into a continuous function, with an idea of the function type. Ideally, extrapolating to or close to the exact conductivity distribution (i.e., the distribution being sought) ought to speed up the time for convergence. At what iteration does one have to interpolate in order for the algorithm to converge (i.e., where measured is equal to exact conductivity distribution)? A naïve approach would be to extrapolate iteratively (i.e., make a guess iteration number and interpolate to that number), while successively comparing conductivity distribution, until convergence is attained. This is the scheme employed in the multistep predictor-corrector approach to convergence as implemented by Strobel, 1996 [Stro96].

In the multistep approach adopted by Strobel 1996, a 'characteristic' equation of the processing algorithm is derived from past known conductivity distribution and interpolated iteratively, via multiple guess of iteration number, to exact distribution until convergence. The derived equation is assumed to be characteristic of the imaging algorithm. The multistep approach was implemented in the Wexler EIT algorithm with little, if any, success [Stro96]. Though the convergence rate of the initial Wexler EIT algorithm improved, it was yet not optimal for clinical breast imaging. The Modeller-Predictor-Corrector (MPC) scheme developed here attempts to solve this problem. In the MPC algorithm discussed below, both the potential and conductivity distributions are modelled from past behaviour in a least-squares manner and no guess at iteration number is needed as in the multistep approach to convergence discussed by Strobel 1996.

The purpose of the Modeller-Predictor-Corrector (MPC) scheme is to improve the time of convergence of the original Wexler EIT algorithm. In this approach, the potential (or voltage, ϕ) and conductivity (κ) distributions of the processing technique (i.e., the original Wexler algorithm) are **modelled** nonlinearly over the first to n iterations. The modeled/fitted potential equation as a function of iteration is then extrapolated in order to **predict** the number of iterations that is equivalent to the measured/exact potential distribution. The exact potential is used to seek the iteration number at which the algorithm converges. That iteration number is then used in the modelled conductivity equation to derive the corresponding conductivity distribution. It is expected that the derived conductivity distribution will be close to if not equal to the distribution that is being sought. Realizing that the derived conductivity was arrived at by interpolation, thus error-bound, the predicted conductivity distribution is then used to reinitialize the processing algorithm. The reinitialization step allows **correction** of the derived conductivity distribution until convergence is attained.

In summary the MPC algorithm proceeds as follows (see Figure 5.2)

Step 1: Model ϕ and κ as a function of iteration i.

The recovered potential and conductivity distributions, over the first to n iterations, are modelled using the nonlinear least-squares fitting scheme of Levenberg-Marquardt (LM) (see Section 5.4 for a discussion of the Levenberg-Marquardt procedure). The fitted mathematical equations as a function of iteration i, are expressed as:

$$\phi = \phi(i) \qquad [5.0]$$

$$\kappa = \kappa(i) \qquad [5.1]$$

where ϕ and κ are the potential (or voltage) and conductivity distributions at iteration i respectively.

In order to use the Levenberg-Marquardt least-squares fitting algorithm and to ensure correct "fit parameters", the correct actual physical peak shapes (i.e., the fit functions) for the potential and conductivity distributions history are required. In Chapter 4, Section 4.6, it was demonstrated that the actual "fit functions" for the conductivity distributions were in the nature of types of three-parameter exponential or logarithmic functions. Due to the fact that the LM method is an iterative process that requires a user-defined "fit-function", any interpretations from the final results are only as good as the initial inputs. After all, the algorithm only optimizes the information fed into it; it can not interpret it for the user. This is discussed further in Section 5.4.

Step 2: Predict κ at iteration $I(\kappa_I)$

Once the optimal equations for potential, ϕ, and conductivity, κ are derived from Step 1, the potential relation (5.0) is then used to derive the iteration number I, at which the algorithm is considered to have convergence. This is accomplished by substituting the known potential distribution, ϕ_{known}, obtained through direct measurements, into the mathematical relation (5.0). Unlike in the multistep approach, where guesses at iteration number are taken repeatedly until convergence, in the MPC method no guess at iteration number is made. Rather, the known potential (ϕ_{known}) is used to derive the correct iteration number, I for which the algorithm is considered to converge.

$$\phi_{known} = \phi(I) \qquad [5.2]$$

$$\kappa_d = \kappa(I) \qquad [5.3]$$

Thereafter, the derived number of iterations, I, is used in the conductivity relation (5.3) to derive the corresponding conductivity distribution (κ_d). At this stage, it is assumed that the derived conductivity distribution at iteration (I) is equivalent to or close to the distribution being sought. The algorithm then goes on to Step 3.

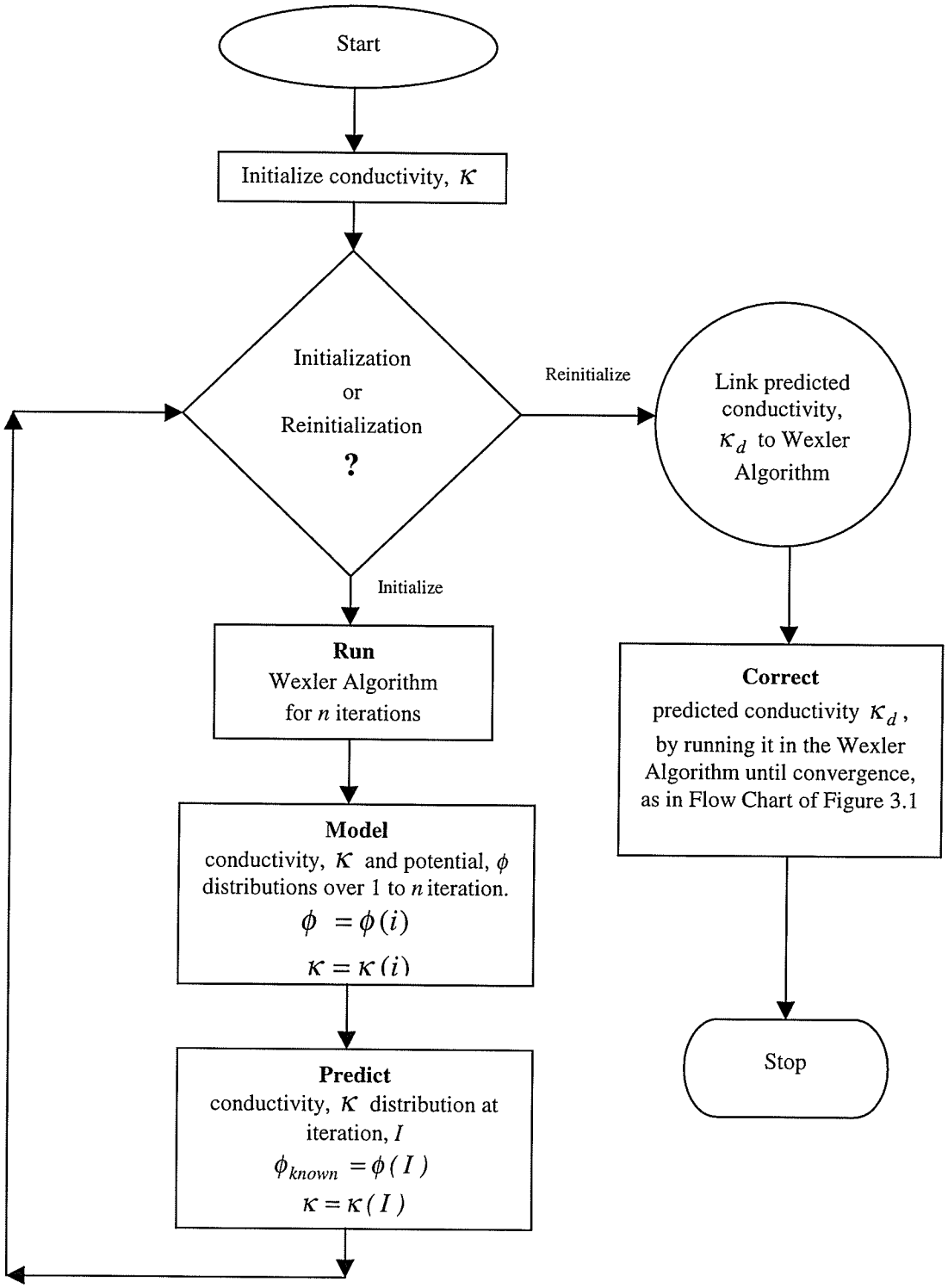

Figure 5.2: The MPC flow chart. The algorithm is initialized using an assumed conductivity distribution. A decision is then made if it is an initialization or reinitialization procedure. If it is initialization, the algorithm proceeds to the Run, Model, and Predict steps respectively. The derived conductivity κ_d, at the end of the Predict stage, gets fed back to the decision phase. At this point, the algorithm recognizes that this is the reinitialization step. This, in turn, is fed to the Wexler Algorithm for error correction until convergence.

Step 3: Correct κ_d by re-initializing

The earlier assumption of Step 2, that the derived conductivity distribution (κ_d) at iteration (*I*) is equal to the distribution being sought is not entirely correct. It is obvious that (κ_d) was arrived at by some interpolation operations, quite likely it contains some error. To minimize the errors that might have been introduced at Steps 1 and 2, the derived conductivity distribution (κ_d) is corrected by re-initializing. Re-initialization involves using the derived conductivity distribution (κ_d) as the initial starting conductivity distribution in Step 1 of the original Wexler EIT algorithm flow chart (see Figure 3.1, Chapter 3). As well as removing any discrepancy, the re-initialization step assures the correct physical approach of the original Wexler EIT image reconstruction algorithm.

5.4 The Levenberg-Marquardt (LM) Least-Squares Fitting Algorithm

As stated previously, EIT is a nonlinear inverse problem and as such data modelling requires a nonlinear approach. Mathematically, the building blocks of any fitting procedure are:

- The data which represent the results of some measurements in which one or several *independent* (input) variables (*x1, x2, x3)* were varied over a certain range in a controllable manner so as to produce the measured *dependent* (output) variable(s) *y1, y2, y3* .....

- The mathematical expression (a function or a set thereof) in the form

$$y1=f1(x1,x2,x3,\ldots;p1,p2,p3,\ldots)$$
$$y2=f2(x1,x2,x3,\ldots;p1,p2,p3,\ldots)$$
$$y3=f3(x1,x2,x3,\ldots;p1,p2,p3,\ldots)$$

  which represents the theoretical model believed to explain the process that produced the experimental data. The model usually depends on one or more parameters, *p1, p2, or p3*. The aim of the fitting procedure is to find the values of the parameters which best describe the data.

It is necessary to design a figure-of-merit function (or merit function for short) that measures the agreement between the data and the model with a particular choice of parameters. As will be discussed shortly, in the Levenberg-Marquardt (LM) method, the merit function employed is the *Chi-Square* (χ^2) function. The parameters of the model are then adjusted to achieve a minimum in the merit function, yielding best-fit parameters. The adjustment process is then a problem in minimization in many dimensions. To be genuinely useful, a fitting procedure should provide 1) parameters, 2) error estimates on the parameters, and 3) a statistical measure of goodness of fit [Pres86]. The Levenberg-Marquardt least-squares algorithm satisfies these requirements.

The Levenberg-Marquardt (LM) method is the most widely used algorithm in nonlinear least squares fitting [Doga83, Pres86 and Reic92]. It is very useful for finding solutions to complex fitting problems. Basically, the Levenberg-Marquardt method [Leve44 and Marq63] combines the robustness of a steepest descent method with the efficiency of a Gauss-Newton method [Bevi92]. The steepest descent and Gauss-Newton methods are comprehensively discussed in Press *et al.*, 1986 [Pres86], Fletcher, 1987 [Flet87], and Reich, 1992 [Reic92]. For the purpose of this discussion and its application here, only the key features of the Levenberg-Marquardt algorithm, an algorithm that switches continuously from a gradient method far from the minimum to a Gauss-Newton step as the minimum is approached, are discussed [Pres86].

As shown by Press *et al.*, 1986 [Pres86], the following quadratic form can approximate a general nonlinear fit equation,

$$\chi^2(\mathbf{a}) \approx \gamma - \mathbf{d}\cdot\mathbf{a} + \frac{1}{2}\mathbf{a}\cdot\mathbf{D}\cdot\mathbf{a} \qquad [5.4]$$

where χ^2 is the merit function, the parameter used to determine what the best fit is for varying ($\mathbf{a}$) which is the set of M unknown fit parameters ($\mathbf{a_1}$, $\mathbf{a_2}$, ..., $\mathbf{a_m}$). γ is the shape or curve that is being fitted. $\mathbf{D}$ is an M×M Hessian matrix, the second

partial derivatives of the functions used for fitting and **d** is a gradient vector (steepest descent of order M), the first partial derivatives of the functions.

For poor initial approximations, the method of steepest descent will localize the fit parameters by finding the next parameter values ($\mathbf{a}_{next}$), using the current fit parameters ($\mathbf{a}_{cur}$), via the following equation,

$$\mathbf{a}_{next} = \mathbf{a}_{cur} + \mathbf{D}^{-1} \cdot [\nabla\chi^2 (\mathbf{a}_{cur})] \qquad [5.5]$$

If the initial guess is fairly close, the Hessian matrix [Pres86] method works better for finding the minimized values ($\mathbf{a}_{min}$), by using the current fit parameters (a_{cur}) as shown below,

$$\mathbf{a}_{min} = \mathbf{a}_{cur} - \boldsymbol{const} \times \nabla\chi^2 (\mathbf{a}_{cur}) \qquad [5.6]$$

Upon carrying out the partial derivatives of the merit function, χ^2 and rearranging, a vector (β) and a matrix (α) are derived that represents the fit parameters,

$$\beta_k \equiv -\frac{1}{2}\frac{\partial\chi^2}{\partial a_k} \qquad [5.7]$$

$$\alpha_{kl} \equiv \frac{1}{2}\frac{\partial^2\chi^2}{\partial a_k \partial a_l} \qquad [5.8]$$

After determining the partial derivatives from the gradients, a second derivative term arises, causing a destabilization during the fitting routine. The contribution of the second term, which tends to cancel itself out when summed over all data points (N), can be neglected, simplifying the α_{kl} term. Hence, ignoring the term gives the following for the Hessian matrix, when summed over all the data points in the curve, N,

$$\alpha_{kl} = \sum_i^N \frac{1}{\sigma_i^2}\left[\frac{\partial y(x_i;\mathbf{a})}{\partial a_k}\,\frac{\partial y(x_i;\mathbf{a})}{\partial a_l}\right] \qquad [5.9]$$

Using the inverse of the Hessian matrix, the step size can be rewritten as a set of linear equations that can be solved for the new step size, δa_l,

$$\delta a_l = \frac{1}{\alpha_{kl}} \times \beta_k \qquad [5.10]$$

The new step, is then added to the current value, and tested in the merit equation for "best fit". Similarly, the steepest descent formula of equation [5.6] translates to,

$$\delta a_l = constant \times \beta_l \qquad [5.11]$$

which is then subtracted from the current value to give the new parameters for testing the "best fit". The final "best fit" solution is arrived when χ^2 is at a minimum, or when β_k values are 0 at all k values. It should be noted that any changes in α_{kl} would not affect the final parameter fit values, since its only purpose is to determine the rate (i.e., the step size) at which the minimum is obtained.

The Levenberg-Marquardt method combines the inherent stability of steepest descent with the quadratic convergence rate of the Gauss-Newton method as described in the previous section. The algorithm uses the method of steepest descent to determine the step size when the results are far from the minimum,

$$\delta a_l = constant \times \beta_l$$

$$\delta a_l = \frac{1}{\alpha_{kl}} \times \beta_k$$

But as the solution approaches the minimum, the algorithm switches to the Hessian matrix for determining the step size in order to zero in on the best fit. Marquardt realized that by combining equations [5.10 and 5.11], the full advantage of both methods can be derived [5.12],

$$\delta a_l = \sum_{l=1}^{M} \frac{1}{\alpha'_{kl}} \times \beta_k \qquad [5.12]$$

where α' is a new matrix obtained by combining [5.10 and 5.11] and is defined as,

$$\alpha'_{jj} \equiv \alpha_{jj}\,(1+\lambda) \quad (j = 1....M) \qquad [5.13]$$

$$\alpha'_{jk} \equiv \alpha_{jk} \qquad (j \neq k) \qquad [5.14]$$

and λ ($\lambda >> 1$) is a regularization constant (or fudge factor) to regulate the step size. Marquardt's equation [5.12] spans the full range of the fitting processes, from the method of steepest descent to the Hessian matrix (or Gauss-Newton) method.

The algorithm is usually implemented as follows:

- Compute $\chi^2(\mathbf{a})$.
- Guess at a modest value for λ, say $\lambda = 0.001$.
- Solve equation [5.12] for $\delta\mathbf{a}$ and evaluate $\chi^2(\mathbf{a} + \delta\mathbf{a})$.
- If $\chi^2(\mathbf{a} + \delta\mathbf{a}) \geq \chi^2(\mathbf{a})$, *increase* λ by a factor of 10 (or any other substantial factor).
- If $\chi^2(\mathbf{a} + \delta\mathbf{a}) < \chi^2(\mathbf{a})$, *decrease* λ by a factor of 10, and update the trial solution.

The algorithm iterates until some convergence criterion is reached. Typically this means when a minimum in the reduced χ^2 is reached.

The LM method works very well in practice and has become the standard of the nonlinear least-square routine [Bevi92]. The Levenberg-Marquart scheme is implemented in Step1 of the Modeller-Predictor-Corrector to model potential (voltage) and conductivity distributions from a knowledge of their past history and an idea of their correct actual physical peak shapes (i.e., the fit function).

5.5 3-D Computer Simulations using the MPC Algorithm

In order to demonstrate the effectiveness of the Modeller-Predictor-Corrector (MPC) scheme in improving the convergence rate of the original Wexler 3-D EIT algorithm, the previous 3-D simulation of small breast tumour imaging described in Section 5.2 is repeated with the MPC scheme.

The modelling is done over the first two to fifteen iterations, conductivity and potential distributions are predicted at the 15^{th} iteration, and the correction is done over the next five iterations (i.e., a total of 20 iterations for an approximate time of 7.4 minutes). To demonstrate and compare its ability in improving convergence rate, a comparison to the original Wexler and multistep approach of Strobel, 1996 is provided. Figure 5.3 below shows the error norm plot as a function of iteration count for the original Wexler, Strobel's multistep, and the MPC methods employed here.

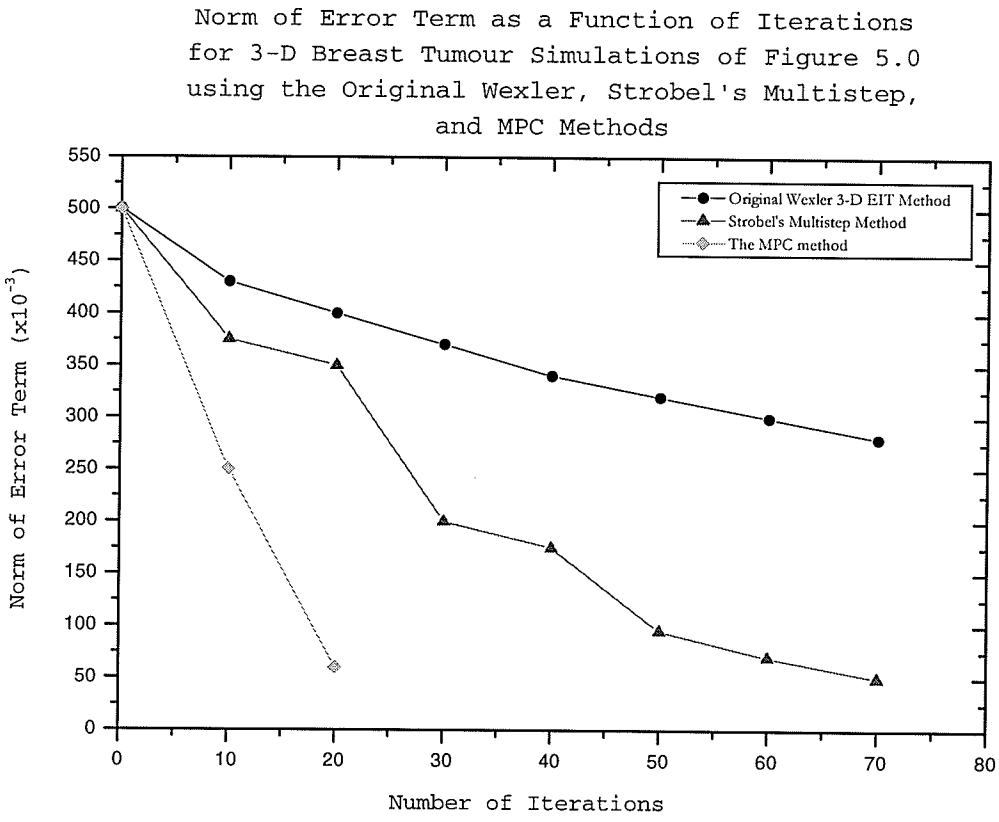

Figure 5.3: Norm of error tern as a function of iterations for setup of Figure 5.0 using the original Wexler 3-D EIT, Strobel's multistep, and MPC methods. Note that the MPC method provides faster convergence than the mutistep or original Wexler 3-D EIT methods. The recovered conductivity distribution at 10 iterations is also shown.

It is obvious from Figure 5.3 that the MPC algorithm succeeds in obtaining fast and quite accurate recovery of the conductivity distribution. Though the image recovered by Strobel's multistep approach [Stro96] is close to that recovered using the MPC scheme, the time to converge (approximately 16.3 minutes) was much longer than the MPC scheme. At 20 iterations, for a time period of 7.4 minutes, on a SUNW, SPARCstation-4, the recovered conductivity distribution, obtained using the MPC algorithm, was determined to be quite close to the exact conductivity distribution. Using the concept of the conductivity profile matching ratio τ ($0 < \tau \leq 1$), introduced in Chapter 4, the τ value for the original, multistep, and MPC methods were determined to be equal to 0.35, 0.78, and 0.82 respectively. The difference between the MPC recovered conductivity distribution to that of the exact distribution was identified to be at the diseased-to-normal tissue interface. Measurement of FWHM's on the recovered image at 20 iterations in the cross-sectional and axial plane were 6.2% and 7.1% of the diameter of the imaging region respectively. These results were an improvement over the original algorithm with FWHMs values of 13.0% and 14.6% in the cross-sectional and axial plane for the central tumour respectively.

5.6 Discussion

Using simulations, the original Wexler 3-D EIT algorithm was identified to be slowly convergent. Method was devised to improve its convergence time. From observations made earlier in Chapter 4, it appears that if the history of potential and conductivity distributions is known, one can predict their distributions at a future time. This observation was at the basis of the Modeller-Predictor-Corrector (MPC) scheme adopted here to improve time of convergence.

In the MPC scheme, the history of potential and conductivity distributions wAS modelled over the second to n iteration period. Although the algorithm is quite stable, the recovered potential and conductivity distributions at the first iteration were not employed in the modelling phase. From experience obtained with the Wexler iterative algorithm, the first iteration was always regarded as the iteration at which the algorithm begins to "settle" down and the iteration at which it is getting ready for a "kick start". Though, as mentioned above, the Levenberg-Marquardt algorithm is very efficient in determining the most appropriate nonlinear fit parameters, sometimes the method converges upon a local minimum, or one or more of the parameter values may tend to infinity. As such, the use of incorrect "fit functions" forms, for further interpretation, would lead to erroneous results. However, in this application of the Levenberg-Marquardt algorithm, the correct "fit functions" were employed as derived carefully in Chapter 4. These were identified experimentally in Chapter 4 to be of type three-parameter exponential and logarithmic functions respectively.

Once modelled, the potential and conductivity relations were used to derive the conductivity distribution at which the algorithm will converge or be relatively close to convergence. To minimize errors that may have propagated as a result of the interpolation operations performed on the relations, in an attempt at deriving the conductivity distribution, the recovered distribution was used to reinitialize the original Wexler algorithm. This ensures that the correct physical approach of the Wexler algorithm is employed.

The result of the simulation performed on the simplified 3-D breast model indicates that the MPC algorithm is quite effective in improving the time of convergence. At 20 iterations, for a time period of 7.4 minutes, the recovered conductivity distribution was determined to be quite similar to the exact conductivity distribution that was being sought. The conductivity profile matching ratio τ ($0 < \tau \leq 1$), for the original, multistep, and MPC methods were determined to be 0.35, 0.78, and 0.82 respectively. As mentioned above, the difference between the MPC recovered conductivity profile to that of the exact distribution was identified to be primarily at the diseased-to-normal tissue interface. Note that this effect, termed the "Tumour-Edge" earlier, was initially identified in Chapter 4.

Measurement of FWHM's on the recovered images at 20 iterations in the cross-sectional and axial plane were 6.2% and 7.1% of the diameter of the imaging region respectively. An obvious improvement over the original algorithm with FWHMs of values 13.0% and 14.6% in the cross-sectional and axial plane respectively.

Despite the major improvement in the time of convergence of the algorithm, using the MPC algorithm, now comparable to existing imaging modalities, the spatial resolution of the recovered conductivity distribution, in particular at diseased-to-normal tissue interface, still requires improvement.

5.7 Summary

The time to convergence of the original Wexler EIT algorithm was demonstrated, using computer simulations, to be relatively inappropriate in the imaging of early breast tumours. The multistep acceleration to convergence as proposed by Strobel, 1996, was identified to be an improvement yet unacceptable in the imaging of breast tumour. A new algorithm - the Modeller-Predictor-Corrector (MPC) - was developed with the objective to drastically improve convergence rate of the original Wexler EIT algorithm.

Results of the 3-D computer simulation appear to indicate that the MPC method is quite effective in improving convergence time. A clinically useful image, showing the tumour, was recovered in 20 iterations. This recovery process took approximately 7.4 minutes on a SUNW[6], SPARCstation-4. However, the resolution, in particular at diseased-to-normal tissue interface, of the recovered image was not of clinical potential. This issue is investigated and addressed fully in the next Chapter.

[6] Sun Microsystems, Inc., 901 San Antonio Road, Palo Alto, CA 94303 USA.

Chapter 6

A Locator-Compensator (LC) Algorithm to Improve Spatial Resolution of the Original Wexler 3-D EIT Algorithm

6.1 Introduction

The transition of EIT from the laboratory to the clinic can only occur if the spatial resolution of the technique improves so as to be comparable to, if not better than, present clinical imaging modalities. Dijkstra *et al.*, 1993, in a review article on EIT, argued that the poor spatial resolution of the technique, which is only about 10% of the diameter of the body, is a major disadvantage in 'static' imaging [Dijk93]. As such, they concluded that the greatest potential clinical application of EIT ought to be in 'dynamic' imaging (e.g., in the monitoring of cardiopulmonary function). Other authors have came to similar conclusions [Camp94, Jong94, Moru96, and Kotr97].

In Chapter 4, Section 4.6, the full-width half-maximum (FWHM, a measure of spatial resolution) of the original Wexler 3-D EIT 'static' imaging algorithm was shown to be approximately 13% in cross-sectional plane, 11%, and 9% of the diameter of the imaging region for a central, intermediate, and peripheral recovered Dirac impulse, respectively. Further, in Chapter 4 the ability to image sharp conductivity changes, e.g., at diseased-to-normal tissue interface, was demonstrated to be relatively poor. Using the MPC algorithm of Chapter 5, it was shown that the spatial resolution at diseased-to-normal tissue interface improved slightly. Here, the focus is on substantially improving the resolution at the sharp edge of the diseased-to-normal tissue.

In an attempt to improve the original Wexler EIT algorithm, Condamines and Marsili, 1994 observed that the algorithm provides good qualitative results but is quantitatively less accurate [Cond96]. Simply stated, the algorithm locates the region(s) of interest (i.e., tumour(s)) at a very low iteration count, irrespective of the size and type (e.g., benign or malignant) of the region(s). However, the recovered conductivity distribution detail, at such early iteration, is somewhat far from what is desired (i.e., what is being sought).

In Chapter 2, it was discussed that for EIT to be of clinical potential and for an accurate diagnosis, a breast lesion ought to be detected at an early stage, physically equivalent to an approximate size of 1-2 mm. Thus, it appears that the spatial resolution that can be obtained with the original Wexler algorithm is not suitable to image small breast tumours. This chapter focuses on improving the algorithm's present limit of spatial resolution and attempts to refine its ability to detect small breast lesions. A novel algorithm, termed the Locator-Compensator (LC) algorithm, is developed and implemented on realistic 3-D computer simulations of small breast tumour imaging. Results of simulations are discussed and summarized.

6.2 Spatial Resolution of the Original Wexler 3-D EIT Algorithm

For the purpose of this section, the simplified 3-D model of the breast adopted for Chapter 5, Section 5.5 is employed. The focus here is on investigating the spatial resolution of the original Wexler 3-D EIT algorithm rather than on its convergence rate discussed was in Chapter 5. The region to be imaged (i.e., a cube) is divided into 15625 (i.e., 25×25×25) finite volumetric elements (i.e., voxels), with a central voxel representing the tumour (see Figure 6.0). The tumour element is spatially located at the coordinates (x=13, y=13, and z=13). Two hundred and twenty electrodes were arranged over the 3-D object surface and one hundred and ten injections/extractions views were employed to reconstruct the 3-D images. This corresponds to a determinacy of 1.15 using the '*sometimes*' measurement pattern. The voxel representing

the tumour has a conductivity of 4.0 and is within a background region of conductivity value 1.0. Measurements are taken on five sides of the cube. The remaining side represents the side of the breast that is attached to the chest wall.

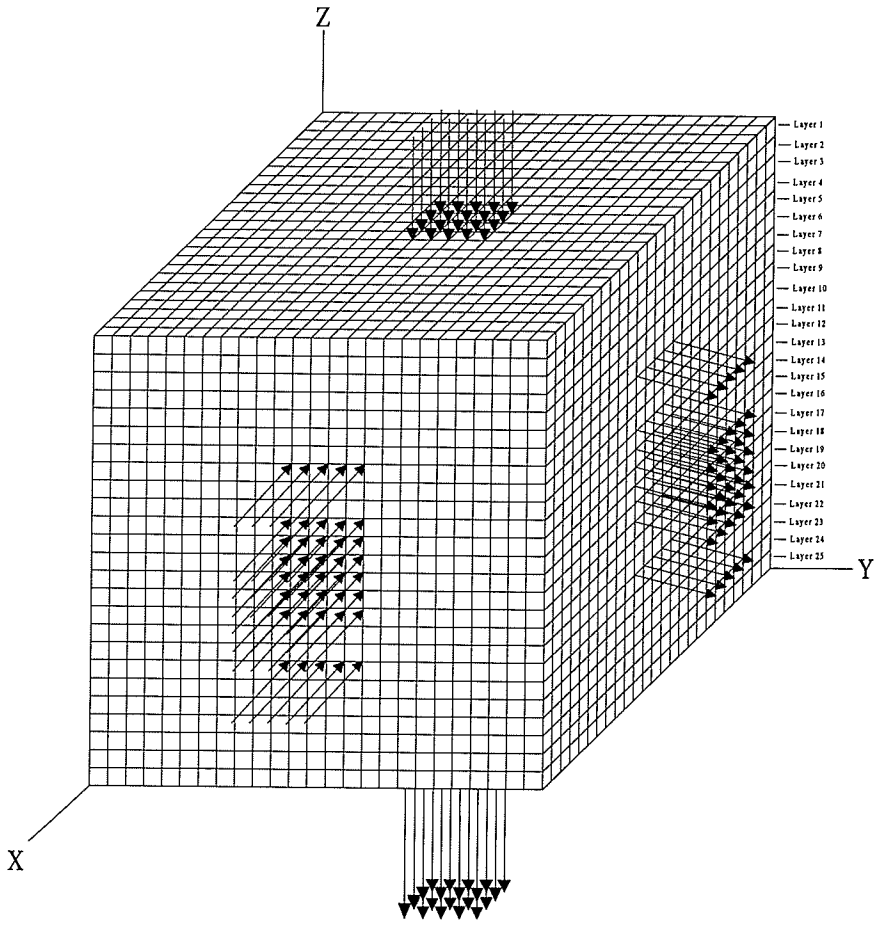

Figure 6.0: A simplified 3-D breast model for simulation of Section 6.2. Volume has 15625 elements. One hundred and ten excitation pairs were employed. The tumour element is located on Layer 13, with coordinates (x=13,y=13, and z=13). Though not fully realistic, this simplified model provides a mean to investigate the limit of spatial resolution of EIT breast cancer imaging

Figure 6.1 below shows the recovered images of layers 11, 12, 13, 14, and 15 for the central tumour voxel of Figure 6.0. The spatial resolution (or the FWHMs) in the cross sectional and axial planes for the recovered image of the tumour voxel are approximately 12.6% and 13.8% of the diameter of the imaging region.

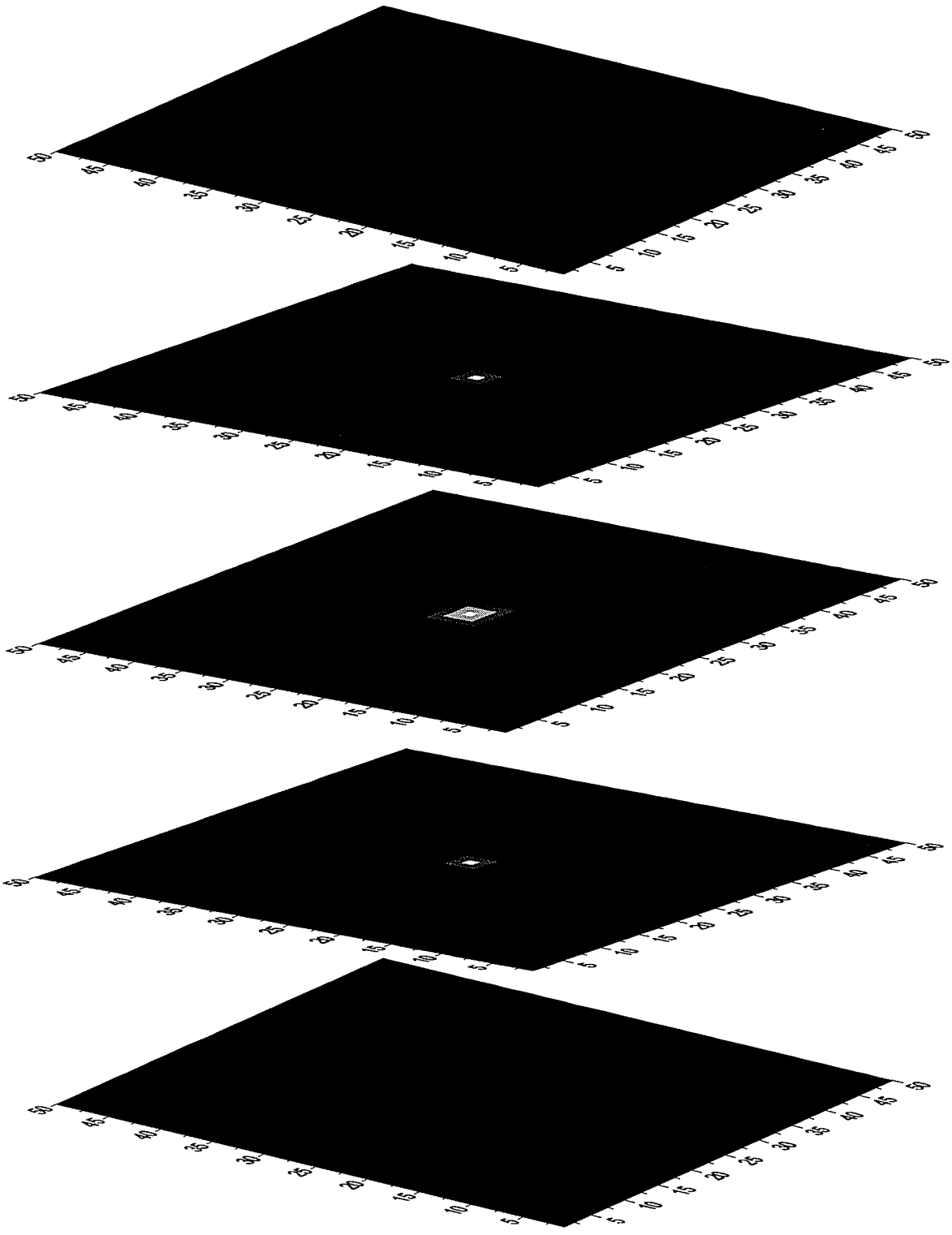

Figure 6.1: Recovered images of layers 11, 12, 13, 14, and 15 (from top) using the original Wexler 3-D EIT algorithm at 50 iterations. The FWHMs (or spatial resolution) in the cross-sectional and axial planes for the tumour voxel are approximately 12.6% and 13.8% of the diameter of the imaging region. Note that to accommodate for gray scaling, the elements had to be double in size. In reality, there are 25×25 elements on the 2-D image shown above.

6.3 EIT's Limit of Spatial Resolution: A Discussion

The quality of an impedance imaging system is directly and closely related to the image it can provide, and therefore to the reconstruction algorithm, that it is to say, the stability of the algorithm, reconstruction time, precision of the reconstructed image, computing complexity, etc. [Moru96]. There are a number of ways one can try to improve resolution. One way is by incorporating a priori knowledge of the location of various tissues and the range of corresponding impedances [Avis95, Mees95, and Bays98]. It appears that correct a priori information is usually not readily available, for example the conductivity values within most anatomical regions are not known [Dehg99]. However, with recent developments in 'EIT spectroscopy', impedance mapping of anatomical structures and organs contribute to the knowledge of tissue characterization [Brow95].

Some authors have argued that in order to obtain high resolution with EIT, high precision impedance measurements are needed since the image reconstruction process is ill-conditioned and small errors in measurement can lead to large errors in the final image [Barb 95 and Boon96]. Maybe this is so for 'dynamic' imaging-based algorithms. However, for iterative algorithms, e.g., the Wexler EIT image reconstruction method, ill-conditioning is generally not much of a limitation as has been demonstrated here.

With respect to EIT hardware, as seen in the literature, the general notion is that formidable instrumentation problems exist, due mainly to the interaction of finite current drive output impedance, recording amplifier common mode rejection, and unequal skin-electrode impedances [Boon97]. Consequently, the spatial resolution of EIT would be limited. However, many of the instrumentation problems that were once considered troublesome have now been overcome [Boon97]. Some have employed strategies like using additional electrodes, multiple electrode current injection, or recording at multiple frequencies, to improve image accuracy.

From simulations performed here and a review of literature, it appears that the major difficulties with iterative-based 'static' imaging algorithms are convergence problems (directly related to the guess made at initial conditions), noise and an accurate model of the physical system being imaged [Riga96]. Despite these hurdles, EIT reconstruction methods that are based on an iterative algorithmic approach generally provide higher image quality than direct methods [York88 and Shah95].

A few interesting observations on spatial resolution of EIT can be found in the literature. In particular, Kotre, 1997 remarked that the spatial resolution of a 'static' recovered EIT image is low and observed that it is worst towards the center of the image [Kotr97]. Ider *et al.*, 1995, using an iterative backprojection algorithm, showed that the full-width half-maximum (FWHM), of 2-D single-object perturbations for central, intermediate, and peripheral high-contrast objects are 27%, 18% and 14% of the imaging region diameter respectively [Ider95]. Similar observations were made for the original Wexler EIT algorithm. It was further demonstrated that the resolution at normal-to-diseased tissue interface was relatively poor.

To be of potential in the imaging of small breast tumour, the spatial resolution of the Wexler 3-D EIT algorithm ought to be comparable to existing high-resolution techniques (e.g. MRI or CT, which typically go down to $1mm^3$ voxels) [Harm98]. The overall resolution and, in particular, the spatial resolution at normal-to-diseased tissue interface would need to be improved. As shown in Chapter 4, the higher conductivity magnitude of the tumour element/voxel has an undesired effect on the surrounding normal element(s). This, in turn, contributes to the deterioration of image quality at sharp edges. The Locator-Compensator method described here mainly addresses the issue of improving the lower spatial resolution at sharp edges.

6.4 The Peak Detection Image Processing Algorithm

Though it is known in the literature [Hua91 and Ider95], and demonstrated in Chapter 4, that the spatial resolution of EIT decreases from the periphery to the central portion of the image (i.e., is space variant), no published work on compensating for the loss in spatial resolution exists. The loss in spatial resolution is a characteristic of the flow of electrical current through a heterogeneous medium as governed by Poisson's equation (i.e., the physics of electrical current flow). However, as has been pointed out by many investigators, it is imperative that the imaging process in EIT incorporates the solution of the electric field equations [Tast81 and Pric79].

How to improve EIT's spatial resolution? In the case of the Wexler EIT algorithm, it was concluded in Chapter 5 that the algorithm locates disturbance(s) at early iterations. However, quantitatively the resolution of the recovered disturbance(s) at such early iterations are far from what is desired. An obvious approach, in this case, would be to apply some sort of quantitative resolution compensation to the localized region(s). By compensating for loss in resolution as a function of location of region(s) of interest (i.e., at normal-to-diseased tissue interface), an increase in the spatial resolution would be anticipated. In other words, the characteristic EIT spatial resolution would, in theory, be shifted from space variant to space invariant.

How to locate these region(s) of interest and how best to apply the resolution compensation? In her Ph.D. dissertation, Mu, 1994 discussed an approach that combines an image processing technique, the peak detection method, to locate the region(s) or peak(s) of interest with a modified conductivity distribution-updating scheme [Mu94]. Although, Mu's method was correct, the results of its implementation on the Wexler EIT algorithm were not appropriately effective in increasing spatial resolution, in particular at normal-to-diseased tissue interface, where

no drastic improvements were noticeable. The method and implementation of Mu's approach is discussed in more detail in the next section.

The peak detection algorithm is an image processing technique that selectively detects peak(s) in the image histogram. It does so by generating a peak detection signal from an image histogram [Seza89]. Using the difference between the local maxima and the zero-crossings of the detection signal, histogram peaks are then located. Peak detection algorithms have been used successfully in selective post-enhancement of digital anatomical images [Seza89]. Mu, 1994, demonstrated its usefulness in improving spatial resolution when applied at the pre-recovery stage of conductivity distributions using the original Wexler EIT algorithm [Mu94].

The peak detection method as implemented by Mu, 1994, in an attempt to improve convergence rate and subsequently spatial resolution, is summarized in the following steps:

Step 1: The Wexler algorithm, with its initial conductivity-updating scheme (see Chapter 3, Section 3.1) is applied to the imaging region for n^{th} iteration.

Step 2: At the n^{th} iteration, the element conductivity difference $(\kappa_n - \kappa_b = \Delta\kappa_n)$ is determined and saved accordingly for the whole imaging region. Where κ_n is the conductivity distribution of the whole region at the n^{th} iteration and κ_b is the background conductivity distribution respectively.

Step 3: Peak(s) within the imaging region is/are then located by finding the local maximal conductivity changes. To avoid detecting any unwanted anomalies induced by numerical errors via discretization, a filtering scheme is applied prior to peak(s) detection. The criterion for peak(s) detection is simply to compare $(\Delta\kappa_n)$ with a subjective preset value of some fraction of the background conductivity $(*\kappa_b)$. If $(\Delta\kappa)$ exceeds the preset value $(*\kappa_b)$, then a modification to the updating-scheme is applied to the local region of the

peak(s). Mathematically, if the neighborhood within a localized peak region, κ_{ln}, with central peak element conductivity, κ_P, exceeds $*\kappa_b$, then elements within the localized region, κ_{ln}, are replaced at the (n^{th} + 1) iteration by,

$$\kappa_{n+1} = \kappa_{ln} + \omega \Delta\kappa_n \qquad [6.0]$$

where $\Delta\kappa_n$ is the difference in conductivity for elements within the localized region as defined earlier, and ω is the convergence acceleration factor as discussed in Appendix II.

Step 4: This process is repeated over the whole imaging region until there are acceptable errors between calculated and measured conductivity distributions.

The peak detection method, implemented by Mu, 1994, works well in situations where correct preset values are assumed. If a guess at a preset value is relatively lower than the conductivity difference ($\Delta\kappa$), the recovered overall resolution is not appropriate for imaging small breast tumours. In particular, resolution at diseased-to-normal tissue interface does not improve substantially. Since a user-determined preset value is required, the applicability of this approach is greatly reduced. Further, once the peak(s) is/are located, an incorrect choice of the convergence acceleration factor, ω can subsequently affect its stability [Pres86].

6.5 The Locator-Compensater (LC) Algorithm

Despite the selective peak(s) localization approach adopted by Mu, 1994, in attempting to improve spatial resolution, only tumours of physical size >30 mm in diameter could be resolved. At such size, the metastatic probability is substantially high. As discussed earlier, ideal detection size would be within the range of 1-2 mm. Can the original Wexler EIT image reconstruction algorithm be improved to resolve tumours of size <4mm? A novel scheme, the Locator-Compensator (LC) method, developed here appears to do just that!

The Locator-Compensator (LC) algorithm is a combination of a variant of the peak detection method described above and a new resolution compensation scheme. The Locator-Compensator method is discussed in more detail in the next paragraph. In brief, the peak detection variant method is used to locate the spatial coordinates of the peak(s) at early iterations. Location of peaks is done in a much different manner than described previously. Once the coordinates of the peak(s) are localized, then the resolution (i.e., in terms of conductivity magnitude of the peak(s)), are compensated for. The compensation is performed by applying the original Wexler EIT conductivity- updating scheme over the localized regions rather than over the whole imaging region.

In this implementation of the peak detection method, rather than having to assume a percent of the background conductivity (i.e., $*\kappa_b$), which subsequently is used as the basis for the criterion for peak detection (i.e., by comparing $*\kappa_b$ to $\Delta\kappa$), the variant of the peak detection method employs a non-subjective approach for peak(s) localization (Figure 6.2). The Wexler algorithm with its original conductivity updating-scheme is used to sweep through an imaging region for n iterations. The recovered conductivity distribution at each iteration (i.e., $\kappa_1, \kappa_2, \kappa_3, ..., \kappa_n$) is averaged over n iterations (i.e., $\kappa_1 + \kappa_2 + \kappa_3 + ... + \kappa_n / n$). The averaged conductivity distribution at n iterations (i.e., $\overline{\kappa}_n$) is then averaged over all the elements

within the imaging region. This results in an average conductivity per element ($\overline{\kappa}_{en} = \overline{\kappa}_n / N$), N being the total number of elements in the adopted mesh for image recovery (or solution of the inverse problem). Peaks are located by comparing $\overline{\kappa}_{en}$ to κ_{en+1}, where κ_{en+1}, is the conductivity of each element at n+1 iteration (Figure 6.2). If $\kappa_{en+1} > \overline{\kappa}_{en}$, the element or an aggregate of elements is/are identified as peak(s) or if $\kappa_{en+1} \leq \overline{\kappa}_{en}$, then the element or an aggregate of elements is/are not regarded as peak(s). To avoid detecting any unwanted anomalies due to truncation or discretization, a filtering scheme is applied prior to peak(s) detection. Once element(s) is/are identified as peak(s), the spatial coordinates of the immediate elements surrounding the peak(s) element(s) are identified. It is at these coordinates that the new conductivity distribution updating-scheme is implemented to compensate for loss in spatial resolution.

Once identified, the calculated potentials at coordinates of identified element(s) are then substituted by the interpolated interior potentials obtained from measured or known surface potentials. The interpolated potentials applied to the surrounding elements node of the peak(s) element(s) caused the interior potentials (i.e., potentials at nodes within the localized region(s)) to be nudged in the correct direction (i.e., toward minimization of the differences between the measured and the calculated potentials). Since the localized region(s) would generally consist(s) of a few elements (i.e., pixels or voxels), this selective conductivity-updating scheme is relatively fast and effective. While conductivity in the localized region is updated with the localized updating scheme just described, conductivity update for the rest of the imaging region proceeds via the original Wexler EIT conductivity-updating scheme. This process continues until measured and calculated potentials are equal (i.e., until convergence is attained).

The Locator-Compensator algorithm is summarized in the following steps:

Step 1. Run Wexler Algorithm for *n* Iterations

The original Wexler EIT algorithm, with its conductivity updating scheme as described in Chapter 3, Section 3.1 (see Figure 3.1), is used to sweep through the imaging region (see Equation 3.6) for n iterations. In brief, the revised estimate of conductivity within element i over all node points and over all excitations is,

$$\kappa_i = \frac{-\sum_X \iiint_{V_i} \bar{J} \cdot \nabla\phi \, dv}{\sum_X \iiint_{V_i} \nabla\phi \cdot \nabla\phi \, dv} \qquad [6.1]$$

where $\bar{J}$ is the estimated electrical current density distribution, ϕ is the potential obtained with Dirichlet boundary conditions, κ_i is a revised estimate of the conductivity within element i, v_i is the volume of the element i, and X represents the excitations over which the sum is taken.

Step 2. Save Conductivity Distribution (κ) over 1 to *n* Iterations

The recovered conductivity distribution over the period of iteration 1 to n is saved and averaged over n iterations, $\bar{\kappa}_n$. The average conductivity distribution $\bar{\kappa}_n$ is then averaged over all the elements, $\bar{\kappa}_{en} = \bar{\kappa}_n / M$. The average over all elements $\bar{\kappa}_{en}$ is then used as a criterion component for peak detection.

Step 3. Locate Peak(s) with the Peak Detection Variant Method at *n*+1 Iterations

Peak(s) is/are located by comparing $\bar{\kappa}_{en}$ to κ_{en+1}, where κ_{en+1} is the conductivity of each element at n+1 iteration. If $\kappa_{en+1} > \bar{\kappa}_{en}$, the element or an aggregate of elements is/are identified as peak(s) or if $\kappa_{en+1} \leq \bar{\kappa}_{en}$, then the element or an aggregate of elements is/are not regarded as peak(s). To avoid detecting any unwanted anomalies due to truncation or discretization, a filtering scheme is applied

prior to peak(s) detection. Once the peak(s) is/are located, the immediately surrounding elements nodes spatial coordinates are identified. The potentials at these nodes are saved accordingly.

Step 4. Compensate for Resolution at (n+2) to N Iterations

When viewed as a whole, the imaging region can be considered to consist of localized peak(s) region and a background region. The conductivity updating-scheme for the background region is that as utilized by the original Wexler algorithm, described mathematically by relation [6.1] above. The new conductivity updating scheme for the localized region(s) can be arrived at by applying the original Wexler conductivity updating scheme to the identified region(s) in much the same way as described in Chapter 3, Section 3.1. In this new approach, the calculated potentials at the spatial coordinates of the external nodes of the elements identified in Step 3 are substituted by the interpolated calculated potentials obtained from the measured or known surface potentials. That is to say, applying Dirichlet boundary conditions to the localized regions while leaving the remaining initial (i.e., at n +1 iterations) Neumann boundary conditions unchanged. This causes the interior potentials to be nudged in the correct direction. This is performed for each iteration and over the whole imaging region iteratively until convergence at iteration N. Similarly, the Dirichlet boundary condition for the localized region(s) is,

$$\varphi(ls) = g(ls) \qquad [6.2]$$

which corresponds to the interpolated calculated potentials at external nodes coordinates of element(s) identified in Step 3. In addition, the boundary conditions must include the Neumann conditions at current-injection sites as described in Chapter 3.

By following a similar derivation process as in Chapter 3, the revised estimate of conductivity within element l over the volumetric region enclosed by the identified node points coordinates and over all excitations is given as,

$$\kappa_l = \frac{-\sum_X \iiint_{V_l} \bar{J} \cdot \nabla \phi_l \, dv}{\sum_X \iiint_{V_l} \nabla \phi_l \cdot \nabla \phi_l \, dv} \qquad [6.3]$$

where $\bar{J}$ is the estimated electrical current density distribution, ϕ_l is the interpolated calculated potential obtained from the measured or known surface potentials (i.e., from application of Dirichlet boundary conditions), κ_l is a revised estimate of the conductivity within element l of the localized region, v_l is the volume of the element l, and X represents the excitations over which the sum is taken.

By combining equations 6.2 and 6.3, a new conductivity-updating scheme is obtained (6.4). This revised scheme is applied to each element in turn to update the conductivity distribution over the entire region within which the imaging is being performed.

$$\kappa_{i+l} = \frac{-\sum_X \iiint_{V_i} \bar{J} \cdot \nabla \phi \, dv}{\sum_X \iiint_{V_i} \nabla \phi \cdot \nabla \phi \, dv} + \frac{-\sum_X \iiint_{V_l} \bar{J} \cdot \nabla \phi_l \, dv}{\sum_X \iiint_{V_l} \nabla \phi_l \cdot \nabla \phi_l \, dv} \qquad [6.4]$$

The Locator-Compensator algorithm makes use of the combined updating scheme [6.4] to recover the conductivity distribution. Characteristically, the fact that the original Wexler algorithm locates the peak(s) at early iteration, application of the LC algorithm, will in theory, ensure that the peak(s) converge(s) much faster and with adequate resolution at diseased-to-normal tissue interface. In the next section, the Locator-Compensator (LC) method scheme is tested by performing computer simulations.

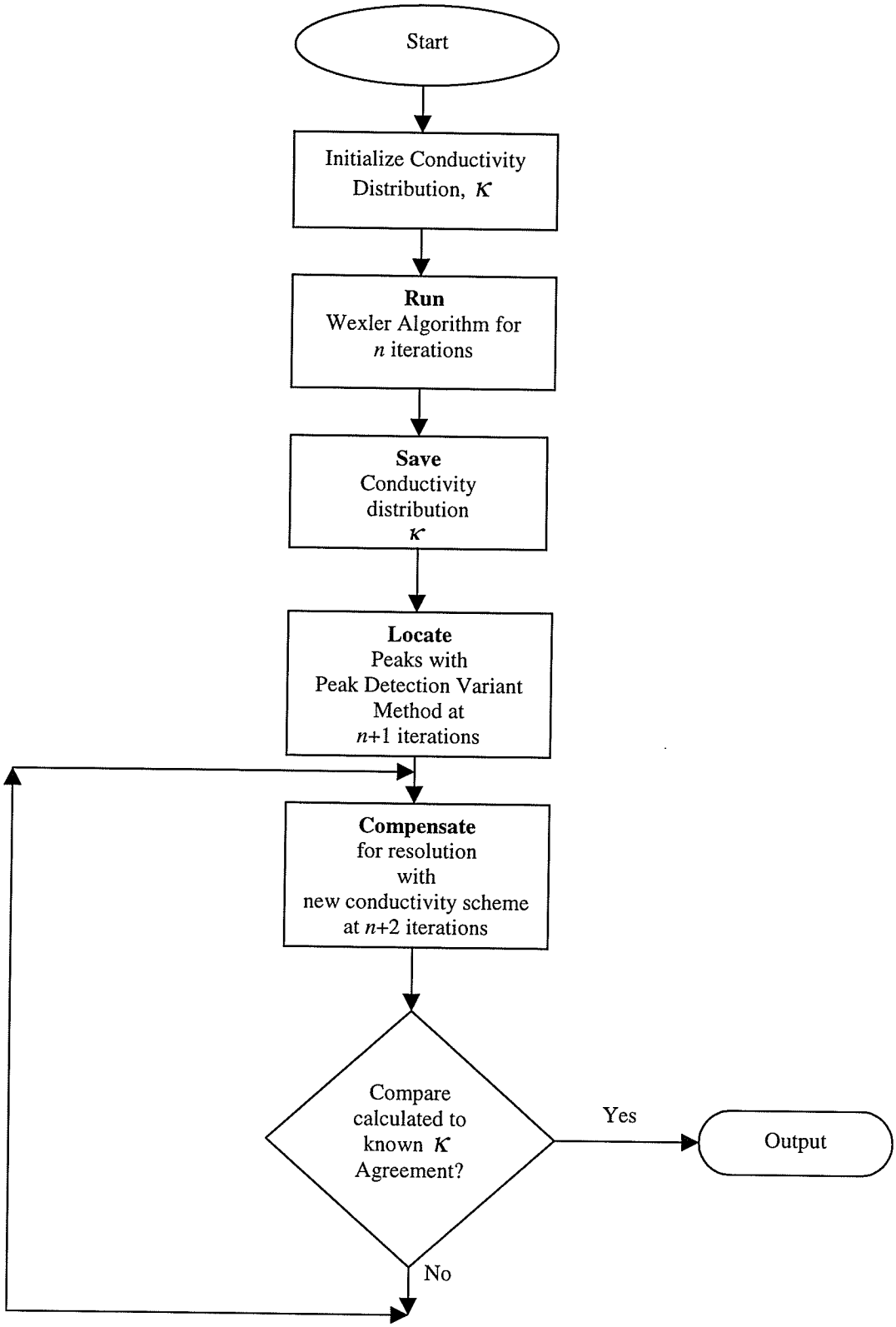

Figure 6.2: The Locator-Compensator (LC) flow chart. The algorithm is initialized using an assumed conductivity distribution. The original Wexler 3-D EIT is allowed to run for n iterations. The algorithm then proceeds to the Save, Locate, and Compensate steps. A comparison is then made to the known conductivity distribution, if results agree then the algorithm outputs. If not, the algorithm keeps iterating through the Compensation step until convergence.

6.6 3-D Computer Simulations using the LC Algorithm

To demonstrate the effectiveness of the Locator-Compensator (LC) scheme in improving spatial resolution, in particular at diseased-to-normal tissue interface, the previous 3-D simulation of small breast tumour imaging described in Section 6.2 and Figure 6.0 above is repeated here. The original Wexler 3-D EIT algorithm is run for a period of 15 iterations. The recovered conductivity distributions over that time interval are averaged. The averaged distribution is then subsequently average over all the elements. This is saved accordingly and the original Wexler algorithm is allowed to run for one more iteration. At the 16th iteration, the average conductivity per element is then used as a criterion to locate peaks. Once localized, the peak conductivities are then compensated for at the 17th iteration by the combined conductivity-updating scheme described above. Figure 6.3 below shows the recovered images of layers 11, 12, 13, 14, and 15 for the central tumour voxel of Figure 6.0 using the LC algorithm at 50 iterations. The spatial resolution (or the FWHMs) in the cross sectional and axial planes for the recovered image of the tumour voxel are approximately 5.4% and 6.3% of the diameter of the imaging region.

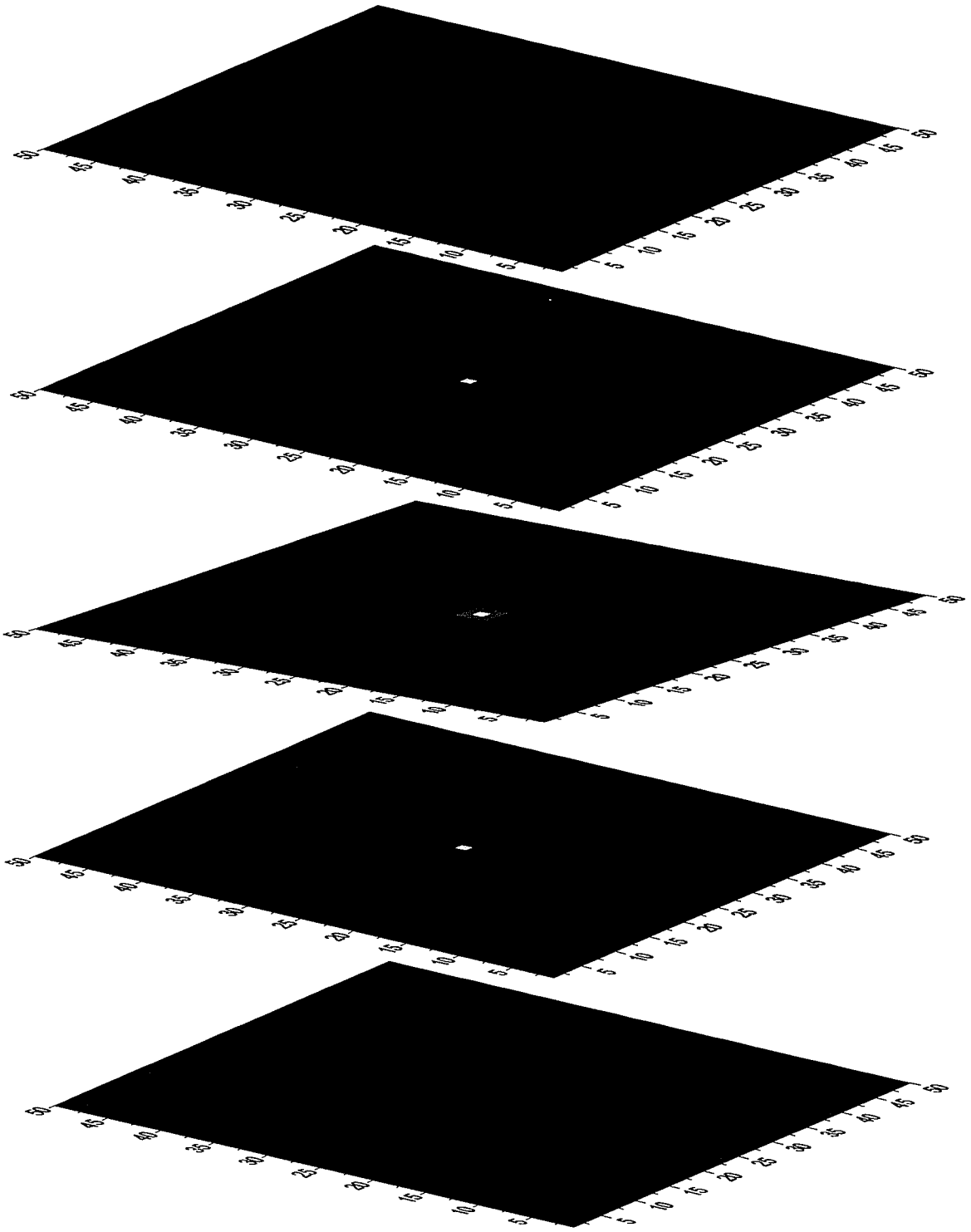

Figure 6.3: Recovered images of layers 11, 12, 13, 14, and 15 (from top) using the LC algorithm. The FWHMs (or spatial resolution) in the cross-sectional and axial planes for the tumour voxel are approximately 5.4% and 6.3% of the diameter of the imaging region. Images were recovered at 50 iterations. Note that to accommodate for gray scaling, the elements had to be double in size. In reality, there are 25×25 elements on the 2-D image shown above.

6.7 Discussion

Using simulations, the original Wexler 3-D EIT algorithm was identified to have low resolution. From observations made earlier in Chapter 4, it appears that the "Tumour-Edge" effect is responsible for the observed low resolution at the edges. As such, the Locator-Compensator (LC) method was developed to improve the overall spatial resolution.

In brief, the LC method involved locating the peaks with a variant of the peak detection image processing algorithm and subsequently applying a new conductivity-updating scheme. This combination appeared to improve resolution at diseased-to-normal tissue interface. Measurement of FWHM's on the recovered images at 50 iterations in the cross-sectional and axial plane were 5.4% and 6.3% of the diameter of the imaging region respectively. These results were an improvement over the original algorithm with FWHMs of values 13.0% and 14.6% in the cross-sectional and axial plane respectively.

It should be noted that the recovered image resolution obtained from the LC algorithm is higher than that obtained with the Modeller-Predictor-Corrector (MPC). The resolution for the MPC in the cross-sectional and axial planes was 6.2% and 7.1% respectively. Though, the resolution of the LC method is superior to that of the MPC, the LC takes much longer to converge. The MPC converged in 20 iterations while the LC converged in 50 iterations for the same computer simulation setup. If combined, one anticipates that the MPC would help to improve convergence rate and the LC method would improve resolution, in particular, at diseased-to-normal tissue interface. This observation is further investigated in Chapter 7.

6.8 Summary

The spatial resolution of the original Wexler EIT imaging algorithm was demonstrated to be relatively low, compared to other clinical imaging modalities. The spatial resolution was identified to be space variant. The Locator-Compensator (LC) algorithm was developed to compensate for the loss in spatial resolution at diseased-to-normal tissue interface. Improvements were demonstrated on simplified 3-D computer simulations of early breast tumour imaging. It was shown that the LC method could resolve approximately 5.4 % and 6.3% of the diameter of the imaging region.

Chapter 7

An Improved Wexler EIT Algorithm for 3-D Breast Cancer Imaging

7.1 Introduction

It is generally assumed, though incorrectly, that the flow of electrical current is restricted to the 2-D-measurement plane while current flowing elsewhere through the medium is negligible [Meth96]. This gross over-simplification has limited the capability of EIT, as it is intuitively clear that there exists a three dimensional variation of conductivity distribution within the 3-D object [Liu88]. Consequently, image reconstruction via 2-D voltage distributions throughout a 3-D object can lead to severe image distortions. In Chapter 4, it was shown that significant advantages might be achieved by extending EIT to 3-D, in particular, an increase in the size of the independent data set for image reconstruction and an improved spatial resolution of the derived images. To date only a few articles have addressed and contributed to the understanding of 3-D EIT.

Using a new electrode arrangement scheme along with the Newton-Raphson algorithm, Liu *et al.*, 1988 obtained good resistivity images of a 3-D object [Liu88]. Kuzuoglu *et al.*, 1992, demonstrated the effect of the three dimensional variation of conductivity distribution in 3-D EIT using FEM and the frontal algorithm of Irons for matrix inversion [Kuzu92]. Metherall *et al.*, 1996, using a previously developed EIT system and an inverse-matrix based algorithm, demonstrated the practical potential of 3-D EIT in clinical applications of lung or brain imaging [Meth96]. A three-dimensional image reconstruction algorithm for EIT, based on the inversion of the sensitivity matrix for a finite right circular cylinder, was derived by Kleinermann *et*

al., 1996 [Klei96]. The authors showed that the 3-D algorithm recruits more central information than the two-dimensional image reconstruction algorithm. And recently, Glidewell *et al.*, 1997, from simulation results demonstrated and emphasized the importance of tissue anisotropy in 3-D EIT [Glid97].

In this chapter, the inevitable questions raised in Chapter 1 are addressed. Could an improved Wexler 3-D EIT algorithm be used to image (viz., detect and diagnose) breast tumours? Could it be used to detect breast cancer before the onset of metastatic spread i.e., at physical size of 1-2 mm in diameter? An attempt is provided here, using an improved algorithm obtained by combining the development of the two previous chapters, in particular, the Modeller-Predictor-Corrector (MPC) scheme to improve convergence speed and the Locator-Compensator (LC) algorithm to improve overall spatial resolution. The potential of the improved 3-D Wexler EIT algorithm is demonstrated through realistic (i.e., pertinent to clinical situation) computer simulations imaging of small breast tumours (viz., benign and malignant). Results are presented and discussed.

7.2 An Improved and Refined Wexler 3-D EIT Algorithm

In Chapter 4, through computer simulations, it was demonstrated that the convergence rate of the original Wexler 3-D EIT algorithm would need to be improved drastically. This was achieved in Chapter 5 by using a new and efficient scheme, the Modeller-Predictor-Corrector (MPC) algorithm. The efficiency of the MPC scheme was demonstrated on 3-D computer simulations of small breast tumour imaging. With an improved convergence rate, a subsequent improvement in overall resolution was also observed. However, it was observed that resolution at diseased-to-normal tissue was not of optimal level for the imaging of small breast tumours.

An algorithm (i.e., the Locator-Compensator, LC) that carefully locates region(s) of interest and updates the region(s) conductivity with a combined conductivity-updating scheme was developed in Chapter 6. It was shown, using simulations that if the Locator-Compensator (LC) algorithm is appropriately implemented, a substantial increase in overall resolution, and in particular, at diseased-to-normal tissue, could be achieved.

On the basis of the previous discussion, it is anticipated that an improved (i.e., fast and accurate) Wexler EIT image reconstruction algorithm, capable of producing radiologically useful 3-D conductivity images, could be used to image (viz., detect and diagnose) small breast tumours. This feat could be accomplished by combining the development of the last two chapters (i.e., Chapters 5 and 6) with optimal parameters, identified while investigating the characteristics and 'dynamics' of the original Wexler EIT algorithm, of Chapter 4.

The flow chart of the improved Wexler EIT algorithm is shown in Figure 7.0 below. In this combined approach of the improved algorithm, the conductivity κ and potential ϕ are first initialized. The original Wexler 3-D EIT algorithm is then used to sweep through an imaging region for n iterations. Thereafter, the MPC algorithm is used to model the past behaviour of potential and conductivity distributions. From the modeled potential and conductivity relations, a conductivity

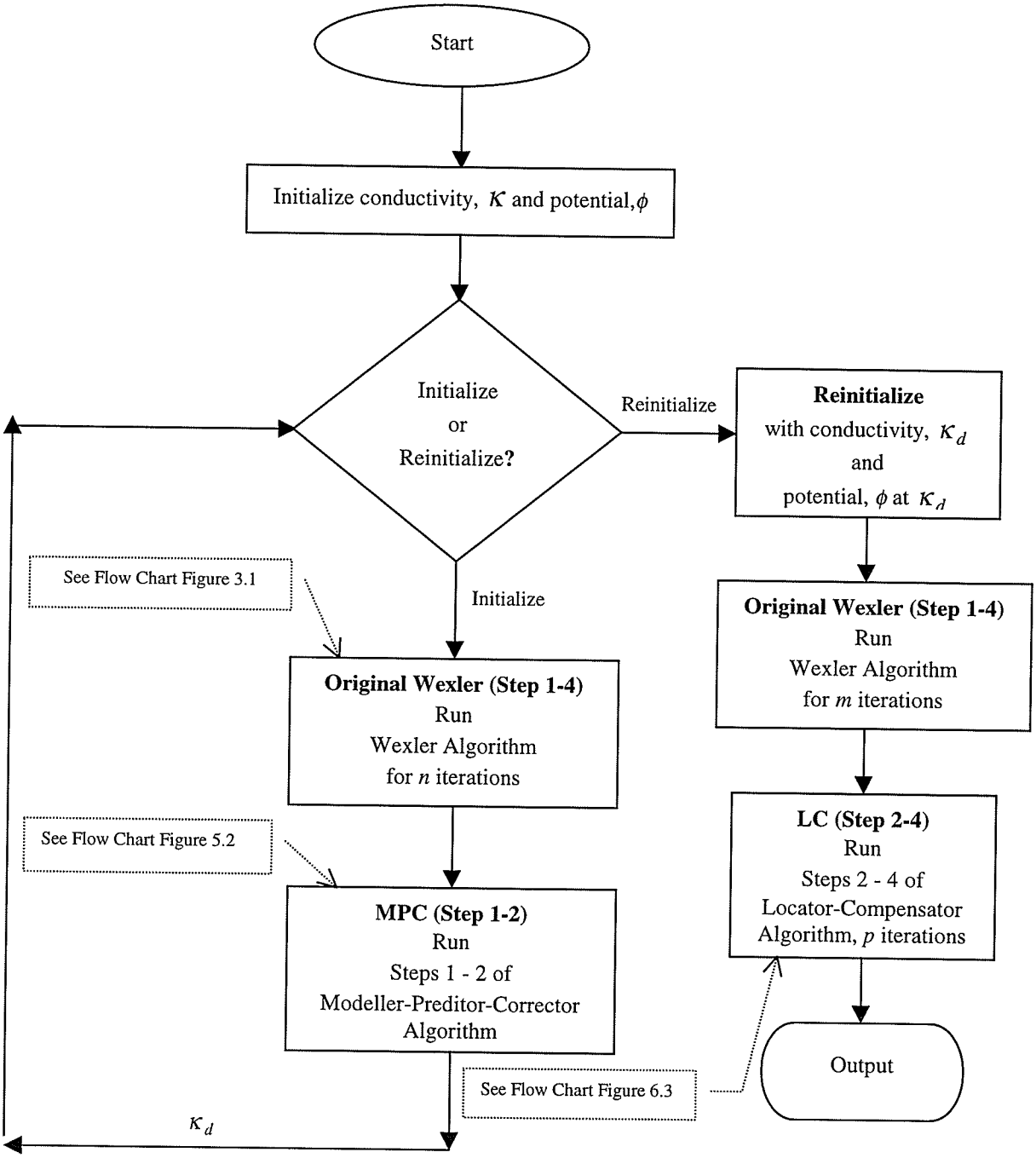

Figure 7.0: The improved Wexler EIT algorithm flow chart. The algorithm is initialized for k and ϕ. The algorithm then proceeds to the MPC algorithm. This outputs a derived conductivity, which is then employed in the LC algorithm. If the resulted conductivity is equal to the measured conductivity, the algorithm outputs the image. The improved algorithm runs for approximately c $(c = n + m + p)$ iterations.

distribution κ_d is derived that is assumed to be close to the conductivity distribution being sought (i.e., at convergence). The extrapolated conductivitity, κ_d is then used to reintialize the original Wexler 3-D EIT algorithm. The MPC is applied for over m iterations. Subsequently, the LC algorithm is applied to the derived conductivity distribution κ_d for a period of p iterations. The LC algorithm localizes peak(s) and updates conductivity appropriately. This process continues until the calculated value is equal to the measured potential. The algorithm then outputs the recovered image in a considerably faster time and at higher spatial resolution.

In summary the improved algorithm proceeds as follows (Figure 7.0):

Step 1: Run Original Wexler 3-D EIT Algorithm for n Iterations.

The original Wexler EIT algorithm, with its conductivity updating scheme as described in Chapter 3, Section 3.1 (see Figure 3.1), is used to sweep through the imaging region (see Equation 3.6) for n iterations.

Step 2: Run the MPC Algorithm for m Iterations.

From the history of the recovered potential and conductivity distributions of Step 1, the MPC algorithm is applied to model, predict, and correct for a derived conductivity distribution, κ_d. As discussed earlier, the correction is performed using the original Wexler algorithm and this is performed for m iterations.

Step 3: Run the LC Algorithm for p Iterations.

Following Step 2, the Locator-Compensator (LC) algorithm is applied. This localizes the peaks and the revised conductivity distribution scheme is applied subsequently to update the conductivity appropriately (i.e., for localized and background region). The LC algorithm is applied over p iterations. This process continues until the calculated is equal to measured potential (i.e., until convergence). The algorithm then outputs the recovered conductivity image. The whole process takes approximately c ($c = n + m + p$) iterations to converge.

7.3 The Original Wexler 3-D EIT Algorithm: A Realistic 3-D Simulation

The Wexler 3-D EIT algorithm was thoroughly discussed in Chapter 3 and a few tests and effects on the algorithms were performed in Chapter 4. For the purpose of this section, a more realistic 3-D simulation that is representative of small breast tumour imaging is performed here (Figure 7.1). As in Chapter 3, the breast is physically represented as a cube. The 3-D cube is divided into 50×50×50 (i.e., for a total of 125,000 elements or voxels). The central voxel representing the malignant tumour (conductivity equal to 4.0) is spatially located on the 25th layer at coordinates of (x=25, y=25, and x=25). The intermediate voxel representing the benign tumour is located on the 25th layer at coordinates of (x=13, y=13, and z=25) respectively. Three hundred excitation pairs were employed to recover the 3-D images, this corresponds to a determinacy of approximately 1.08, a slightly over-determined problem. Measurements are made on five sides of the breast model region, and no measurements were made to the side that is attached to the chest wall. To render the simulation as close to the realistic situation (i.e., conditions prevalent in a clinical situation), a SNR level of 30 dB was added to the simulation. This was intended to simulate instrumentation noise.

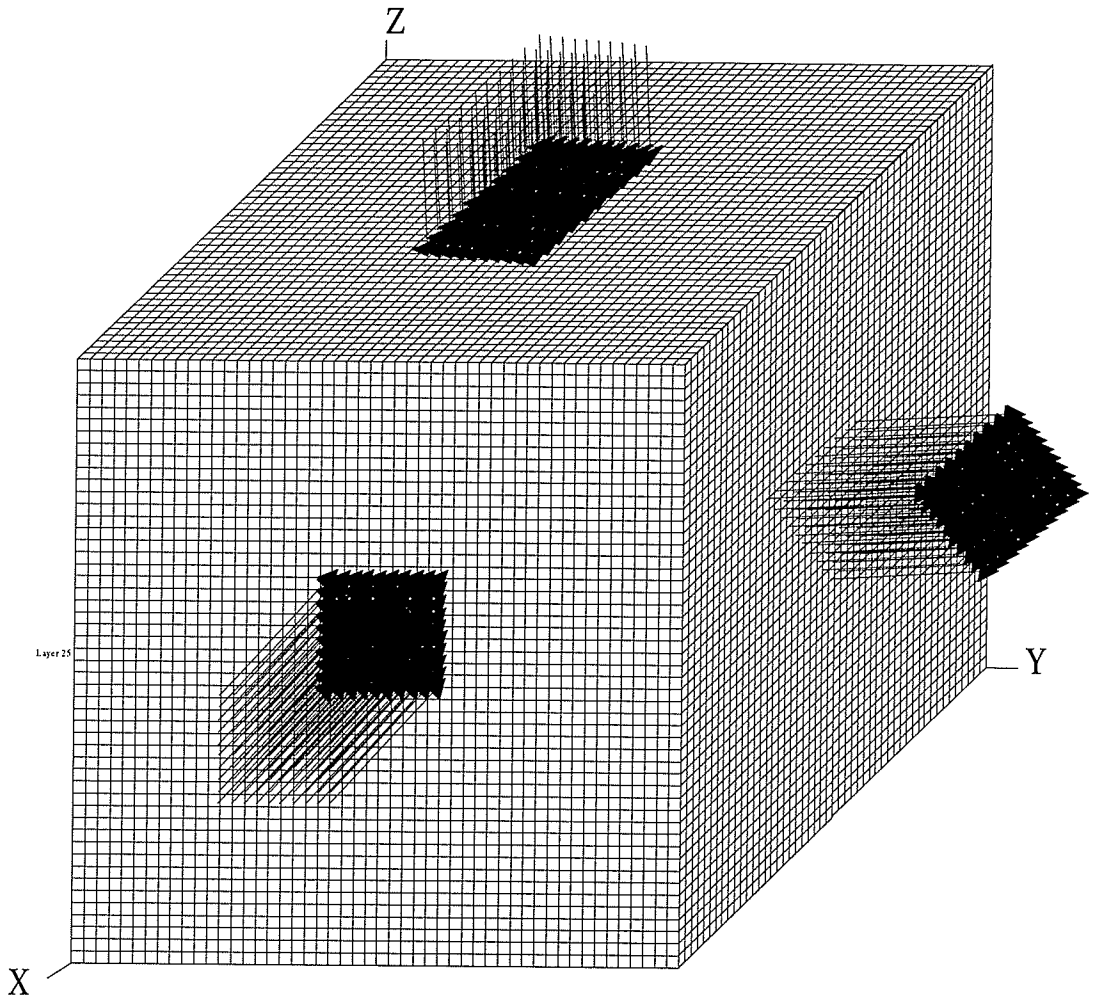

Figure 7.1: Simplified 3-D breast tumour imaging setup using the original Wexler 3-D EIT imaging algorithm. Arrows show points of injection/extraction (i.e., excitations). There is no injection/extraction on the side of the chest wall. There are 300 pairs of current excitations, 50 layers, and a total of 125,000 elements. Tumours (benign and malignant) elements are located at (x=13, y=13, and z=25) and (x=25, y=25, and z=25) respectively.

Figure 7.2 below shows a sequence of images recovered for layers 23 to 27 for simulation of Figure 7.1 using the original Wexler 3-D EIT algorithm at 100 iterations.

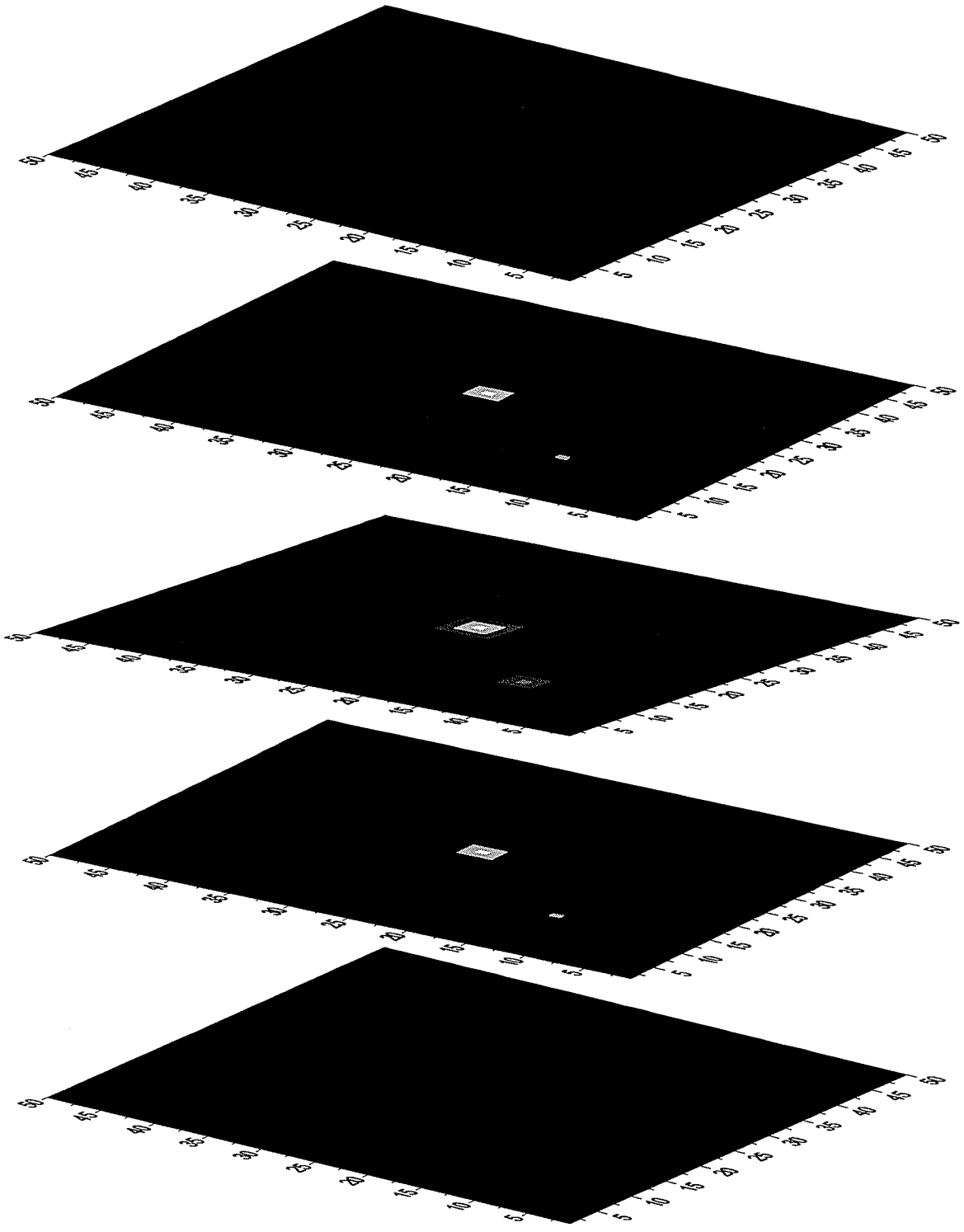

Figure 7.2: Recovered conductivity images with the original Wexler 3-D EIT algorithm for setup of Figure 7.1. Image (a) shows the gray level images of layers 23, 24, 25, 26, and 27 (from top to bottom) for 100 iterations.

7.4 The Improved Wexler 3-D EIT Algorithm: A Realistic 3-D Simulation

In order to demonstrate the effectiveness of the improved Wexler 3-D EIT algorithm, the previous simplified 3-D simulation of small breast tumour imaging described in Section 7.3 is repeated here. In this combined approach of the improved algorithm, the conductivity κ and potential ϕ were first initialized to 1.0 and 0.0 respectively. The original Wexler 3-D EIT algorithm was then used to sweep through the imaging region for 9 iterations. Thereafter, the MPC algorithm was used to model the past behaviour of potential and conductivity distributions. From the modeled potential and conductivity relations, a conductivity distribution κ_d was derived. The derived conductivity distribution was used to reinitialize the original Wexler algorithm and was allowed to run for approximately 5 iterations. Thereafter, the LC algorithm was applied for a period of 20 iterations. The whole recovery process took about 34 iterations to converge using the improved Wexler 3-D EIT algorithm. Figures 7.3 below show a sequence of images recovered for layers 23 to 27 for the simulation of Figure 7.1 using the improved Wexler 3-D EIT algorithm at 34 iterations.

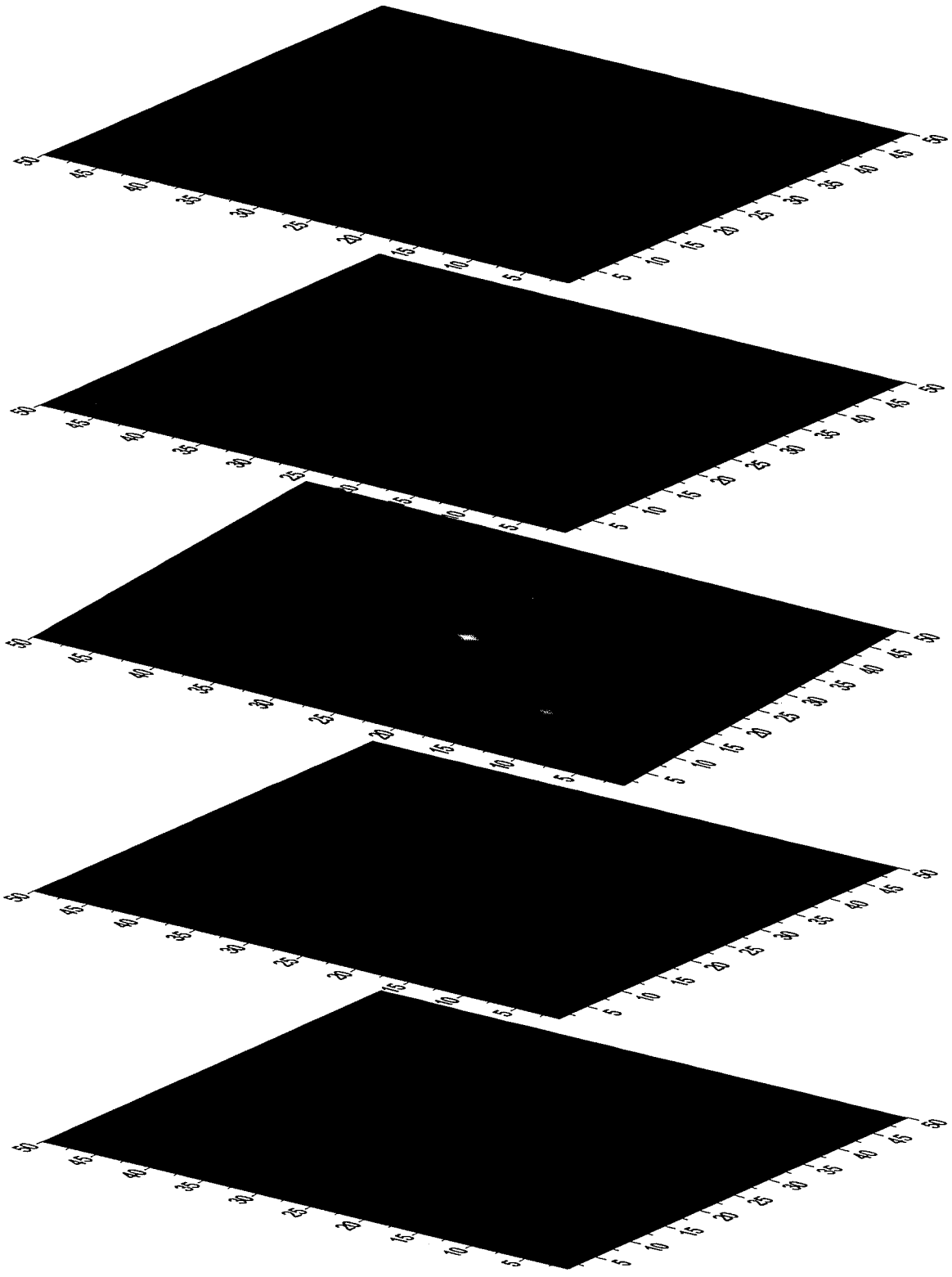

Figure 7.3: Recovered conductivity images with the improved Wexler 3-D EIT algorithm for setup of Figure 7.1. Images show the gray-level of layers 23, 24, 25, 26, and 27 (from top to bottom) for 34 iterations. Note both tumours are idemtified at layer 25

7.5 Discussion

In this chapter, the original Wexler 3-D EIT algorithm was used to image a simplified computer simulation model of small breast tumours (benign and malignant). The breast model was a cube of size 50×50×50 mm^3. The malignant and benign tumours were each of physical size 1 mm^3 in volume and had conductivity 4.0 and 2.0 respectively. The recovered image at 500 iterations had an average FWHMs value of 9.4% and 10.3% for the benign tumour and 13.6% and 14.9% for the malignant tumour in the cross-sectional and axial plane respectively. The FWHM obtained for the central (i.e., malignant) voxel (14.9%) here is in accordance to the measurements obtained in Chapter 3, Section 3.5 (14.1%). The difference was a result of the total number of excitations pairs used to recover the image.

When the improved algorithm was employed to recover the image, the convergence rate and the overall spatial resolution improved dramatically. By combining the development of the two previous chapters, i.e., via MPC and LC algorithms, the convergence rate and spatial resolution of the original Wexler algorithm improved dramatically even in the presence of a SNR level of 30 dB. The FWHMs in the cross-sectional and axial planes were 2.2% and 2.5% for the intermediate benign tumour and 2.7% and 3.1% for the malignant tumour of the diameter of the imaging region respectively. The recovered conductivity values for the benign and malignant tumours were 1.93 and 3.87 for known values of 2.00 and 4.00. An obvious improvement in resolution at diseased-to-normal tissue interface resulted with the implementation of the improved algorithm. The work carried out here demonstrates clearly an improvement over the original algorithm with FWHMs in the cross-sectional and axial plane of 13.0% and 14.5% respectively.

7.6 Summary

Using simplified 3-D simulation of breast tumour (benign and malignant) imaging, it was observed that the original Wexler 3-D EIT algorithm recovers images with low resolution, in particular at diseased-to-normal tissue interface and that image quality is degraded with addition of noise.

Implementation of the combined MPC and LC algorithms on the original Wexler 3-D EIT algorithm was demonstrated to improve both the convergence rate and overall spatial resolution. Simulation results indicated that the improved algorithm could resolve tumours (benign or malignant) of size 2.2 - 3.1 mm in diameter and in the presence of noise. The recovered conductivity values for the benign and malignant tumours were determined to be equal to 1.93 and 3.87 for simulated values of 2.00 and 4.00 respectively. This degree of performance is clinically useful.

Chapter 8

Results and Discussions

Breast cancer is the most common cancer in women worldwide [Park93]. It is ranked first in cancer deaths among women in developed countries and was second only to cervical cancer in developing countries [Pisa93]. As a consequence of demographic trends in aging and population growth, breast cancer deaths are expected to increase. If these trends continue in previously low-risk countries, it is predicted that the worldwide incidence of new breast cancer cases will be over one million annually by the year 2000 [Mill86]. Most of the women that develop breast cancer have no family history or other recognizable risk factors. There is no way to tell who will get breast cancer and no proven way to prevent it, so the best possible defense is to find the tumour as early as possible. Successful early detection depends on three methods [Newm97]:

- Performing monthly breast self-examinations,
- having a yearly clinical breast examination by a health care professional, and
- getting regular mammograms after age 40.

While routine breast self-examinations have been shown to aid in early detection and consequently in improving survival rate, a great majority of women still do not practice breast self-examinations [McLe88 and Mah92]. Modeste *et al.*, 1999, in a study among women in a Caribbean population, identified a low level of breast self-examination, infrequent clinical breast examinations as part of regular care, unavailability of mammography services, and cost of screening as barriers to early detection [Mode99]. It is evident that changes in the behaviour of women and

physicians are needed to increase the use of breast self-examination, clinical breast examination by a health care professional and mammographic screening [Frie98].

The ideal breast clinical test combines high sensitivity and specificity. That is, nearly all patients with disease will be identified by the test and patients without disease will not be inaccurately identified - few false negative and false positive results. However, current procedures for detection and diagnosis illustrate the difficulty of optimizing both sensitivity and specificity. Neither screening mammography nor clinical breast self-examinations provide a definitive diagnosis of breast cancer. Every patient with a positive screening test requires biopsies. However, in 67-87 percent of cases, biopsy of breast lesions discovered via screening mammography is negative for malignancy [Kuni93]. These usually result in associated risk, unnecessary discomfort, and increased cost.

In clinical trials, screening mammography has been shown to reduce mortality from breast cancer by about 25% to 30% among women aged 50 years and older after only 5 to 6 years from the initiation of screening. Among women 40 to 49 years old, the evidence supporting the efficacy of screening mammography is less convincing [Mill93, Neug95, and Esse96]. Elwood *et al.*, 1993 argued that the difference in effectiveness of screening mammography in younger women might relate both to the greater difficulty in distinguishing normal from abnormal tissue, and to greater growth speed and different biological characteristics of tumours [Elwo93]. In a study to determine factors that influence the sensitivity of modern first screening mammography, Kerlikowske *et al.*, 1996 showed that sensitivity is lowest among women younger than 50 years, possibly because of rapid tumour growth [Kerl96]. Thus, despite the value of mammography as a breast cancer screening tool and improvements in the technique, it remains an imprecise diagnostic technique. Jackson *et al.*, 1993 discussed that the radiologically dense breast in young women remains difficult to image despite improvement in mammography equipment and technique [Jack93].

A few imaging techniques are presently being investigated as a potential or complementary breast screening or diagnostic tools. Among these are ultrasound (US), nuclear medicine (NM), computerized tomography (CT) and magnetic resonance imaging (MRI) [Ders89]. As previously described in Chapter 1, these modalities have a limited role and have yet to demonstrate their efficacy. In brief, ultrasound has a limited role in the differentiation of cystic from solid masses and as a guide for aspiration and preoperative localization of selected breast lesions. Computed tomography has a more limited role to determine the spatial orientation of a lesion detected only in the lateral mammographic position. The other modalities are generally considered experimental with no demonstrated efficacy for early detection or diagnosis of breast cancer.

A new and emerging imaging technique, electrical impedance tomography (EIT), has been given a lot of attention recently. EIT is a technique that produces images of impedance (viz. conductivity or relative permittivity) distribution in a slice through the body by means of noninvasive electrical measurements and a reconstruction algorithm. EIT has many advantages among which are its noninvasiveness (i.e., no associated radiation hazard), its relatively inexpensive hardware requirements, and its ease of operation (i.e., minimal operator supervision). This technique has potential in medical, industrial, and environmental applications. In medical applications, EIT is being considered in lung, brain, and heart imaging among others [Moru96].

Many experimental studies have postulated that due to the differential electrical (or dielectric) properties of breast tissue (viz. normal, benign, and malignant), an EM radiation-based imaging technique (e.g., EIT) ought to be able to detect the characteristic dielectric contrast. To date, only a limited amount of work has been done on EIT of breast cancer imaging. This is mainly due to the fact that the spatial resolution requirement for clinical breast cancer imaging is considerably high and that the time for a complete scan is relatively longer than established imaging modalities.

Despite these stringent requirements, a few attempts at breast EIT imaging have been made. Skidmore *et al.*, 1987, described a data collection system for gathering electrical impedance measurements from the human breast [Skid87]. Holder *et al.*, 1994, obtained good quality in-vivo images of the female breast using the Sheffield Mark 1 electrical impedance tomography system [Hold94]. Larson-Wiseman, 1998 using the Rensselaer's third-generation adaptive current tomograph (ACT3) EIT system, along with a clustered electrode array configuration, showed the possibility of early breast cancer detection [Lars98]. Recently, Radai *et al.*, 1999, using 2-D simulations, demonstrated that the impedance technique is quite reliable and could be used to detect breast cancer [Rada99].

The purpose of this thesis was to demonstrate whether an improved Wexler 3-D EIT 'static' impedance image reconstruction algorithm could be used to detect and diagnose small breast tumours (i.e., of physical size 1-2 mm^3 in volume). If successful, a high detection rate would result, opening the prospect of making breast cancer a highly curable disease. Since EIT would be economical in capital outlay and maintenance, a much larger proportion of the female population (e.g., minorities and isolated communities) could be reached more effectively for screening purposes.

Simplified two- and three-dimensional computer models of the breast were employed to demonstrate the feasibility of the Wexler EIT algorithm in the detection and diagnosis of small breast tumours. The observations and results of the simulations are discussed here.

In Chapter 2, a review of the literature on the dielectric properties of breast tissue was provided. In some cases, it was observed that significant differences exist in the impedance properties of breast tissue (between normal, benign, and malignant). However, it was concluded that more extensive, particularly in vivo, studies of dielectric measurements of breast tissue samples are needed to establish values more accurately from subject to subject (i.e., inter-subject variability) and to investigate the reality of any differences between the different breast histopathological types and

normal tissue. However, as far as EIT imaging is concerned, the most crucial feature of tissue impedance is the existence of sufficient variation between different tissue types to allow appropriate imaging. Such variations, from the sparse data obtained so far, seem to be quite reliable.

In Chapter 3, the original Wexler (also known as the double-constraint method) image reconstruction algorithm was reviewed by performing simple 2-D and 3-D computer simulations of breast cancer imaging. In terms of image reconstruction methodology, it was observed that the Wexler algorithm has many advantages, the most important being that it transfers the difference in potential between the Neumann and Dirichlet boundary conditions to the interior (i.e., it provides local support) rather than to the boundary, unlike the procedure used in Newton-Raphson-like methods [Woo90]. This approach yields a sparse-matrix permitting use of efficient finite-element method solution schemes. Furthermore, currents are allowed to follow natural paths, and no attempt is made to force them to behave in beam-like fashion and image quality is not degraded by contact and spreading resistance as is inherent in resistance projection techniques [Bate80].

Optimally, in the clinical situation, image acquisition ought to be relatively fast and accurate. However, it was apparent from the simulations performed that the original Wexler EIT algorithm was slowly convergent and that the spatial resolution was inadequate for clinical imaging purposes. For the more realistic 3-D model of breast cancer imaging simulation described in Section 3.5, the algorithm converges in approximately 3 hours and 47 minutes at approximately 8,000 iterations on a SUNW, SPARCstation-4. The spatial resolution of the 2-D simulation was observed to be much lower than that of the 3-D case. This was associated with the physics of the inverse problem. The original Wexler 3-D algorithm can only resolve up to 13.0% in the cross-sectional plane and 14.6% in the axial plane of the diameter of an imaging region as demonstrated by simulations.

Closer analysis of the recovered image appears to indicate that the recovered conductivity of the central element was affected by closely surrounding elements. It appears as though the difference in conductivity, between simulated and recovered conductivity for the central element, was equally distributed to the immediate surrounding elements. As a result of which, the magnitude of the recovered conductivity of the central element was consequently lower than what was anticipated. This effect appears to be more pronounced in the 2-D case than the 3-D case. This phenomenon is probably due to the fact that electrical current is not restricted to the 2-D plane.

The observations and results of Chapter 3 are summarized and discussed as follows:

- The algorithm used the correct physical approach. As such, it yields a sparse matrix permitting use of efficient finite element schemes.
- Currents were allowed to follow natural paths and image quality was not degraded by contact and spreading resistance.
- Being iterative, the algorithm's convergence rate was characteristically slow.
- Recovered spatial resolution both in the cross-sectional and axial plane was not of clinical potential.
- Recovered conductivity differences (i.e., between simulated and recovered) of an element (i.e., pixel or voxel) of interest appears to "dissipate" or "spread" equally among immediate surrounding elements.

Though faster convergence rate and relatively higher spatial resolution are important requirements of a reliable clinical image-processing algorithm, they are not the only prerequisites. In Chapter 4, a series of tests and effects, of relevance to clinical expectations, was conducted on both the original Wexler 2-D and 3-D EIT algorithms. These tests and effects were conducted for the purpose of evaluating the potential of the Wexler EIT algorithm in a clinical environment and to identify "areas needing improvement".

The observations and results of Chapter 4 are summarized and discussed as follows:

- It was determined that if the initial starting conductivity distribution was equivalent to the exact conductivity distribution, the Wexler EIT algorithm converges at the first iteration. This observation supports the accuracy of the mathematical code. Through simulations, it was also observed that a good starting value would produce correct results, while a poor initial guess may not lead to convergence. This observation is supported by other studies [Mura85 and Avis95]. In the 2-D and 3-D simulations the tumour element (i.e., pixel or voxel) had a conductivity of 4.0 and the background region was at 1.0. It was observed that, if the algorithm was initialized with a homogeneous conductivity of 2.0, the convergence rate improves over that of the homogeneous 1.0. However, the improvement is not significantly better than if the initial assumption of 3.0, 4.0 and 5.0 was made. This observation supports the importance of incorporating a priori information in EIT algorithms.

- In section 4.3, an investigation was performed to derive an optimal excitation and measurement pattern configuration. It was determined that excitation patterns that employed a symmetrical or near-symmetrical configuration provide faster convergence and improves image quality. The combination of minimal node involvement, symmetrical or near-symmetrical excitation patterns, and *sometimes* measurement patterns provide the optimal configuration for the imaging of breast tumour.

- In Section 4.4, an investigation into the finite element size effect on convergence rate and image quality was conducted. Mu, 1994 described a procedure that starts with a coarse mesh to obtain an initial guess and a fine mesh to recover the image accurately in the solution of the inverse problem. Mu argued and demonstrated that convergence speed would be greatly

reduced if a coarse mesh were used first to obtain an approximate solution, then a finer mesh to reach the true image. The observations derived by Mu [Mu94] were implemented on the standard 2-D and 3-D computer simulation examples for breast cancer imaging. Results of simulations indicated that Mu's scheme improves the convergence rate and subsequently the image quality.

- In section 4.5, the effect on convergence speed of the spatial location of tumour was demonstrated. It was observed that better convergence rate is attained if the tumour is located on the periphery of the object than if it was located in an intermediate or central position within the object. It was also observed that conductivity of the element on the edge of a central tumour element increases with iteration count at early iterations. The conductivity value of the edge element then decreases at later iterations. This phenomenon appeared to affect the resolution at the sharp edges of the diseased-to-normal tissue interface. This effect was termed the "Tumour-Edge" effect. If the potential and conductivity distributions are known from past history, the distributions at convergence can be determined by interpolation. This observation will prove crucial in developing a method to improve the convergence speed of the algorithm.

- In section 4.6, an investigation of the behaviour of spatial resolution as a function of the location of the tumour was performed. It was determined that the resolution of EIT is spatially variant. The resolution of a tumour at a peripheral location is superior to that at intermediate and central locations. When compared to values obtained from the literature, the spatial resolution of the original Wexler 2-D and 3-D EIT were found to be quite similar to those obtained by [Ider95 and Meth96]. It is apparent that if the loss in resolution, in particular at the diseased-to-normal tissue interface, as a function of tumour spatial location could be compensated, EIT spatial resolution would improve drastically.

- The "Tumour-Edge" effect identified in Section 4.5 and 4.6 was investigated further in Section 4.7. It was determined that this effect was responsible for the poor spatial resolution at the diseased-to-normal tissue interface. A figure-of-merit was introduced to quantify the difference between the simulated and recovered conductivity at the tumour location. The figure-of-merit was termed the conductivity profile ratio and was represented by τ. This provides a measure of how close the recovered distribution is to the simulated distribution and would be used to assess improvement in spatial resolution at the diseased-to-normal tissue interface.

- In section 4.8, the effect of instrumentation or device noise on convergence rate and recovered image quality was investigated. It was observed that, with the *sometimes* measurement pattern, a tumour of appropriate contrast could be distinguished adequately from the background region. The fact that the algorithm can handle noise that will be characteristic of a clinical EIT-based system further adds to its potential in medicine.

- In section 4.9, the effect of electrode-electrolyte (or electrode-skin) impedance on recovered image quality was discussed. It was determined that for the Wexler algorithm, the effects of electrode-contact resistance are minimal, if any. Furthermore, accurate finite element models of the impedance of the skin and that of the chestwall ought to be considered in the imaging reconstruction algorithm.

- In section 4.10, the effect of electrode and patient motion was investigated on simple breast model. It was shown that the original Wexler EIT algorithm is not affected significantly with electrode motion. Simulation of breast motion showed that the original Wexler EIT algorithm would not perform that accurately in the presence of patient motion. Methods were suggested that would address this issue.

- An experimental study of the effect of the third dimension on the 2-D Wexler EIT system was conducted in Section 4.11. It was observed through simulations that the 2-D Wexler EIT system inevitably produces three-dimensional current flow. This renders interpretation of EIT images difficult. This study had shown that a detailed understanding of the nature of this 3-D effect is essential and ought not to be neglected. This effect has justified the focus of this thesis on the development of an improved Wexler 3-D EIT algorithm rather than the 2-D algorithm.

Based on the observations made in Chapters 3 and 4, it was obvious that one of the crucial "areas needing improvement" of the Wexler algorithm was the relatively longer time it took the algorithm to converge. Further, as discussed in Chapter 4, it was of significant importance that any realistic attempt at imaging the breast ought to be done in three-dimensions, i.e., 3-D. As such, the focus of Chapter 5 was to improve the convergence rate of the original Wexler 3-D EIT algorithm.

An algorithm was developed and implemented on 3-D computer simulations of small breast tumour imaging. The algorithm was arrived at from an important observation made in Section 4.6, an investigation on the convergence rate of the algorithm as a function of spatial location of tumour. It was observed that if the potential and conductivity distributions of the algorithm at the first few iterations are known, future (i.e., at later iteration) distributions could be predicted. That was the basis of the Modeller-Predictor-Corrector (MPC) algorithm developed to improve the time of convergence.

In brief, the MPC involved modelling past behaviour of potential and conductivity distributions, predicting conductivity distribution at an iteration close to convergence by using predicted potential distribution, and correcting conductivity distribution by reinitializing the original Wexler algorithm with the predicted conductivity distribution. Results of simulation performed on a simple 3-D breast model (of size $25 \times 25 \times 25$ mm^3) in an attempt to detect a 1 mm^3 tumour indicated that the MPC

algorithm is quite effective in improving the time of convergence. At 20 iterations, for a time period of 7.4 minutes, on a SUNW, SPARCstation-4, the recovered conductivity distribution, obtained using the MPC algorithm, was determined to be quite close to the exact conductivity distribution. The conductivity profile matching ratio τ ($0 < \tau \leq 1$), for the original Wexler, Strobel's multistep, and MPC methods were determined to be 0.35, 0.78, and 0.82 respectively. The difference between the MPC recovered conductivity profile and that of the exact distribution was identified to be at the tumour (i.e., benign and malignant)-edge interface. Note that this effect, termed the "Tumour-Edge" effect earlier, was initially identified in Chapter 4. Despite the major improvement in the time of convergence, now comparable to existing imaging modalities, the spatial resolution, in particular at diseased-to-normal tissue interface, was yet to improve. The "Tumour-Edge" effect, identified earlier as responsible for the observed low resolution, was closely investigated in Chapter 6.

The observations and results of Chapter 5 are summarized and discussed as follows:

- The original Wexler 3-D EIT algorithm was identified as slowly convergent.
- The Modeller-Predictor-Corrector (MPC) algorithm was developed to improve time of convergence of the original Wexler 3-D EIT algorithm.
- Results of computer simulations on a simplified 3-D breast model, using the MPC scheme, showed a drastic improvement in convergence rate.
- Conductivity profile matching ratio τ was identified to be higher than the original or multistep methods. Consequently, an appropriate and useful conductivity image was recovered in a relatively shorter time span comparable to existing imaging modalities.
- Overall spatial resolution had improved. The FWHMs of the recovered image at 20 iterations in the cross-sectional and axial plane were 6.2% and 7.1% of the diameter of the imaging region respectively. These results were an

improvement over the original algorithm with FWHMs in the cross-sectional and axial plane of 13.0% and 14.5% respectively.

- It was observed that due to the "Tumour-Edge" effect, resolution at diseased-to-normal tissue interface did not improve that considerably.

The Locator-Compensator (LC) algorithm developed in Chapter 6 was used to address the observed "Tumour-Edge" effect. In brief, the LC algorithm involved using a variant of the peak detection method to locate peak(s) and a combined conductivity-updating scheme to compensate for resolution at located peak(s). The LC method was implemented on a computer simulation of a simplified 3-D breast model (of size 25×25×25 mm^3), in an attempt to image a small tumour of size 1 mm^3 in volume. The FWHMs in the cross-sectional and axial plane were 5.4% and 6.3% of the diameter of the imaging region respectively. Results showed an improvement over the original algorithm with FWHMs in the cross-sectional and axial plane of 13.0% and 14.5% respectively.

The observations and results of Chapter 6 are summarized and discussed as follows:

- The original Wexler 3-D EIT algorithm was identified to have overall low resolution.
- The Locator-Compensator (LC) algorithm was developed to improve spatial resolution of the original Wexler EIT algorithm, in particular, at diseased-to-normal tissue interface.
- Results of computer simulations on a simplified 3-D breast model, using the LC scheme, showed a drastic improvement in resolution at diseased-to-normal tissue interface.
- An observed two-fold increase in resolution magnitude was observed.

In Chapter 7, an improved Wexler 3-D algorithm was demonstrated on a more realistic computer simulation of a simplified breast model. The breast model was a cube of size 50×50×50 mm^3. The malignant and benign tumours were of physical size 1 mm^3 in volume and had conductivity 4.0 and 2.0 respectively. By combining the development of the two previous chapters, i.e., MPC and LC algorithms, the convergence rate and spatial resolution of the original Wexler algorithm improved dramatically even in the presence of a SNR level of 30 dB. The FWHMs in the cross-sectional and axial planes were 2.2% and 2.5% for the intermediate benign tumour and 2.7% and 3.1% for the malignant tumour of the diameter of the imaging region respectively. The recovered conductivity values for the benign and malignant tumours were 1.93 and 3.87 for known values of 2.00 and 4.00. The improved Wexler 3-D EIT algorithm clearly demonstrated that small breast tumours can be detected and diagnosed accurately with EIT.

The observations and results of Chapter 7 are summarized and discussed as follows:

- The original Wexler 3-D EIT algorithm was identified to have overall low convergence rate and spatial resolution, in particular at diseased-to-normal tissue interface.
- By combining the MPC and the LC algorithms of Chapters 5 and 6 respectively, an improved Wexler 3-D EIT algorithm was obtained.
- Results of computer simulations on a more realistic 3-D breast model, using the improved LC, showed a drastic improvement in resolution at diseased-to-normal tissue interface.
- EIT can be used to detect and diagnose small breast tumours.

The improved Wexler 3-D EIT algorithm for imaging small breast tumour developed here was demonstrated on uniform geometry. Though realistically, the breast is not uniform, the improved and refined algorithm presented here would perform similarly for nonuniform geometry as demonstrated by Mu, 1994 [Mu94].

Chapter 9

Conclusions and Future Work

9.1 Conclusions

The statistics for breast cancer, a common cancer in women, are sobering and downright scary. The chance of recovery (i.e., prognosis) and choice of treatment depend on the stage of discovery of the cancer. Early detection is a woman's hope for effective treatment and better survival rates. However, present clinical techniques are either ineffective (e.g., mammography) for early detection or financially unjustifiable (e.g., magnetic resonance imaging) for mass screening. As such, other imaging modalities are being investigated e.g., ultrasound, computerized tomography, radionuclide scanning, and electrical impedance tomography.

Among the screening techniques under investigation, electrical impedance tomography (EIT) appears to offer the most promising solution. EIT offers several advantages over other clinical and experimental techniques. EIT's positive attributes are its ability to produce images at reduced, if any, biological hazard, its relatively inexpensive instrumentation requirements, and its physical ease of operation. Despite these obvious advantages, EIT remains an experimental tool with little, if any, importance to medicine yet. So far, from a medical perspective, the spatial resolution of EIT is not as good as may be achieved by other techniques. The goal of this thesis was to demonstrate otherwise.

The original Wexler EIT algorithm was reviewed by performing 2-D and 3-D computer simulations of simplified breast cancer imaging. It was observed that the algorithm satisfies most of the standard criteria expected of an EIT image-processing scheme, with clinical potential in the early detection of breast tumours. The approaches utilized and the results obtained in this work, in an attempt to accomplish the objective, are summarized as follows:

- On the basis of the alarming statistics for breast cancer and the ineffectiveness of X-ray mammography for early detection, an alternate method (Electrical Impedance Tomography, EIT) was investigated. The focus was to further the development and refinement of an existing EIT 'static' image reconstruction algorithm, namely, the Wexler algorithm. The inevitable question was posed. Can an improved Wexler EIT 'static' imaging algorithm be employed to image small breast tumours of size 1 - 2 mm in diameter?

- The rationale for choosing EIT, as an alternate breast cancer imaging modality, was discussed in Chapter 2. EIT is an imaging methodology that is based upon electrical impedance (or 'dielectric') contrasts within the body. A review of literature on the dielectric properties of breast tissue was conducted. Generally, differential dielectric properties (viz., conductivity or relative permittivity) between normal and diseased breast tissue were observed. However, it was concluded that despite the variability of dielectric properties of tissues, more extensive studies of dielectric measurements of breast tissue samples are needed, in particular, to establish values more accurately from tissue to tissue (i.e., inter-subject variability) and to investigate the reality of any differences between tumours and normal tissue. As far as EIT imaging is concerned, the most crucial feature of tissue impedance is the existence of sufficient variation between different tissue types to allow appropriate imaging.

- In Chapter 3, the original Wexler EIT algorithm was reviewed. A few advantages were identified. In particular, the algorithm yields a sparse-matrix and thus efficient finite-element method solution schemes could be employed, currents are allowed to follow natural paths without constraining them to behave in beam-like fashion, and image quality is not degraded by contact and spreading resistance as is inherent in resistance projection techniques. However, early observations of two- and three-dimensional computer simulations on simple 3-D breast model performed appear to indicate two major difficulties that are crucial to the clinical success of the algorithm in the imaging of breast cancer. The convergence rate was too slow and the recovered spatial resolution, in particular at diseased-to-normal tissue interface was not sufficient for early breast cancer imaging (i.e., detection and diagnosis).

- More detailed analyses were performed on the original Wexler 2-D and 3-D EIT algorithm to determine its characteristics and 'dynamics'. The purpose of the analyses was to determine whether the original Wexler algorithm could satisfy the stringent requirements expected of an established clinical imaging algorithm, and to identify "areas needing improvement" in an attempt to image small breast tumours. The ability to provide fast, accurate, repeatable, low-noise, and clinically meaningful images were among the criteria of interest. Two- and three-dimensional computer simulations indicated that, in general, the algorithm could perform well in a clinical environment. Image quality was not affected with patient motion and in the presence of noise, and reasonable images were recovered when electrode-electrolyte impedance was taken into account. In brief, the Wexler algorithm was observed to be stable and quite robust. However, two crucial "areas needing improvement" were identified. These were the scan time (or convergence rate) and the overall spatial resolution, in particular at diseased-to-normal tissue interfaces. The focus of this thesis was on developing methods that would improve these shortcomings.

- One of the observations made in Chapter 4 was that with a knowledge of past conductivity distribution, future distributions could be determined by extrapolating the modeled past conductivity distributions. Simply stated, if the history of conductivity distributions is known at early iterations, it can be modelled and used to estimate the distribution at later iterations. This is the observation, which was at the basis of the Modeller-Predictor-Corrector (MPC) scheme. In brief, the MPC method involved modelling the past behavior of conductivity and potential distributions at early stage. Subsequently, the fitted equations were used to derive a conductivity distribution close to or at convergence. To minimize error due to extrapolation, the derived conductivity distribution was used to reinitialize the image reconstruction algorithm. When implemented on 3-D computer simulations of early stage breast tumour imaging, convergence rate appears to improve dramatically. As such, scan time was relatively comparable to present breast cancer imaging modalities. This was clearly identified as an improvement over the original Wexler 3-D EIT algorithm.

- It was also observed in Chapter 4 that the spatial resolution of EIT is relatively lower at the center than at an intermediate or peripheral location for a region. Simply stated, EIT is space variant. Further, the resolution at diseased-to-normal interface was determined to be relatively poor. On that basis, a Locator-Compensator (LC) scheme was developed and implemented on 3-D computer simulations of early stage of breast tumour imaging. In brief, the LC method involved two major steps. In the first step, region(s) of interest was/were localized using a variant of the peak detection algorithm. Once localized, the conductivity values of the peak(s) were compensated for loss in spatial resolution using a combined conductivity-updating scheme. Results obtained with the LC algorithm improved resolution at diseased-to-normal tissue interface considerably.

- In Chapter 7, a combined algorithm, incorporating the MPC and LC schemes with the original Wexler 3-D EIT algorithm, was developed and implemented on simplified 3-D computer simulations of small breast tumour (benign and malignant) imaging. The focus was to show that an improved Wexler 3-D algorithm could be used to image small breast tumours. Results of simulations indicated significant improvement in convergence rate and overall spatial resolution. Detection and diagnosis of early breast diseased tissue (viz., benign and malignant) of physical size 2.2 - 2.7 mm was demonstrated with the improved algorithm.

In this thesis, an EIT image reconstruction algorithm, namely, the original Wexler EIT algorithm was investigated to demonstrate its potential in the imaging of early stages of breast cancer. The algorithm was tested rigorously, using simulations, to assess some criteria expected of a clinical imaging tool. It was shown that the algorithm is relatively stable and robust. However, initial scan time and spatial resolution were not appropriate for medical applications. As such, methods were devised to refine and improve the original algorithm. The improved Wexler 3-D EIT algorithm was implemented on simplified 3-D computer simulations. It was observed that the algorithm could resolve up to (2.2 - 2.7)% of the diameter of an imaging region. For the simplified model of the breast adopted here, the improved algorithm was able to detect and resolve tumour of size similar to an average duct size (1-2 mm).

The goal of this thesis was to demonstrate that an improved Wexler 3-D EIT algorithm can be used to detect and diagnose breast tumour of size 1 - 2 mm in diameter (i.e., the size corresponding to an average female human duct). The work carried out here, was successful in demonstrating:

- The potential of EIT as a clinical tool in breast cancer imaging.
- That the continuous development of a clinical EIT system is justified.

- The medical community will have at their disposal an inexpensive noninvasive tool that will either replace or complement mammography in the race for a cure.

9.2 Future Work

The focus of this thesis was on the algorithmic development of an iterative EIT image reconstruction algorithm, namely, the Wexler algorithm. It was demonstrated, through realistic computer simulations, that the improved Wexler algorithm could be employed to image small breast tumours. Ideally, for a proper clinical assessment of the algorithm, real measurements on a statistically representative group of subjects will have to be used. Consequently, this can only be accomplished with the use of existing and/or development of an appropriate data acquisition system.

The clinical success of the improved Wexler EIT 'static' image reconstruction algorithm will depend on the appropriate hardware. Though this work has demonstrated the usefulness of a robust and fast algorithm, only with the proper hardware, complementary with the algorithm developed here, will EIT be successful in the detection of small breast tumours.

The improved Wexler EIT algorithm, as demonstrated in this thesis, can be of potential in the imaging of early stage of breast cancer. However, it is evident that what has been achieved here is only a demonstration of feasibility, requiring further development to meet the ultimate goal of a clinical EIT-based breast cancer imaging system (i.e., to be able to detect and diagnose breast tumour of size 1.0 mm^3 in volume). As such, the focus of future developments, complementary to the improved Wexler EIT algorithm, would most likely be in the following areas, outlined here as questions:

- How best to take measurements on the breast? Would a plastic breast holder fashioned in the shape of a brassiere cup with the appropriate types, sizes, and

placements of electrodes be more effective than immersing the breast in a container of electrically conductive fluid with the inner surface of the container supporting the electrodes? Can the algorithm be implemented with existing, i.e., off-shelf hardware?

- How will the improved Wexler 3-D EIT algorithm perform in real clinical situations? This can only be known if a clinical EIT machine is built in the very near future. The works carried out in this thesis justifies the feasibility of developing such a unit.

- If a clinical unit is developed, more studies on larger groups of subjects and comparisons with existing techniques need to be performed to correctly assess the potential of EIT as a clinical tool.

These and other questions will need to be fully addressed before a clinical EIT system, utilizing the improved Wexler image reconstruction algorithm, can be developed. It is anticipated that with the algorithmic development presented here, along with the future works outlined above, the transition of EIT from the laboratory to the clinic would become a reality.

References

[Avis92] N. J. Avis, D. C. Barber, B. H. Brown, and M. A. Kiber, " Back-projection distortions in applied potential tomography images due to non-uniform reference conductivity distributions," *Clin. Phys. Physiol. Meas.*, vol. 13, Suppl. A, pp. 113-117, 1992.

[Avis95] N. J. Avis and D. C. Barber, "Incorporating a priori information into the Sheffield filtered backprojection algorithm," *Physiol. Meas.*, vol. 16, no. 3, Suppl. A, pp. A111-122, 1995.

[Barb83] D. C. Barber, B. H. Brown, and I. L. Freeston, "Imaging spatial distributions of resistivity using applied potential tomography," *Electronic Lett.*, vol. 19, no. 22, pp. 933-935, 1983.

[Barb87] D. C. Barber and A. D. Seagar AD, "Fast reconstruction of resistance images," *Clin. Phys. Physiol. Meas.*, vol. 8, Suppl. 2A, pp. 47-54, 1987.

[Barb93] D. C. Barber, "An overview of image reconstruction: Clinical and Physiological Applications of Electrical Impedance Tomography," ed., D. S. Holder, London: UCL Press, 1993.

[Barb95] D. C. Barber, "Electrical impedance tomography, applied potential tomography. In: Beneken, J. E. W. and Thevenin, V., Eds., *Advances in Biomedical Engineering*, Amsterdam: IOS Press, pp. 165-173, 1995.

[Bate80] R. H. T. Bates, G. C. McKinnon, and A. Seager, "A limitation on systems for imaging electrical conductivity distributions," *IEEE Trans. Biomed. Eng.*, vol. 27, pg. 418, 1980.

[Bayf95] R. Bayford, Y. Hanquan, K. Boone, and D. S. Holder, "Experimental validation of a novel reconstruction algorithm for electrical impedance tomography based on backprojection of Lagrange multipliers," *Physiol. Meas.* vol. 16, no. 3, Suppl. A pp. A237-47, 1995.

[Bays98] U. Baysal and B. M. Eyuboglu, " Use of a priori information in estimating tissue resistivities--a simulation study," *Phys. Med. Biol.*, vol. 43, no. 12, pp. 3589-3606, 1998.

[Benn91] I. C. Bennett, R. Jr. Freitas, and I. S. Fentiman, "Diagnosis of breast cancer in young women," *Aust. N Z J. Surg.*, vol. 61, no. 4, pp. 284-289, 1991.

[Bern79] J. Bernhardt, "Biological effects of electromagnetic fields," *IEEE Trans. Nuclear Sci.*, vol. NS-26, no. 2, pp. 2736-2739, 1979.

[Berr92] J. G. Berryman, "Lecture Notes on Electrical Impedance Tomography, Lawrence Livermore National Library, California, USA., 1992

[Bevi92] P. R. Bevington and D. K. Robinson, "Data reduction and error analysis for the physical sciences," McGraw Hill, ISBN: 0079112439, 1992.

[Blad94] B. Blad, K. Lindstrom, L. Bertenstam, B. R. Persson, and N. G. Holmer, " A current injecting device for electrical impedance tomography," *Physiol. Meas.*, vol. 15, Suppl. 2A, pp. A69-A77, 1994.

[Blad95] B. Blad and B. Baldetorp, "Impedance spectra of tumour tissue in comparison with normal tissue: A possible clinical application for electrical impedance tomography, *Proc. IX ICEBI*, Heidelberg, Germany: University of Heidelberg, pp. 223-224, 1995.

[Bodn99] M. Bodnar, Miller OF 3rd, and W. Tyler, "Paget's disease of the male breast associated with intraductal carcinoma," *J. Am. Acad. Dermatol.*, vol. 40, no.5, part 2, pp. 829-31, 1999.

[Boon96] K. G. Boone and D. S. Holder, " Current approaches to analogue instrumentation design in electrical impedance tomography," *Physiol. Meas.,* vol. 17, no. 4, pp. 229-247, 1996.

[Boon97] K. Boone, D. Barber, and B. Brown, "Review: Imaging with Electricity: Report of the European Concerted Action on Impedance Tomography," *J Med. Eng. Tech.*, vol. 21, no. 6, pp. 201-232, 1997.

[Bren97] R. J. Brenner and E. A. Sickles, "Surveillance mammography and stereotactic core breast biopsy for probably benign lesions: a cost comparison analysis", *Acad. Radiol.*, vol. 4, no. 6, pp. 419-425, 1997.

[Brow82] B. H. Brown and D. C. Barber, "Applied Potential Tomography - a new in vivo medical imaging technique," *Proc. Hospital Physicists Annual Conference, Sheffield, Clin. Phys. Physiol. Meas.*, vol. 4, no. 1, 1982.

[Brow94] B. H. Brown, A. D. Leathad, L. Lu, W. Wang, and A. Hampshire, "Measured and expected Cole parameters from electrical impedance tomographic spectroscopy images of the human thorax," *Physiol. Meas.*, vol. 16, Suppl. 3A, pp. A57-A67, 1995.

[Brow95] B. H. Brown, D. C. Barber, A. D. Leathad, I. Lu, W. Wang, R. H. Smallwood, and A. J. Wilson, "High frequency EIT data collection and parametric imaging," *Innv. Tech. Biol. Med.*, vol. 15, Suppl. 1, pp. 1-18, 1994.

[Camp92] A. M. Campbell and D. V. Land, "Dielectric properties of female human breast tissue measured *in vitro* at 3.2 GHz," *Phys. Med. Biol.*, vol. 37, no. 1, pp. 193-210, 1992.

[Camp94] J. H. Campbell, N. D. Harris, F. Zhang, B. H. Brown, A. H. Morice, "Clinical applications of electrical impedance tomography in the monitoring of changes in intrathoracic fluid volumes," *Physiol. Meas.*, vol. 15, no. 6, Suppl. 2A, pp. A217-A22, 1994.

[Chau84] S. S. Chaudhary, R. K. Mishra, A. Swarup, and J. M. Thomas, "Dielectric properties of normal and malignant human breast tissue at radiowave and microwave frequencies," *Indian J. Biochem. Biophys.*, vol. 21, pp. 76-79, 1984.

[Chen99] M. Cheney, D. Isaacson, and J. C. Newell, "Electrical Impedance Tomography," SIAM Review, vol. 41, no. 1, pp. 85-101, 1999.

[Cher95] V.A. Cherepenin, A. V. Korjenevsky, V. N. Kornienko, Yu. S. Kultiasov, and M. Yu. Kultiasov, "The electrical impedance tomograph: new capabilities," *Proc. IX Int. Conf. Electrical Bio-Impedance* (Heidelberg), pp. 430-433, 1995

[Cohe85] M. I. Cohen, R. A. Mintzer, H. J. Matthies, and J. R. Bernstein, "Mammography in women less than 40 years of age," *Surg. Gynecol. Obstet.*, vol. 160, no. 3, pp. 220-222, 1985.

[Cole42] K. S. Cole and R. H. Cole, "Dispersion and absorption in dielectrics. II. Direct current characteristics," *J. Chem. Phys.*, vol. 10, pp. 98, 1942.

[Cole98] C. F. Cole, "Issues in breast imaging," *Lippincotts Prim. Care Pract.*, vol. 2, no. 2, pp. 141-148, 1998.

[Cond97] T. Condamines and P. M. Marsili, "A New Version of Wexler Algorithm in Electrical Impedance Tomography," *Conference on inverse problems of wave propagation and diffraction*, INRIA, 1996.

[Conw92] J. Conway, M. Hawley, Y. Mangnall, H. Amasha, and G. C. van Rhoon, "Experimental assessment of electrical impedance imaging for hyperthermia monitoring," *Clin. Phys. Physiol. Meas.*, vol. 13, Suppl. A, pp. 185-189, 1992.

[Cook94] R. D. Cook, G. J. Saulnier, D. G. Gisser, J. C. Goble, J. C. Newell, and D. Isaacson, "ACT3: a high-speed, high-precision electrical impedance tomograph," *IEEE Trans. Biomed. Eng.*, vol. 41, no. 8, pp. 713-22, 1994.

[Cris93] W. J. Crisp, M. J. Higgs, W. K. Cowan, W. J. Cunliffe, J. Liston, L. G. Lunt, D. J. Peakman and J. R. Young, "Screening for breast cancer detects tumours at an earlier biological stage," *Br. J. Surg.*, vol. 80, no. 7, pp.863-865, 1993.

[Dehg99] H. Dehghani, D. C. Barber, and I. Basarab-Horwath, "Incorporating a priori information into image reconstruction in electrical impedance tomography, " *Physiol. Meas.*, vol. 20, no. 1, pp. 87-102, 1999.

[Ders89] D. D. Dershaw and M. Osborne, "Imaging techniques in breast cancer," *Semin. Surg. Oncol.*, vol. 5, pp. 82-93, 1989.

[Dijk93] A. M. Dijkstra, B. H. Brown, A. D. Leathard, N. D. Harris, D. C. Barber, and D. L. Edbrooke, "Clinical Applications of Electrical Impedance Tomography," *J. Med. Eng. Technol.*, vol. 17, no. 3, pp. 89-98, 1993.

[Doga83] K. Doganis and D. L. Scharfetter, "General optimization and extraction of IC device model parameters," *IEEE Trans. Elect. Dev.*, vol. 30, no. 9, pp. 1219-1228, 1983.

[Duck90] F. A. Duck, "Physical properties of tissue: A Comprehensive Reference Book," Academic Press, Harcourt Brace Jovanovich, Publishers, 1990.

[Elwo93] J. M. Elwood, B. Cox B, and A. K. Richardson, " The effectiveness of breast cancer screening by mammography in younger women," *Online J. Curr. Clin. Trials*, Doc. no. 32, 1993.

[Engl49] T. S. England and N. S. Sharples, "Dielectric properties of the human body in the microwave region of the spectrum," *Nature.*, vol.163, pp. 487-488, 1949.

[Engl50] T. S. England, "Dielectric properties of the human body for wavelenghts in the 1-10 cm range," *Nature.*, vol.166, pp. 480-481, 1950.

[Esse96] L. Esserman and K. Kerlikowske, " Should we recommend screening mammography for women aged 40 to 49?" *Oncology (Huntingt)*, vol. 10, no. 3, pp. 357-364, 1996.

[Eyub92] B. M. Eyuboglu and T. C. Pilkington, "Anisotropic skeletal muscle conductivity in electrical impedance tomography," in *Proc. Annu. Conf. IEEE Eng. Med. Biol. Soc.*, vol. 14, pp. 1726-1727, 1992.

[Flet87] R. Fletcher, "Practical Methods of Optimization," John-Wiley, 1987.

[Folk85] L. Folke and O. Ljungberg, "Atlas of Breast Pathology," Lippincott Williams & Wilkins Publishers, ISBN: 0397582978, 1985.

[Fost86] K. R. Foster and H. P. Schwan, "Dielectric properties of tissues; in Polk, Postow, CRC handbook of biological effects of electromagnetic fields," CRC Press, Boca Raton, 1986.

[Fost89] K. R. Foster and H. P. Schwan, "Dielectric properties of tissues and biological materials: A critical review," *Crit. Rev. Biomed. Engng.*, vol. 17, no. 1, pp. 25-104, 1989.

[Fric26] T. H. Fricke and S. Morse, "The electric capacity of tumors of the breast," *J. Cancer Res.*, vol. 10, pp. 340-376, 1926.

[Frie98] L. C. Friedman, N. E. Neff, J. A. Webb and C. K. Latham, "Age-related differences in mammography use and in breast cancer knowledge, attitudes, and behaviors," *J. Cancer Educ.*, vol. 13, no. 1, pp. 26-30, 1998.

[Fry83] B. Fry, "A Resistive Tomography Algorithm," M.Sc. Thesis, Department of Electrical and Computer Engineering, The University of Manitoba, Winnipeg, Manitoba, Canada, 1983.

[Fry85] B. Fry and A. Wexler, "Reconstruction system and methods for impedance imaging," Canadian Patent # 1 196 691 and United States Patent # 4 539 640, Granted to Tasc Ltd., Winnipeg, Canada, November 1985.

[Fryk90] E. R. Frykberg, K. I. Bland, and E. M. Copeland, " The detection and treatment of early breast cancer," *Adv. Surg.*, vol. 23, pp. 119-194, 1990.

[Gabr96] C. Gabriel and S. Gabriel, "Compilation of the Dielectric Properties of Body Tissues at the RF and Microwave Frequencies," Technical Report For AFOSR/NL Bolling AFB DC 20332-00014, December 1994-95.

[Gadd92] R. Gadd, P. Record, and P. Rolfe, "Electrical impedance tomography. A sensitivity region reconstruction algorithm using adjacent drive current injection strategy," *Clin. Phys. Physiol. Meas.*, vol. 13, Suppl A (1), pp. 101-105, 1992.

[Gedd67] L. Geddes and L. E. Baker, "The specific resistance of biological materials: a compendium of data for the biomedical engineer and physiologist," *Med. Biol. Engng.* vol. 5, pp. 271-293, 1967.

[Gers99] E. Gersing, "Monitoring temperature-induced changes in tissue during hyperthermia by impedance methods," *Ann. N Y Acad. Sci.*, vol. 873, pp. 13-20, 1999.

[Gese71] B. D. Geselowitz, "An Application of Electrtocardiographic Lead Theory to Impedance Plethysmography," *IEEE Trans. Biomed. Eng.*, vol. 18, pp. 38-41, 1971.

[Gibs98] A. Gibson, S. Somaroo, R. H. Bayford, and D. S. Holder DS, "Development of a reconstruction algorithm for imaging impedance changes in the human head. *X International Conference on Electrical Bioimpedance*, Barcelona, 1998.

[Giss87] D. Gisser, D. Isaacson, and J. C. Newell, "Current topics in impedance imaging," *Clin. Phys. Physiol. Meas.*, vol. 8, Suppl. A, pp. 13-31, 1987.

[Glid97] M. E. Glidewell and K. T. Ng, "Anatomically constrained electrical impedance tomography for three-dimensional anisotropic bodies," *IEEE Trans. Med. Imag.*, vol. 16, no. 5, pp. 572-580, 1997.

[Gord70] R. Gordon, R. Bender, and G. T. Herman, "Algebraic reconstruction techniques (ART) for three-dimensional electron microscopy and x-ray photography," *J. Theor. Biol.*, vol. 29, pp. 471-481, 1970.

[Gord74] R. Gordon, "A tutorial on ART," *IEEE Trans. Nucl. Sci.*, vol. 21, pp. 78 - 93, 1974.

[Guan96] H. Guan and R. Gordon, "Computed tomography using algebraic reconstruction techniques (ARTs) with different projection access schemes: a comparison study under practical situations," *Phys. Med. Biol.*, vol. 41, no. 9, pp. 1727 - 1743, 1996.

[Gord99] R. Gordon and R. Sivaramakrishna, "Mammograms are Waldograms: the need for 3-D breast screening," *Appl. Radiol.*, vol. 28, no. 10, pp. 12-25. 1999.

[Guar91] R. Guardo, R. Boulay, C. Murray, and M. Bertrand "An Experimental Study in Electrical Impedance Tomography Using Backprojection Reconstruction," *IEEE Trans. Biomed. Eng.*., vol. 38, pp. 617-627, 1991.

[Harm98] S. E. Harms, "Integration of breast magnetic resonance imaging with breast cancer treatment," *Top. Magn. Reson. Imaging.*, vol. 9, no. 2, pp. 79-91, 1998.

[Hawl92] M. S. Hawley, J. Conway, H. Amasha, Y. F. Mangnall, and G. C. van Rhoon, "Electrical impedance tomography: prospects for non-invasive control of deep hyperthermia treatments," *Front. Med. Biol. Eng.*, vol. 4, no. 2, pp. 119-128, 1992.

[Hend78] R. P. Henderson and J. G. Webster, "An impedance camera for spatially specific measurements of the thorax," *IEEE Trans. Biomed. Eng.*, vol. 25, no. 3, pp. 250-254, 1978.

[Herr97] R. C. Herrick, L. A. Hayman, K. H. Taber, P. J. Diaz-Marchan, and M. D. Kuo, "Artifacts and pitfalls in MR imaging of the orbit: a clinical review," *Radiographics* vol. 17, no. 3, pp. 707-724, 1997.

[Hind99] W. H. Hindle, L. Davis, D. Wright, "Clinical value of mammography for symptomatic women 35 years of age and younger," *Am. J. Obstet. Gynecol.*, vol. 180, no. 6, part 1, pp. 1484-1490, 1999.

[Hold94] D. S. Holder, N. Anells, and K. G. Boone, "In-vivo images of the female breast obtained with the Sheffield Mark 1 electrical impedance tomography system," *Proceedings of the 3rd meeting of the European Concerted Action on Impedance Tomography*, Ankara, Turkey, September, 1994.

[Holm89] L. Holmberg, J. Ponten, and H. O. Adami, " The biology and natural history of breast cancer from the screening perspective," *World J. Surg.*, vol. 13, no. 1, pp. 25-30, 1989.

[Hua91] P. Hua, E. J. Woo, J. G. Webster, and W. J. Tompkins, "Iterative reconstruction methods using regularization and optimal current patterns in electrical impedance tomography," *IEEE Trans. Med. Imag.*, vol. 10, no. 4, pp. 621-628, 1991.

[Hua93] P. Hua, E. J. Woo, J. G. Webster, and W. J. Tompkins, " Using compound electrodes in electrical impedance tomography," *IEEE Trans. Biomed. Eng.*, vol. 40, no. 1, pp. 29-34, 1993.

[Huyn98] P. T. Huynh, A. M. Jarolimek, and S. Daye, " The false-negative mammogram," *Radiographics.*, vol. 18, no. 5, pp. 1137-54, 1998.

[Ider95] Y. Z. Ider, B. M. Eyuboglu, M. Kuzuoglu, K. Leblebicioglu, U. Baysal, B. K. Caglar, and O. Birgu, "A method for comparative evaluation of EIT algorithms using a standard test," Physiol. Meas., vol.16, Suppl. 3A, pp. 227-236, 1995.

[Isaa86] D. Isaacson, "Distinguishability of conductivities by electric current computed tomography,"*IEEE. Trans. Med. Imag.*, vol. 5, pp. 91-95, 1986.

[Isaa92] D. Isaacson, M. Cheney, and J. C. Newell, "Electrical impedance tomography: Comments on reconstruction algorithms," *Clin. Phys. Physiol. Meas.*, vol. 13, Suppl. A, pp. 83-89, 1992.

[Isma98] Esh. Ismailov, D. G. Khachirov, and IuB. Kudriashov, "Mechanisms of biophysical effects of microwaves," *Radiats. Biol. Radioecol.*, vol. 38, no. 6, 1998.

[Jack93] V. P. Jackson, R. E. Hendrick, S. A. Feig, and D. B. Kopans, "Imaging of the radiographically dense breast," *Radiology*, vol. 188, no. 2, pp. 297-301, 1993.

[Jato99] I. Jatoi, "Breast cancer screening," *Am. J. Surg.*, vol. 177, no. 6, pp. 518-524, 1999.

[John95] C. R. Johnson, "Theme Editor's Introduction: Computational Inverse Problems in Medicine," *IEEE Comput. Sci. Eng.*, vol. 2, no. 4, pp. 42-45, 1995.

[Jong94] H. C. Jongschaap, R. Wytch, J. M. Hutchison, and V. Kulkarni, "Electrical Impedance Tomography: A Review of Current Literature," *Eur. J. Radiol.*, vol. 18, no. 3, pp.165-174, 1994.

[Joss96] J. Jossinet, "Variability of impedivity in normal and pathological breast tissue," *Med. Biol. Eng. Comput.*, vol. 34, no. 5, pp. 346-350, 1996.

[Kerl96] K. Kerlikowske, D. Grady, J. Barclay, E. A. Sickles, and V. Ernster, " Effect of age, breast density, and family history on the sensitivity of first screening mammography," *JAMA*, vol. 276, no. 1, pp. 33-38, 1996.

[Kerl97] K. Kerlikowske and J. Barclay, " Outcomes of modern screening mammography," *J. Natl. Cancer Inst. Monogr.*, vol. 22, pp. 105-111, 1997.

[Kino88] Y. Kinouchi, T. Irritani, T. Ushita, T. Morimoto, S. Kimura, Y. Konishi, and Y. Monden, "Impedance measurement of tumours and its application to diagnoses," *Proc. 10th Annu. Int. Conf. IEEE-EMBS*, New Orleans, 10, pp. 1311, 1988.

[Klei96] F. Kleinermann, N. J. Avis, S. K. Judah, and D. C. Barber, "Three-dimensional image for electrical impedance tomography," *Physiol. Meas.*, vol. 17, pp. A77-A83, 1996.

[Kohn87] R. V. Kohn and M. Vogelius, "Relaxation of a Variational Method for Impedance Computed Tomography," *Comm. Pure Appl. Math.*, vol. 40, pp. 745-777, 1987.

[Kosc84] S. Koscielny, M. Tubian M. G. Le, A. J. Valleron, H. Mouriesse, G. Contesso, and D. Sarrazin, " Breast cancer: relationship between the size of the primary tumour and the probability of metastatic dissemination," *Br. J. Cancer*, vol. 49, no. 6, pp. 709-715, 1984.

[Kotr94] C. J. Kotre, "EIT image reconstruction using sensitivity weighted filtered backprojection," Physiol. Meas. vol. 15, no. 6, Suppl. 2A, pp. A125-36, 1994.

[Kotr96] C. J. Kotre, " Subsurface electrical impedance imaging: measurement strategy, image reconstruction and in vivo results," *Physiol. Meas.*, vol. 17, Suppl. 4A, pp. A197-A204, 1996.

[Kotr97] C. J. Kotre, "Electrical Impedance Tomography," *Brit. J. Radiol.*, vol. 70, pp. S200-205, 1997.

[Kram98] S. Kramer, R. Schulz-Wendtland, K. Hagedorn, W. Bautz, and N. Lang, "Magnetic Resonance Imaging and its Role in the Diagnosis of Multicentric Breast Cancer," *Anticancer Res.*, vol. 18, 3C, pp. 2163-4, 1998.

[Kuni93] C. C. Kuni, "Mammography in the 1990s: A plea for objective doctors and informed patients," *Am. J. Prev. Med.*, vol. 9, no. 3, pp. 185-190, 1993.

[Kuzu92] M. Kuzuoglu, M. Moh'dSaid, and Y. Z. Ider, "Analysis of three-dimensional software EIT phantoms by the finite element method," *Clin. Phys. Physiol. Meas.*, vol. 13, Suppl. A, pp. 135-138, 1992.

[Kyri90] G. A. Kyriacou, C. S. Koukourlis, and J. N. Sahalos, "Evolution of the Reconstruction Algorithm for Electrical Impedance Tomography," *Proc. Electrical Impedance Tomography*, Copenhagen, pp.226-231, 1990.

[Kyri93] G. A. Kyriacou, C. S. Koukourlis, and J. N. Sahalos, "A reconstruction algorithm of electrical impedance tomography with optimal configuration of the driven electrodes," *IEEE Trans. Med. Imag.,* vol. 12, n0.3, pp.430-438, 1993.

[Land88] C. E. Land, "Low-dose radiation - a cause of breast cancer," *Cancer*, vol. 46, pp. 868-873, 1988.

[Lars98] J. L. Larson-Wiseman, "Early breast cancer detection utilizing clustered electrode arrays in impedance imaging," Ph.D. Thesis, Department of Biomedical Engineering, Rensselaer Polytechnic Institute, Troy, NY, USA, 1998.

[Leve44] K. Levenberg, "A method for the solution of certain nonlinear problems in least squares," *Quarterly of Applied Mathematics*, vol. 2, pp. 164-168, 1944.

[Leve84] H. H. Leveen, P. R. Rajagopalan, I. Vujic, R. P. Gobien, P.H. O'Brien, R. Hutto, P. Pontiggia, N. D'Ovidio, R. Pethig, and D. Armitage, "Radiofrequency Thermography, Local Chemotherapy, and Arterial Occlusion in the Treatment of Nonresectable Cancer," *Am. Surg.*, vol. 50, no. 2, pp. 61-65, 1984.

[Lidg92] F. J. Lidgey, Q. S. Zhu, C. N. McLeod, and W. R. Breckon, "Electrical impedance tomography. Electrode current determination from programmable voltage sources," *Clin. Phys. Physiol. Meas.*, vol. 13, Suppl. A, pp. 43-46, 1992.

[Lion97] W. R. Lionheart, "Conformal uniqueness results in anisotropic electrical impedance imaging," *Inverse Problems*, vol. 13, pp. 125-134, 1997.

[Liu88] W. P. Liu, P. Hua, and J. G. Webster, "Three-dimensional reconstruction in electrical impedance tomography," *Clin. Phys. Physiol. Meas.*, vol. 9, Suppl. A, pp. 131-135, 1988.

[Maco83] A. Macovski, "Medical Imaging Systems," Englewood Cliffs, NJ: Prentice Hall, pp. 106-144, 1983.

[Mah92] Z. Mah and H. Bryant, "Age as a factor in breast cancer knowledge, attitudes and screening behaviour," *CMAJ*, vol. 146, no. 12, pp. 2167-2174, 1992.

[Mall67] J. R. Mallard and D. G. Lawn, "Dielectric absorption of microwaves in human tissues," *Nature.*, vol. 213, pp. 28-30, 1967.

[Marq63] D. W. Marquardt, "An algorithm for least squares estimation of nonlinear parameters," Journal of the Society of Industrial and Applied Mathematics (SIAM), vol. 11, pp. 431-441, 1963.

[McLe88] G. L. McLellan, "Screening and early diagnosis of breast cancer," *J. Fam. Pract.*, vol. 26, no. 5, pp. 561-568, 1988.

[Mees95] S. Meeson, A. L. T. Killingback, and B. H. Blott, "The dependence of EIT images on the assumed initial conductivity distribution: a study of pelvic image," Phys. Med. Biol., vol. 40, no. 4, pp. 643-657, 1995.

[Meth96] P. Metherall, D. C. Barber, and B. H. Brown, "Three-Dimensional Electrical Impedance Tomography," *Nature.*, vol. 380, pp. 509-512,1996.

[Mill86] A. B. Miller and R. D. Bulbrook, "UICC Multidisciplinary project on breast cancer: The epidemiology, aetiology and prevention of breast cancer," *Int. J. Cancer*, vol. 37, pp. 173-177, 1986.

[Mill93] A. B. Miller, " Mammography: reviewing the evidence. Epidemiology aspect," *Can. Fam. Physician*, vol. 39, pp. 85-90, 1993.

[Mits88] N. Mitsuyama, T. Morimoto, Y. Kinouchi, T. Iritani, T. Sumi, S. Kimura, and Y. Monden, "In vivo measurements of electrical bio-impedance of breast tumours," *Nippon Geka Gakkai Zasshi.*, vol. 89, no. 2, pp. 251-255, 1988.

[Mode99] N. N. Modeste, V. L. Caleb-Drayton, and S. Montgomery, "Barriers to early detection of breast cancer among women in a Caribbean population," *Rev. Panam. Salud. Publica.*, vol. 5, no. 3, pp. 152-156, 1999.

[Mori90] T. Morimoto, Y. Kinouchi, T. Iritani, S. Kimura, Y. Konishi, and N. Mitsuyama, "Measurement of the electrical bio-impedance of breast tumors," *Eur. Surg. Res.*, vol. 22, pp. 86-92, 1990.

[Mori93] T. Morimoto, S. Kimura, Y. Konishi, K. Komaki, T. Uyama, Y. Monden, Y. Kinouchi, and T. Iritani, "A study of the electrical bio-impedance of tumours,"*J. Invest. Surg.,* vol. 6, no. 1, pp. 25-32, 1993.

[Moru92] J. P. Morucci, Y. Shi, and B. Rigaud, "The modulation transfer function in impedance imaging," Clin. Phys. Physiol. Meas., vol. 13, Suppl. A, pp. 161-166, 1992.

[Moru94] J. P. Morucci, P. M. Marsili, M. Granie, Y. Shi, M. Lei, and W. W. Dai, "A direct sensitivity matrix approach for fast reconstruction in electrical impedance tomography," *Physiol. Meas.*, vol. 15, Suppl. 2A (6), pp. A107-114, 1994.

[Moru96] J. P. Morucci and B. Rigaud, "Bioelectrical impedance techniques in medicine. Part III: Impedance imaging. Third section: medical applications," *Crit. Rev. Biomed. Eng.*, vol. 24, no. 4-6, pp. 655-677, 1996.

[Mu94] Z. Mu, "Electrical impedance computed tomography - algorithms and systems," Ph.D. Thesis, Department of Electrical and Computer Engineering, University of Manitoba, Winnipeg, Manitoba, Canada, 1994.

[Mura85] T. Murai and Y. Kagawa, "Electrical impedance computed tomography based on a finite element model," *IEEE Trans. Biomed. Eng.*, vol. 32, no. 3, pp. 177-184, 1985.

[Muru94] R. M. Murugan, "Investigation of MRI SPAMM Tag Contrast," MSc Dissertation, Center for Medical Imaging Research (CoMIR), Department of Medical Physics, Leeds General Hospital, University of Leeds, Leeds, United Kindom, 1994.

[Neug95] A. I. Neugut and J. S. Jacobson, " The limitations of breast cancer screening for first-degree relatives of breast cancer patients," *Am. J. Public Health*, vol. 85, no. 6, pp. 832-834, 1995.

[Newe88] J. C. Newell, D. Gisser, and D. Isaacson, " An electric current tomograph," *IEEE Trans. Biomed. Eng.*, vol. 35, no. 10, pp. 828-833, 1988.

[Newm97] J. Newman, "Early detection techniques in breast cancer management," *Radiol. Technol.*, vol. 68, no. 4, pp. 325-328, 1997.

[Oost91] A. van Oosterom, "History and Evolution of Methods for Solving the Inverse Problem," *J. Clin. Neurophys.*, vol. 8, pp. 371-380, 1991.

[Park93] D. M. Parkin, P. Pisani, and J. Ferlay, "Estimates of the worldwide incidence of eighteen major cancers in 1985," *Int. J. Cancer*, vol. 54, pp. 59-606, 1993.

[Pate98] M. R. Patel and G. J. Whitman, "Negative mammograms in symptomatic patients with breast cancer," *Acad. Radiol.,* vol. 5, no. 1, pp. 26-33, 1998.

[Paul90] C. Paul, D. C. Skegg, G. F. Spears " Oral contraceptives and risk of breast cancer," *Int. J. Cancer.*, vol. 46, no. 3, pp. 366-373, 1990.

[Peer96] P. G. Peer, A. L. Verbeek, M. Mravunac, J. H. Hendriks, and R. Holland,"Prognosis of younger and older patients with early breast cancer," *Br. J. Cancer.*, vol. 73, no. 3, pp. 382-385, 1996.

[Pisa93] P. Pisani, D. M. Parkin, and J. Ferlay, "Estimates of the worldwide mortality from eighteen major cancers in 1985. Implications for prevention and projections of future burden," *Int. J. Cancer*, vol. 55, pp. 891-903, 1993.

[Plas95] A. Plaskowski, M. S. Beck, R. Thorn and T. Dyakowski, "Imaging industrial flows," Bristol IOP Publishing, ISBN 0 7503 0296 8, 1995.

[Pres86] W. H. Press, B. P. Flannery, S. A. Teukolsky, and W. T. Vetteling, "Numerical Recipes: The Art of Scientific Computing," Cambridge University Press, Cambridge, United Kingdom, 1986.

[Pric79] L. R. Price, "Electrical Impedance Computed Tomography: A New CT Imaging Technique," *IEEE Trans. Nuclear Sci.*, vol. NS-26, no. 2, pp. 2736-2739, 1979.

[Qana99] S. D. Qanadli, M. El Hajjam, B. Mesurolle, L. Lavisse, O. Jourdan, B. Randoux, S. Chagnon, and P. Lacombe, "Motion artifacts of the aorta simulating aortic dissection on spiral CT," *J. Comput. Assist. Tomogr.*, vol. 23, no. 1, pp. 1-6, 1999.

[Rada99] M. M. Radai, S. Abboud and M. Rosenfeld, "Evaluation of impedance technique for detecting breast carcinoma using a 2-D numerical model of the torso," *Ann. N Y Acad. Sci.*, vol. 20, no. 873, pp. 360-369, 1999.

[Rava98] F. Ravandi-Kashani and T. G. Hayes, "Male breast cancer: a review of the literature," *Eur. J. Cancer*, vol. 34, no. 9, pp. 1341-1347, 1998.

[Redd93] J. N. Reddy, "An introduction to finite element method," McGraw Hill College Div; ISBN: 0070513554, 2nd Edition, 1993.

[Reic92] J. G. Reich, "C curve fitting and modeling for scientist and engineers," McGraw-Hill, New York, USA, 1992.

[Rick99] M. T. Rickard, "Current issues in mammographic breast cancer screening," *Hosp Med.*, vol. 60, no. 5, pp. 325-328, 1999.

[Riga96a] B. Rigaud and J. P. Morucci, "Bioelectrical impedance techniques in medicine. Part I: Bioimpedance measurement. Second section: impedance spectrometry," *Crit. Rev. Biomed. Eng.*, vol. 24, no. 4-6, pp. 257-351, 1996.

[Riga96b] B. Rigaud and J. P. Morucci, "Bioelectrical impedance techniques in medicine. Part III: Impedance imaging. First section: general concepts and hardware," *Crit. Rev. Biomed. Eng.*, vol. 24, no. 4-6, pp. 467-597, 1996.

[Riu92] P. Riu, J. Rosell, A. Lozano, and R. Pallas-Areny, "A broadband system for multifrequency static imaging in electrical impedance tomography," *Clin. Phys. Physiol. Meas.*, vol. 13, Suppl. A, pp. 61-66, 1992.

[Riu95] P. J. Riu, J. Rosell, A. Lozano, and R. Pallas-Areny, "Multi-frequency static imaging in electrical impedance tomography: Part 1. Instrumentation requirements," *Med. Biol. Eng. Comput.*, vol. 33, no. 6, pp. 784-792, 1995.

[Rose87] P. P. Rosen, "The pathology of breast carcinoma," In Harris J. R., Hellman S., Henderson I. C., Kinne D. W., eds., Breast Diseases. Philadelphia, Lippincott, pp. 147-208, 1987.

[Saha85] A. V. Sahakian, W. J. Tompkins, and J. G. Webster, "Electrode motion artifacts in electrical impedance pneumography," *IEEE. Trans. Biomed. Eng.*, vol. 32, pp. 449-451, 1985.

[Samu98] T. H. Samuels, "Breast imaging. A look at current and future technologies," *Postgrad. Med.*, vol. 104, no. 5, pp. 91-4, 97-101, 1998.

[Schu98] T. F. Schuessler and J. H. Bates, " Current patterns and electrode types for single-source electrical impedance tomography of the thorax," *Ann. Biomed. Eng.*, vol. 26, no. 2, pp. 253-259, 1998.

[Seag84] A. Seager, M. Yeo, and R. Bates, "Full-wave computed tomography, Part 2. Resolution limits," *IEE Proceedings A*, vol. 131, pp. 612-622, 1984.

[Seag85] A. Seager and R. Bates, "Full-wave computed tomography, Part 4. Low-frequency electric current CT," *IEE Proceedings A*, vol. 132, pp. 455-466, 1985.

[Send82] L. V. A. Sendlein and H. Yazicigil, "Surface Geophysical Techniques in Ground-Water Monitoring. Part II," *Ground Water Monitoring Review.*, 1982.

[Seza89] M. I. Sezan, A. M. Tekalp, and R. Schaetzing, "Automatic anatomically selective image enhancement in digital chest radiography," *IEEE Trans. Med. Imag.*, vol. 8, no. 2, pp. 154- 162, 1989.

[Shah95] A. V. Shahidi, R. Guardo, and P. Savard, "Impedance Tomography: Computational Analysis Based on Finite Element Models of a Cylinder and a Human Thorax," *Ann. Biomed. Eng.*, vol. 23, no. 1, pp. 61-69, 1995.

[Shaw90] E. Shaw de Paredes, L. P. Marsteller, and B. V. Eden, "Breast cancers in women 35 years of age and younger: mammographic findings," Radiology., vol. 177, no. 1, pp. 117-9, 1990.

[Shaw92] E. Shaw de Paredes, "Atlas of film-screen mammography," Baltimore, Williams & Wilkins, 1992.

[Silv96] P. P. Silvester and R. T. Ferrari, "Finite Elements for Electrical Engineers," Cambridge University Press, ISBN: 0521449537, 1996.

[Siva97] R. Sivaramkrishna and R. Gordon, "Detection of breast cancer at a smaller size can reduce the likelihood of metastatic spread: A quantitative analysis," *Acad. Radiol.*, vol. 4, pp. 8-12, 1997.

[Skaa98] P. Skaane, "Magnetic tomography of the breast," *Tidsskr. Nor. Laegeforen.*, vol. 118, no. 16, pp. 2486-90, 1998.

[Skid87] R. Skidmore, J. M. Evans, D. Jenkins, and P. N. T. Wells, "A data collection system for gathering electrical impedance measurements from the human breast," *Clin. Phys. Physiol. Meas.*, vol. 8, Suppl. A, no. 11, pp. 99-102, 1987.

[Smit90] R. W. M. Smith, B. H. Brown, I. L. Freeston, and F. J. McArdle, "Real-time impedance tomography," In T. J. Hames, Ed., *Proceedings of the Copenhagen Meeting on Elctrical Impedance Tomography*, Sheffield University Press, Sheffield, 1990.

[Soll81] B. D. Sollish, E. H. Frei, E. Hammerman, S. B. Lang, M. Moshitzky, "Microprocessor-assisted screening," *Isr. J. Med. Sci.*, vol. 17, no. 9-10, pp. 859-864, 1981.

[Stro96] G. Strobel, "Electrical resistivity tomography in environmental amelioration," PhD. Thesis, University of Manitoba, Department of Electrical and Computer Engineeering, Winnipeg, Manitoba, 1996.

[Suro88] B. A. Surowiec, S. S. Stuchly, J. R. Barr, and A. Swarup, "Dielectric properties of breast carcinoma and the surrounding tissues," *IEEE Trans. Biomed. Eng.*, vol. 35, no. 4, pp. 257-263, 1988.

[Sylv86] J. Sylvester and G. Uhlmann, "A uniqueness theorem for an inverse boundary problem in electrical prospection," *Comm. Pure. Appl. Math.*, vol. 39, pp. 92-112, 1986.

[Taba85] L. Tabar and P. B. Dean, "Teaching Atlas of Mammography," Stuttgart, Thieme Verlag, 1985.

[Tamb87] A. Tamburi, U. Roeper, and A. Wexler, "An Application of Impedance-Computed Tomography to Subsurface Imaging of Pollution Plumes," *Ground-Water Contamination: Field Methods, ASTM STP 963*, A. G. Collins and A. I. Johnson, Eds., American Society for Testing and Materials, Philadelphia, pp. 86-100, 1987.

[Tast81] M. Tasto and H. Schomberg, "Object reconstruction from projections and some nonlinear extensions," presented at the *NATO Advanced Study Institute on Pattern Recognition and Signal Processing*, 25 June - 4 July 1978, Paris France. Also "Method of and device for determining internal body structure," United States Patent 4,263,920 (April 28, 1981).

[Telf76] W. M. Telford, L. P. Geldart, R. E. Sheriff, and D. A. Keys, "Applied Geophysics," Chapter 8, Cambridge University Press, U.K., 1976.

[Trig99] J. P. Trigaux and M. Lacrosse, "Radiation exposure and computed tomography," *Rev. Mal. Respir.*, vol. 16, no. 2, pp. 127-136, 1999.

[Tubi91] M. Tubiana and S. Koscielny, " Natural history of human breast cancer: recent data and clinical implications," *Breast Cancer Res. Treat.*, vol. 18, no. 3, pp. 125-140, 1991.

[Tubi99] M. Tubiana and S. Koscielny, "The rationale for early diagnosis of cancer--the example of breast cancer," *Acta Oncol.*, vol. 38, no. 3, pp. 295-303, 1999.

[Vale89] M. E. Valentinuzzi and L. E. Baker, Eds., "Impedance techniques," *IEEE Eng. in Med. & Biol. Magazine.*, vol. 8, no 1, pp. 10-52, 1989.

[Wahl98] R. L. Wahl, "Overview of the current status of PET in breast cancer imaging," *Q. J. Nucl. Med.*, vol. 42, no. 1, pp. 1-7, 1998.

[Wang94] M. Wang, F. J. Dickin, R. A. Williams, R. C. Waterfall, and M. S. Beck, "Electrical resistance tomography on metal walled vessels in Process Tomography - A Strategy for Industrial Exploitation - eds., M S Beck, E Campogrande, E A Hammer, M Morris, R C Waterfall and R A Williams, UMIST, Manchester, pp. 163-170, 1994.

[Webs90] J. G. Webster, "Electrical Impedance Tomography," J. G. Webster, Ed., Adam Hilger, Bristol and New York, 1990.

[Well74] S. R. Wellings, H. M. Jensen, and R. G. Marcum, "An atlas of subgross pathology of the human breast with special reference to pancreous lesions," *J. Natl. Cancer Inst.*, vol. 55, pp. 231-273, 1974.

[Wexl80] A. Wexler, "Finite Elements for Technologies," TR80-4, Department of Electrical Engineering, The University of Manitoba, Winnipeg, Manitoba, 1980.

[Wexl85] A. Wexler, B. Fry, and M. R. Neuman, "Impedance-Computed Tomography Algorithm and System," *Applied. Optics.*, vol. 24, pp. 3985-3992, 1985.

[Wexl88] A. Wexler, "Electrical Impedance Imaging in Two and Three Dimensions," *Clin. Phys. Physiol. Meas.*, vol. 9, Suppl. A, pp. 29-33, 1988.

[WHO82] World Health Organization, "The World Health Organization histological typing of breast tumors," 2nd ed. *Am. J. Clin. Pathol.*, vol. 78, pp. 806-816, 1982.

[Will88] N. C. Willet, "Dietary fat intake and cancer risk: a controversial and instructive story," *Semin. Cancer Biol.*, vol. 8, no. 4, pp. 245-53, 1998.

[Woo90] E. J. Woo, " ," Ph.D. Thesis, The University of Wisconsin-Madison, 1990.

[Wtor99] J. Wtorek, J. Stelter, and A. Nowakowski, "Impedance mammograph 3D phantom studies," *Ann. N Y Acad. Sci.*, vol. 873, pp. 520-533, 1999.

[Xie92] C. G. Xie, S. M. Huang, B. S. Hoyle, R. Thorn, C. Lenn, D. Snowden, and M. S. Beck, "Electrical capacitance tomography for flow imaging: system model for development of image reconstruction algorithms & design of primary sensors," *IEE Proc. G*, vol. 139, no. 1, pp. 89-98, 1992

[Yang95] W. Q. Yang, M. Byars, and M. S. Beck, "Electrical capacitance tomography - from design to applications," *Measurement and Control.*, vol. 28, no. 9, pp. 261-266, 1995.

[Yang97] W. Q. Yang, R. He, and R. C. Waterfall, "Imaging internal combustion in engines using electrical tomography - special requirements", *Proc. of Frontiers in Industrial Process Tomography - II*, Delft, Netherlands, pp. 143-146, 1997.

[Yell91] A. Yelland, M. D. Graham, P. A. Trott, H. T. Ford, R.C. Coombes, J.C. Gazet, and N. G. Polson, "Diagnosing breast carcinoma in young women," *BMJ.*, vol. 302, no. 6777, pp. 618-620, 1991.

[York88] T. J. Yorkey, J. G. Webster, and W. J. Tompkins, "Comparing Reconstruction Algorithms for Electrical Impedance Tomography," *IEEE Trans. Biomed. Eng.*, vol. 34, pp. 843-852, 1988.

[Ziew99] J. T. Ziewacz, D. P. Neumann, and R. E. Weiner, "The difficult breast," *Surg. Oncol. Clin. N Am.*, vol. 8, no. 1, pp. 17-33, 1999.

Appendix I

Wexler EIT Algorithm for the Novice

In 1985, Wexler *et al.* [Wexl85] proposed an iterative reconstruction algorithm commonly called the "double-constraint method" or the "Wexler Algorithm", to solve for the nonlinear inverse problem in electrical impedance tomography. A discussion of the Wexler EIT algorithmic approach was provided in Chapter 3. The basics mathematics of iterative image reconstruction algorithm, using the Wexler algorithm as an example or the ART algorithm, is described Appendix II and Appendix III respectively. Here a discussion of the simplistic physical approach of the Wexler iterative EIT algorithm is provided. The purpose is to show that the Wexler algorithmic approach can be easily understood with as simple a concept as Ohm's Law, a concept commonly found in any undergraduate physical sciences curricula.

Ohm's Law deals with the relationship between voltage and current in an ideal conductor. This relationship states that the potential difference (voltage, V) across an ideal conductor is proportional to the current I through it,

$$V = IR \qquad \text{[AI.1]}$$

where R is the constant of proportionality, called the resistance, V is the potential difference between two points that include a resistance R, and I is the current flowing through the resistance. For biological work, it is often preferable to use conductance G, the inverse of R. In this form Ohm's Law is given as:

$$I = GV \qquad \text{[AI.2]}$$

In the Wexler EIT algorithm potentials (voltages) are measured on the surface of the object being imaged using a multi-probe extension of the four-probe technique. In the four-probe technique (or tetrapolar configuration), current enters the object via two injecting electrodes (current electrodes) while the signal (potential difference) is picked up by a second pair of electrodes (voltage electrodes) attached to the surface of the object (see Figure AI.0 below).

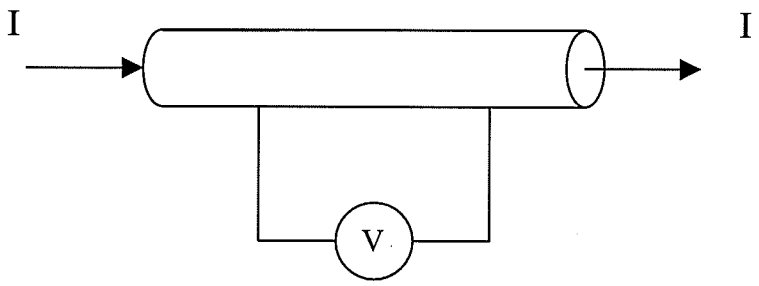

Figure AI.0: A simplified four-probe measurement configuration. Current I, is injected via a pair of electrodes through the continuous object (e.g., cylinder) and voltage V measurements are made on the surface with the other pair of electrodes. In the Wexler algorithm, a multi-probe extension of the four-probe technique is employed to produce sets of currents and voltage measurements.

To produce an acceptable conductance map of the object, linearly independent multiple current and voltage measurements are employed. These measurements are made at low frequency and using high impedance probing electrodes. Since no current leaks across the object, contact resistance for the continuous object (in this example, a cylinder) is of minimal, if not any, importance. This provides true voltage measurements that are used to determine the conductance of the object.

With potentials as measured by application of Neumann (i.e., current) and Dirichlet (i.e., voltage) boundary conditions, Ohm's Law is generally not satisfied within the whole imaging region and a residual $\Re$ is obtained,

$$\Re = (I - GV) \qquad [AI.3]$$

To enforce compatibility, the minimization of the square of the residual over the whole imaging region is sought,

$$R^2 = (I - GV)^2 \qquad [AI.3]$$

$$\frac{\partial R^2}{\partial G} = 2(I - GV)\cdot V = 0 \qquad [AI.4]$$

$$G = \frac{VI}{V^2} \qquad [AI.5]$$

$$\kappa_i = \frac{-\sum_X \iiint_{V_i} \bar{J}\cdot\nabla\phi \, dv}{\sum_X \iiint_{V_i} \nabla\phi\cdot\nabla\phi \, dv} \qquad [3.5]$$

Equation AI.5 yields,

$$GV = I \qquad [AI.7]$$

which is Ohm's Law. Note that if one substitutes V for $\nabla\phi$ and I for $\bar{J}$ in [AI.5], one gets equation 3.5 in Chapter 3. Equation 3.5 is the revised conductance for the imaging region.

Appendix II

Basics of the Iterative Technique

Generally, there are a few steps that are common to most iterative methods. These are outlined below:

a) Assume an initial value for conductivity distribution.

b) Solve the forward problem to calculate surface voltages ϕ from the assumed conductivity distribution. The Finite Difference Method (FDM) or Finite Element Method (FEM) is normally used to solve the forward problem.

c) Applying the results from the Forward problem to determine how close the assumed conductivity distribution is to the real (i.e., measured) conductivity distribution.

d) Improve conductivity distribution recursively.

e) Repeat from (b) until convergence, i.e., the difference between measured and predicted ϕ is zero or suitably small.

It is primarily steps (c) and (d) which distinguishes one iterative reconstruction method from another.

Most of the iterative algorithms, e.g., the Wexler algorithm, employ Poisson's equation (1.0) to describe the continuous electrical field problems and solve surface potential distributions with numerical techniques. The finite element method (FEM) is usually the numerical technique used in solving electric field equations to obtain the potential distribution within a region of interest under an assumed conductivity distribution and boundary conditions. These techniques provide the ability to generate

estimates of boundary potential measurements for a given impedance distribution and are the basis of most iterative techniques.

The first step of the numerical solution of Poisson's equation with FEM involves dividing the region of interest into many smaller regions called elements. The total region is then described on an element-by-element basis (Figure AII.1).

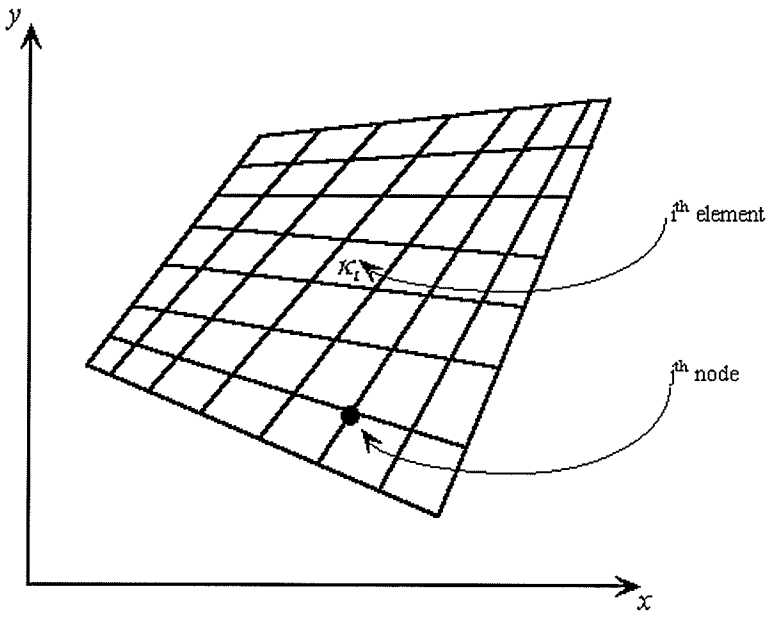

Figure AII.1: An arbitrary 2-D region divided into some finite quadrilateral elements. κ_i, is the conductivity of element i and j represents a node of an element.

The FEM uses the variational principle, in which the field is represented using a piecewise continuous function and the variational integral is minimized with respect to the residual or functional to best approximate the actual field. The variational method is fully described in [Berr92].

If the region is divided into smaller elements the values of conductivity κ_i within each element are assumed to be constant. The field ϕ is given by

$$\phi = \sum_{i=1}^{n} \alpha_i(x, y)\phi_i \qquad \text{[AII.1]}$$

where $\alpha_i(x, y)$, is the interpolation polynomial defined over the *x-y* surface, and *n* is the total number of nodes within the element. Equation (AII.1) can also be rewritten as,

$$\phi = \alpha^T\phi = \phi^T\alpha \qquad \text{[AII.2]}$$

The appropriate functional for the solution of the Poisson's equation is

$$F = \iint_B \kappa\left[\left(\frac{\partial\phi}{\partial x}\right)^2 + \left(\frac{\partial\phi}{\partial y}\right)^2\right] dxdy - 2\int_B \phi h\, ds - 2\iint_B \phi f\, dxdy \qquad \text{[AII.3]}$$

where h is the Neumann condition on the boundary. Equation (AII.3) is minimized by differentiating with respect to the variational parameter ϕ , and set to zero

$$\frac{\partial F}{\partial \phi} = 0 \qquad \text{[AII.4]}$$

Upon substitution of (AII.2) into (AII.4) and differentiating with respect to the new variational parameter ϕ_i, one yields,

$$\frac{\partial F}{\partial \phi_i} = \iint_B \kappa\left[\left(\frac{\partial\alpha_i}{\partial x}\phi_i + \frac{\partial\alpha_j}{\partial x}\phi_j + \cdots\right)\frac{\partial\alpha_i}{\partial x} + \left(\frac{\partial\alpha_i}{\partial y}\phi_i + \frac{\partial\alpha_j}{\partial y}\phi_j + \cdots\right)\frac{\partial\alpha_i}{\partial y}\right] dxdy$$

$$-2\int_B h\alpha_i ds - 2\iint_B f\alpha_i\, dxdy = 0 \qquad i, j = 1,2,\ldots..,n \qquad \text{[AII.5]}$$

The first integral yields a square *n* x *n* matrix where *n* is the number of variational nodal points and the latter two integrals can be summed to yield a vector of length *n*. The resulting set of linear equations can be put in standard matrix form as,

$$S\underline{\phi} = \underline{b} \qquad \text{[AII.6]}$$

where,

$$S_{ij} = \iint_B \kappa \left(\frac{\partial \alpha_i}{\partial x}\frac{\partial \alpha_j}{\partial x} + \frac{\partial \alpha_i}{\partial y}\frac{\partial \alpha_j}{\partial y} \right) dxdy \qquad \text{[AII.7]}$$

$$b_{ij} = \int_B h\alpha_i ds + \iint_B f\alpha_i \, dxdy \qquad \text{[AII.8]}$$

where, $i, j = 1,2,....,n$ and ϕ_i are the unknowns to be solved.

Subsequently, the integration is performed using a standard procedure. One such procedure is to map a standard square element into a general quadrilateral before integration [Berr92]. An appropriate transformation is used to map a square element in local coordinates to the general quadrilateral in global coordinates. By introducing new variables of integration,

$$x = x(\xi,\eta) \qquad \text{and} \qquad y = y(\xi,\eta)$$

and using the Jacobian transformation to map the element in local space to global space,

$$J = \begin{bmatrix} \frac{\partial x}{\partial \xi} & \frac{\partial x}{\partial \eta} \\ \frac{\partial y}{\partial \xi} & \frac{\partial y}{\partial \eta} \end{bmatrix} \qquad \text{[AII.9]}$$

equation (AII.7) can be simplified as,

$$\iint_B f(x,y)dxdy = \iint_{B'} f\left[x(\xi,\eta), y(\xi,\eta)\right] |J| \, d\xi d\eta \qquad \text{[AII.10]}$$

whereby, the values of $\frac{\partial \alpha_i}{\partial x}$ and $\frac{\partial \alpha_i}{\partial y}$ can be determined from,

$$\begin{bmatrix} \frac{\partial \alpha_i}{\partial x} \\ \frac{\partial \alpha_i}{\partial y} \end{bmatrix} = [J] \begin{bmatrix} \frac{\partial x}{\partial \xi} \\ \frac{\partial y}{\partial \xi} \end{bmatrix} / |J| \qquad \text{[AII.11]}$$

and this provides a desired result to perform the integration over a square element using numerical quadrature schemes, e.g., the generalized Gaussian Quadrature methods for two-dimensional and three-dimensional approximations [Berr92]. For multiple integration over 2-D or 3-D, the Gaussian quadrature formulae for estimating an integral of a function $f(\xi)$ on the interval $-1 \leq \xi \leq 1$ is simply the generalizations of those for 1-D respectively. In 1-D, the Gaussian quadrature formula for estimating an integral of a function $f(\xi)$ on the interval $-1 \leq \xi \leq 1$ is given by,

$$\int_{-1}^{+1} f(\xi) d\xi \cong \sum_{i=1}^{m} W_i f(\xi_i) \qquad \text{[AII.12]}$$

where ξ_i is some point located in the interval, W_i is a weight associated with the i-th point, and m is the total number of points. The weights and points are determined by assuming that f is a polynomial of degree $2m$-1 and then computing the points and weights that guarantee an exact result for such a polynomial. Similarly, integration over 2-D and 3-D is given by equations (AII.13 and AII.14) respectively.

$$\int_{-1}^{+1} \int_{-1}^{+1} g(\xi,\eta)\, d\xi\, d\eta = \sum_{i,j} W_i W_j g(\xi_i, \eta_j) \qquad \text{[AII.13]}$$

$$\int_{-1}^{+1} \int_{-1}^{+1} \int_{-1}^{+1} h(\xi,\eta,\varsigma)\, d\xi\, d\eta\, d\varsigma = \sum_{i,j,k} W_i W_j W_k h(\xi_i, \eta_j, \varsigma_k) \qquad \text{[AII.14]}$$

Gaussian quadrature uses the fact that the choice of abscissas at which to evaluate the function to be integrated can substantially contribute to improving the accuracy of the result. Further accuracy can be obtained by using higher order approximations, for example, by adding more nodes to the elements. In the Wexler 2-D EIT

algorithm, the degree of approximation is improved from linear to quadratic by using 9-node quadrilaterals as shown in Figure AII.2a.

(a) **(b)**

Figure AII.2: (a) Higher-order elements employed in the 2-D Wexler algorithm. Element has 9 nodes quadrilateral, (b) the standard element in 3-D, obtained by adding depth to 2-D element.

Higher-order elements can produced better results, however, increasing the number of nodes is equivalent to increasing the number of unknowns which in turn would require more computational effort. As such, the elements employed in the 3-D Wexler algorithm are created by adding depth to elements of 2-D. The standard elements in 3-D is linear with 8 nodes as shown in Figure (AII.2b). Justifications for the choice of elements configuration employed in this thesis are provided by Berryman 1992 [Berr92].

Appendix III

Algebraic Reconstruction Techniques (ART): Its Relation to EIT

Gordon, Bender, and Herman introduced algebraic reconstruction techniques (ART) in 1970 for solving the problem of three-dimensional reconstruction from projections in electron microscopy and x-radiology [Gord70]. In x-ray computer tomography (CT) for example, ART is a conceptually simple method of reconstructing the attenuation matrix from the measured ray sums (or projections) [Maco83]. It is an iterative approach where the matrix of x-ray attenuation values is first assigned a random value. Thereafter, a sequence of steps is performed where sums along the paths through the matrix are given new values to match the corresponding measured ray sums. The literature on ART and variants are numerous. Gordon, 1974 gave a comprehensive tutorial on ART [Gord74], Macovski, 1983 provided simple illustrations and examples of the method. Recently, Guan and Gordon, 1996, using different projection schemes, demonstrated the potential of ART in computed tomography [Guan96].

Barber and Brown developed one of the first in vivo EIT image reconstruction algorithms [Barb83]. The algorithm was an adaptation of the filtered-backprojection method used in computed tomography [Maco83]. In EIT, the ray sums are the measured voltage differences between the adjacent electrodes for each pair of current electrodes. The images produced by each current configuration are summed and filtered as in CT imaging, to form the tomographic image. Realizing that EIT is a nonlinear inverse problem, requiring an iterative approach for the correct solution, an attempt was made here at adapting a CT-based algorithm, ART, to solve the EIT problem.

Two- and three-dimensional computer simulations were employed to access the potential of the basic ART algorithm in producing tomographic impedance images. In ART, the resistivity of each element is corrected at every *projection angle (or view).* Here the term projection angle describes the procedure of solving Laplace equation, or measuring voltage on the electrodes (voltage electrodes), with a specific active electrode pair (current electrodes).

The impedance images recovered using the basic ART algorithm were disappointingly of low quality. The poor quality of the recovered image, using the basic ART algorithm, is the result that at every correction, the number of unknowns (number of elements) is usually greater than the number of linearly independent measurements (i.e., number of equations). This caused the method to diverge unless some restrictions to the number of the unknowns are placed. One possible solution would be to maintain the resistivity of some elements at a constant value? For the two-dimensional simple simulation model employing 9×9 elements with 18 electrodes, one has 81 unknowns and only a maximum of 17 unique measurements for a single view. This scenario is equivalent to a determinacy of $17/81 \approx 0.21$ (i.e., a very underdetermined problem).

With SIRT (Simultaneous Iterative Reconstruction Technique), all the linearly independent measurements are collected first by taking all the possible projection angles (this is called an iteration). Subsequently, the elements resistivity correction are made. This algorithmic approach is similar to that employed by the Wexler EIT algorithm. Using the previous example, the total number of independent measurements, using SIRT, is $N(N-1)/2 = 153$, which is much greater than the total number of unknowns for a determinacy of ≈ 1.89. This is an appropriate determinacy for avoiding divergence.